UNIVERSITÀ
DEGLI STUDI
DI PADOVA

Università degli Studi di Padova
Centro Interdipartimentale di Studi e Attività Spaziali CISAS "G.Colombo"

Dipartimento di: Ingegneria dell'Informazione DEI

SCUOLA DI DOTTORATO DI RICERCA IN : Scienze Tecnologie e Misure Spaziali (STMS)
INDIRIZZO: **Astronautica e Scienze da Satellite (ASS)**
CICLO: **XXII**

ANALYSIS OF THE STEREOSCOPIC PERFORMANCE OF THE STEREO CAMERA (STC) FOR THE BEPICOLOMBO MISSION: A NEW METHOD FOR 3D RECONSTRUCTION

Direttore della Scuola : Ch.mo Prof. Giampiero Naletto
Supervisore :Ch.mo Prof. Giampiero Naletto
Co-Tutore: Dott. Gabriele Cremonese

Emanuele Simioni

"Non vogliamo la luna. Abbiamo le stelle" (L.d.S.)

Sommario

La missione BepiColombo, cornerstone n. 5 dell'Agenzia Spaziale Europea (ESA), partirà nell'agosto del 2014 alla volta di Mercurio. Lo scopo della missione è un'analisi più approfondita di uno dei pianeti più interessanti del Sistema Solare e migliorare la conoscenza di alcune costanti della fisica fondamentale.

Visitato poche volte nella storia (solo due sonde americane hanno finora raggiunto Mercurio: la Mariner 10 nel '75 e attualmente la MESSENGER), il pianeta presenta delle caratteristiche ambientali critiche dovute alla sua vicinanza al Sole e alla sua orbita, e risulta di enorme interesse, considerata la sua craterizzazione e la presenza di un campo magnetico.

Uno strumento particolarmente ambizioso della sonda è rappresentato da STC, una stereo camera push frame (a sensore bidimensionale), compattezza progettata a partire da un disegno ottico particolare ed innovativo derivato da una collaborazione tra l'Università di Padova, l'Osservatorio Astronomico di Padova (INAF) e l'attuale Istituto di Fotonica e Nanotecnologie LUXOR UOS-Padova del CNR.

A differenza delle classiche stereo camere, STC è l'unica ad avere un unico sensore e due canali di acquisizione. I due canali che acquisiranno le immagini della superficie di Mercurio sono inclinati di un angolo di $\pm 20°$ rispetto a nadir. La diversa orientazione dei due sistemi ottici consentirà di acquisire immagini della stessa zona della superficie di Mercurio da due direzioni diverse, e con una baseline molto lunga; questo consentirà di ottenere a posteriori una ricostruzione tridimensionale della superficie con un'accuratezza verticale di 80 metri e una risoluzione spaziale di 50 metri.

Le caratteristiche ambientali del pianeta hanno obbligato il team di STC a progettare un disegno particolarmente complesso per la camera. Le escursioni termiche dovute all'irradiazione della superficie renderanno ulteriormente complicata la modellazione della camera dal punto di vista proiettivo, ovvero la sua calibrazione.

Questo contesto ha anche obbligato il team di Padova ad affrontare l'implementazione di un algoritmo dedicato allo strumento più adattabile dei classici algoritmi e che potesse essere utilizzato come sistema di feedback per la calibrazione dello strumento stesso.

In campo di analisi di immagini, data la relativa novità della scienza, il panorama presenta un livello di specializzazione molto settoriale. Il contributo di molti ricercatori e di lucidi visionari ha permesso, nell'ultimo secolo, di approfondire problematiche quali la ricostruzione 3D da innumerevoli fonti di informazione: la stereoscopia (ovvero la ricostruzione tramite triangolazione da punti di vista differenti), la ricostruzione da illuminazione (ovvero la ricostruzione basata sulla variazione dell'intensità luminosa di un oggetto dovuta alla sua curvatura), la ricostruzione da ombre e la ricostruzione basata semplicemente sulla forma.

Tutti questi settori di ricerca hanno avuto grande successo come sistemi di misura a basso costo e compatti, ma raramente sono stati applicati?in maniera sincrona, se non all'interno di un processo iterativo lineare.

L'algoritmo dedicato alla stereo camera STC rappresenta un tentativo di integrare tutte queste informazioni contemporaneamente allo scopo di avere una ricostruzione greedy (ovvero globalmente ottimale).

Il metodo scelto per il raggiungimento di questo scopo è utilizzato nei processi di segmentazione di immagini, sulla base del riconoscimento di forma, esteso in un campo multidimensionale. Tale metodo, normalmente citato come *Snakes* o *Modelli Deformabili*, invece di procedere in maniera iterativa o gerarchica nella risoluzione di un problema, lo affronta in maniera più continua. Più precisamente, il classico metodo di procedere consiste nel risolvere il problema sfruttando alternativamente i vari metodi di ricostruzione e le ipotesi sul target. Quello che invece fanno gli *Snakes* è partire da una soluzione iniziale approssimativa al problema, per poi farla evolvere spinta da due classi di "forze" dipendenti dal tempo: le forze interne che tengono conto delle ipotesi sul target e quelle esterne rappresentative dei sistemi di equazioni che derivano dal metodo di ricostruzione utilizzato o dal modello della camera.

Per questo motivo all'algoritmo è stato dato il nome di SIEM ovvero Stereo Images Evolving Model (Modelli Evolventi per le Immagini Stereoscopiche).

Le forze interne ed esterne spingono il modello *Snake* (considerabile in un certo senso come la ricostruzione 3D del pianeta) ad una evoluzione temporale agendo "localmente" e facendolo tendere ad una soluzione ottimale.

Nel caso della ricostruzione superficiale di Mercurio sono state prese in considerazione tre tipi di "forze":

- le forze interne che obbligano la soluzione ad essere continua (ovvero che soddisfano l'ipotesi di continuità del target);

- le forze esterne di stereoscopia (che spingono la ricostruzione a soddisfare i vincoli di "somiglianza locale" tra le immagini stereoscopiche);

- le forze esterne di shading (che spingono la ricostruzione a restituire, se illuminata con le stesse condizioni, immagini compatibili con le originali).

Particolare difficoltà incontrata in questo processo è la normalizzazione di questi tre tipi di modelli in modo che la ricostruzione finale sia effettivamente ottimale in relazione alla specificità della situazione.

Pure senza aver ancora affinato l'utilizzo delle forze di shading l'algoritmo ha dato dei risultati comparabili e spesso superiori all'attuale stato dell'arte.

Oltre al vantaggio di avere un'effettiva ricostruzione **completa** della il metodo è estendibile ad altre ipotesi sul target o ad altre fonti di informazione presenti nelle immagini.

Il progetto architetturale di SIEM è stato improntato esattamente a questo scopo: implementato in due linguaggi di programmazione, MATLAB (per la sua componente grafica) e C++ (per le librerie dinamiche), ha una struttura dati a celle parallele che lo rende estendibile a nuove possibili sorgenti d'informazione eventualmente disponibili.

Esso è stato testato con robusti algoritmi quali il DLRmatch realizzato al DLR di Berlino e il DenseMatcher, algoritmo stereoptico utilizzato da anni in fotogrammetria e progettato all'Università di Parma sia su immagini sintetiche che su coppie di immagini della sonda MESSENGER per Mercurio o di ASTER per la Terra.

I classici algoritmi stereo necessitano l'utilizzo di finestre di confronto (*matching windows*) estese, dovendo usare il solo stereo come fonte d'informazione; questo introduce però un effetto di riduzione dei dettagli 3D (*smoothing*). Il SIEM invece, utilizzando più fonti di informazione può usare finestre di dimensioni minore evitando l'introduzione di questo effetto.

Lo studio di differenti settori di analisi di immagini per l'implementazione dell'algoritmo ha permesso, inoltre, la possibilità di applicare nuove tecniche in campi disparati e diversi da quello specifico della BepiColombo. In particolare, durante il suo sviluppo il toolbox di analisi di immagini è stato utilizzato e testato nel contesto della missione Rosetta dopo il flyby con l'asteroide Steins: questo ha portato da una parte a scoprire la presenza di significative problematiche di calibrazione dell'orbita della sonda; dall'altra, i suoi risultati sono stati utilizzati per le operazione di craterizzazione dell'asteroide. Il toolbox di immagini è stato inoltre utilizzato come metodo di calibrazione di sistemi onground per la ricostruzione di reperti archeologici.

In sintesi il lavoro svolto che viene presentato in questa tesi ha dimostrato le sue capacità in differenti campi di metrologia e ha contribuito a disparati progetti. Molto lavoro deve ancora essere fatto per rendere il SIEM un algoritmo robusto e autonomo per la ricostruzione di superfici planetarie ma i risultati finora ottenuti rendono avvincente e speranzoso questo percorso.

Table of contents

Chapter 1

Notation

Symbols

$\mathbf{x}$	*bold letters represent 3D vectors or points.* $x \in R3$
$\mathbf{x}$	*hat letters represent 2D vectors or points.* $x \in R2$
$\mathbf{MW\times}$ $\mathbf{H}$	*space of the Matrixes with W rows and H columns.*
D	*Disparity map*
ΩAB	*Map or functional. With domain in the set* A *and range in* B

Acronyms

AAL	*Angle At Intersection (Angle Between The Two Optical Axes Of The Stereo Pair)*
ABM	*Area-Based Matching*
ADD	*Architectural Design Document*
AoV	*Angle Of View, (Between Optical Axes And Mean Normal Surface)*
APS	*Active Pixel Sensor*
ASI	*Italian Space Agency*
ASTER	*Advanced Spaceborne Thermal Emission And Reflection Radiometer*
AVI	*Audio Video Interleave*

BELA	*BepiColombo Laser Altimeter*
BL	*Base Line Of The Acquisition System*
CCD	*Charge-Coupled Device*
CD	*Current Document*
CG	*Computer Graphics*
CISAS	*Interdepartmental Center For Space Studies And Activities*
CMOS	*Complementary Metal-Oxide Semiconductor*
CNR	*National Research Council*
D2M	*Disparity To Measurements*
DDL	*Digital Disparity Log*
DDM	*Digital Disparity Model: Disparity Map Between The Images*
DDM –	*Digital Disparity Model,*
DLL	*Dynamic Link Library*
DLL-SIEM	*Dynamic Link Library [C++] Snaked Based Algorithm Developed*
DLR	*German Aerospace Center*
DTM	*Digital Terrain Model*
EE	*Ensquared Energy*
EMP	*Evolving Model Protocol*
ESA	*European Space Agency*
FBM	*Feature-Based Matching*
FM	*Flight Model*
FoV	*Field Of View*
FPA	*The Focal Plane Assembly*
FSA	*Filter Strip Assembly*
GUI	*Graphic User Interface*
GUI-SIEM	*User Interface [MATLAB] For Data Parameters Setting And Projects Definition*
HRIC	*High Resolution Imaging Channel*
HRSC	*High Resolution Stereo Camera*
I2P	*Images To Project*
IFN	*Institute For Photonics And Nanotechnologies*
INAF	*National Institute For Astrophysics*
IVM	*Images View Mode (Shows The Datas As Images);*
JAXA	*Japanese Space Agency*
LSM	*Least Squares Matching*
LUXOR	*Laboratory For Ultraviolet And X-Ray Optical Research*
MCGM	*Multiphoto Constrained Geometrically Matching*
MMO	*Mercury Magnetospheric Orbiter*
MPO	*Mercury Planet Orbiter*
MTF	*Modulation Transfer Function*
NAC	*Narrow Angle Camera*
NAIF	*Navigation And Ancillary Information Facility*
NCC	*The Normalized Cross Correlation*
OGSE	*Optical Ground Support Equipment*

OLS	*Ordinary Least Square*
OS	*Operative System*
PC	*Personal Computer*
PDE	*Partial Differential Equation*
PHD	*Doctor Of Philosophy*
PMM	*Pan Mouse Mode (To Pan The Data);*
PXL	*Pixel*
RAM	*Random-Access Memory*
RMS	*Learn Root Mean Square*
S/C	*Spacecraft*
S/W	*Software*
SAD	*The Sum Of Absolute Differences*
SCD	*Source Code Documentation*
SCS	*Self Calibration System*
SDI	*Stereo Data-Project Instance*
SDP	*Stereo Data Protocol*
SDP	*Stereo Data Protocol*
SELENE	*Selenological And Engineering Explorer*
SFS	*Shape From Shading*
SIEM	*Stereo Image Evolving Models*
SPI	*Stereo Pair Images*
SSD	*Sum Of Squared Distance*
STC	*Stereoscopic Imaging Channel*
STM	*Structural And Thermal Model*
SVM	*Surf View Mode (Show The Data As 3D Surfaces);*
TMM	*Turn Mouse Mode (To Turn In 3D Mode The Surfaces);*
URD	*User Requirements Document*
UTC	*Coordinated Universal Time*
VIHI	*Visible And Near-Infrared Hyperspectral Imager*
VVM	*Video View Mode (Save All Cycles In A Movie);*
WAC	*Wide Angle Camera*
ZMM	*Zoom Mouse Mode (To Zoom Or De-Zoom The Data);*

Chapter 2

Summary

In the last years, Computer Graphics, Imaging Science and technical progress of the acquisition systems have filled incredible gaps becoming, year after year, always more integrated and giving important instruments in measurements processes.

In the last years even the computer process power have improved on the other side allowing to gain a more interdisciplinary use of the resources actually in the hand of Imaging Science.

The work that will be described in this thesis is a result of this process and have to be read in Imaging Measurement techniques evolution.

The field in the vanguard for the application of this new system is obviously the astronautic one where techniques and difficulties are more challenging and complex.

Scope of this thesis is the management of a new algorithm for the 3D reconstruction in the context of the BepiColombo mission, a cornerstone mission of the ESA, oriented to the study of planet Mercury.

Thanks to the interdisciplinary cohesion between *ASI Italian Space Agency* and *INAF National Institute of Astrophysics* the mission has given the possibility to obtain great results in the evolution of new methods for the imaging 3D reconstruction.

In the payload of BepiColombo mission there is the brand-new camera instrument STC Stereo Channel. A camera doted of a new design, and which demands new method for the data analysis in particular for the generation of a high resolution 3D characterization of the hermitian surface.

Principal contribution of the work presented in this thesis is, exactly, the description of a new algorithm for stereo reconstruction,the so called *SIEM (Stereo Images Evolving Models),*which want to be a weapon more adaptable and more extendible of the classical stereo-algorithm to balance the issues around the STC Stereo Channel design and the hermitian environments .

The attempt of this software is to use more kind of information beyond the stereo constraint using multiple integration of different branch of image analysis and computer graphics.

The first two introductive chapters are dedicated to a description of all the imaging knowledge used to the generation of this. The new algorithm is exposed in details in the Chapter 3, giving an idea of all the problems linked to the attempt to integrate branches so distant in a same pipeline process for the 3d reconstruction.

The versatility needed by the algorithm is obviously linked to the optical design of STC instrument.

Chapter 4 will describe the satellite context and the optical design of the instruments showing the problems around a so ambitious project which justifies the actual commitment in the project of the generation of a more robust and adaptable algorithm as the SIEM.

In Chapter 5 the SIEM will be described in detail. The main idea of the algorithm is to use the different information and hypotheses usable or definable in the context of a target-camera system. The algorithm is so described even in its informatics architecture defined to manage all the information at the same time.

In Chapter 6 tests for the validation of the algorithm are presented. In the last years the tests were performed in different contexts giving a strong help to the step evolution of the algorithm both from design and informatic point of view. A brief history of this tests actually still used for the choices linked to the paralleled evolution of STC camera will be so exposed.

On the side of this work will exposed some different application of the knowhow acquired during the CISAS*(Interdepartmental Center* for Space Studies and Activities*) PhD*.

Different toolboxes for image analysis were created in the last years of my PhD for the BepiColombo mission. Those toolbox were even used in different contexts as taxonomy in on-ground application and asteroid data analysis still in satellite field.

A pair of this application will be exposed in the seventh chapter.

An overall view of the work is given in a conclusive section together with highlights on the future programs.

Most of the results achieved in the present work have been shown in National and International Meetings in the context of ESA European Space Agency and have brought to publications in astronautic or imaging Journals.

My conclusion could be summarized in saying that a lot of job has been done: a publication for a new stereo algorithm snake based is an important goal reached but a lot of work has still to be done for a robust use of the algorithm; the iteration between this research and the actual needs in the STC on Ground Calibration pipeline will be a strong help for both the contexts: the complete integration of the method SIEM on one side and the validation of an instrument, so complex and challenging, on the other one.

Chapter 3

Background and related work

Contents

Introduction

The main aim of this chapter is an overview of the methods and the algorithm normally used in imaging applications to obtain 3D information from images. To have a complete background about the problems which have finally brought to the definition of a new algorithm to be applied for the 3D reconstruction of the Mercury surface, a first simple model of a camera is presented. After this, five sections illustrating different branches of imaging are introduced:

-*Stereo Method*

-*Segmentation*

-*Snakes*

-*Shape from silhouette*

-*Shape from Shading*

The first is dedicated to the *stereopsis* (from *stereo*- meaning "solid", and -*opsis* meaning view or sight), and is a survey of the rules around binocular view; also the state of the art of 3D reconstruction stereo-matching based is presented. The second section describes the *segmentation*, that is the process to reveal the boundaries of features in an image; this is an important concept used in the following sections that needs to be investigated. Then, also a method for segmentation called *snakes* is explained: although not clearly connected with 3D reconstruction this method represents the kernel of the stereo algorithm presented in the next chapter. The fourth section illustrates the *shape from silhouette*. This is a method, used for the reconstruction of small and closed surface regions, which adopts a base segmentation process. Even if not strictly related to the main subject of the thesis, it is described because it has been used to reconstruct the shape of the Steins asteroid, which has been observed by the OSIRIS instrument [THO98] on board the Rosetta satellite in 2008. Last section of the chapter offers an overview of the *shape from shading* techniques. This is the only monocular based 3D method presented here and it will show its capabilities in the final algorithm.

3.1 Acquisition image systems model

In this section the simplest perspective camera model is explained. This corresponds to an ideal pinhole camera. A similar process is the well known human eye acquisition system under some approximations.

The basic idea of the pinhole model is a simple camera without a lens and with a single small aperture. The camera structure can be approximated to the pinhole model when the size of the aperture is 1/100 or less of the distance between it and the projected image.

3.1.1. Brief history

As far back as the 4th century BC, Greeks such as Aristotle and Euclid wrote about naturally-occurring rudimentary pinhole cameras. It was the 10th century when Ibn al-Haytham published this idea in the Book of Optics in 1021 AD. When Ibn al-Haytham began his experiments with the “camera obscura”, he stated: *Et nos non inventimus ita*, that is "we did not invent this" [HA21] (see Figure).

He improved the camera after realizing that the smaller the pinhole, the sharper the image (though the less the light). He provides the first clear description for construction of a “camera obscura”. As a side benefit of his invention, he was credited with being the first man to shift physics from a philosophical to an experimental basis.

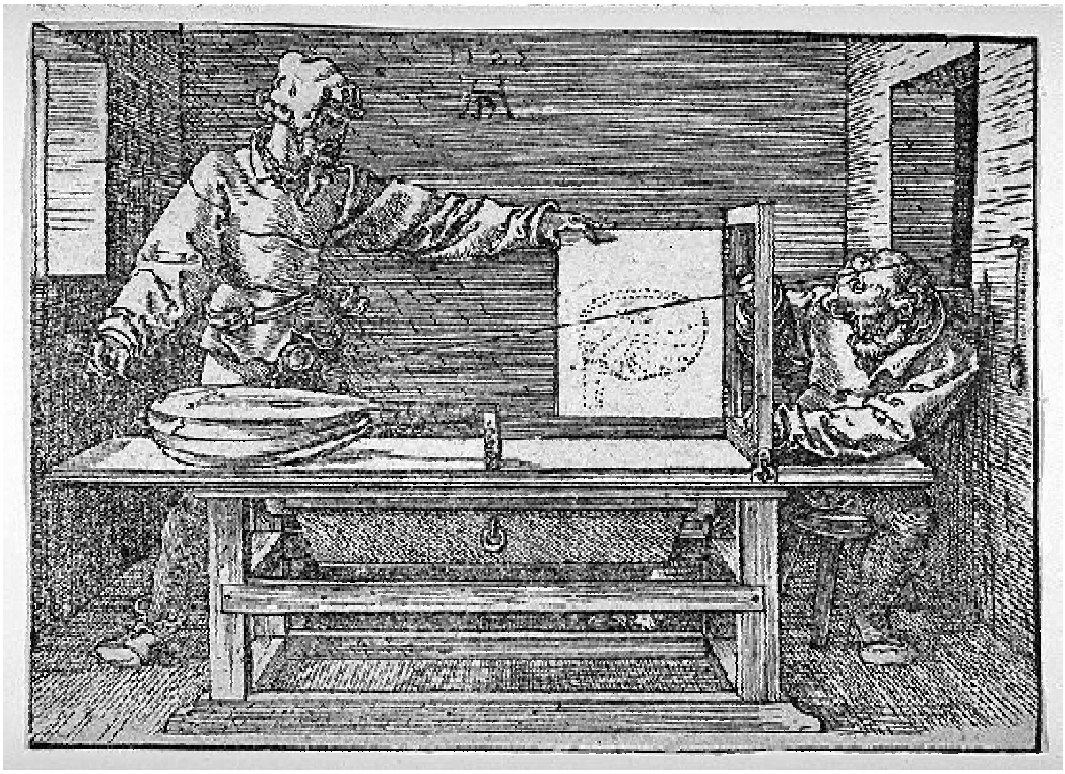

(a)

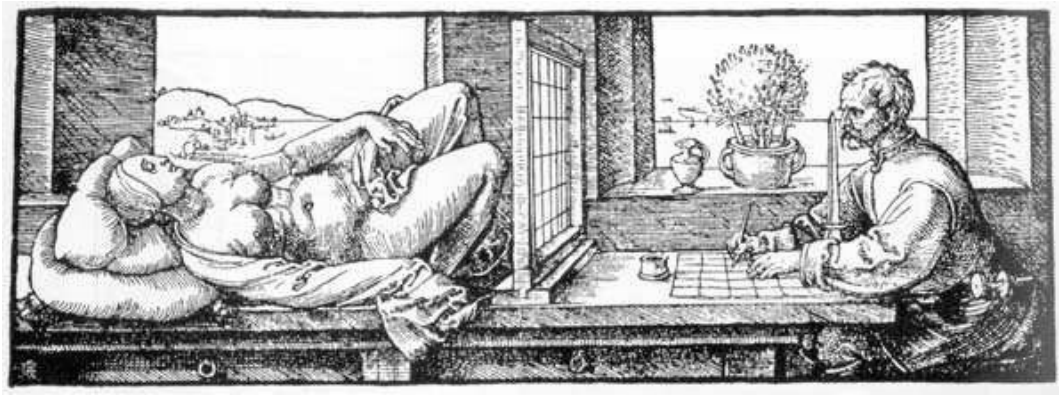

(b)

Figure *(a) "The Draughtsman of the Lute" (woodcut 1525, Albrecht Dürer) shows the prospective process. (b) From the same author "Engraving". Here there is another way of thinking about the pinhole model. Suppose you view a scene with one eye looking through a square window, and draw a picture of what you see through the window. In this case the human eye is the optical center and the grid window represent the image plane.*

Figure *Page from Book of Optics by Ibn al-Haytham: optical structure of the human eye and basic scheme of the pinhole camera.*

The same results have been achieved in Asia in the 5th century BC by the Mohist philosopher Mo Jing (墨經) mentioning the effect of an inverted image forming through a pinhole. The image of an inverted Chinese pagoda is mentioned in Duan Chengshi's (died 863) book "Miscellaneous Morsels from Youyang". The Chinese scientist Shen Kuo (1031–1095), in addition to the pinhole camera and to the burning mirrors of the ancient Mohists, realized experiments with the *camera obscura* and was the first to establish geometrical and quantitative attributes for it.

Between 1000 and 1600, some authors as Ibn al-Haytham, Gemma Frisius, and Giambattista della Porta wrote on the pinhole camera, explaining why the images are upside down. Great advantage in the use of pinhole devices was provided by the safety for the eyes in solar eclipse observations because the event is observed indirectly and this can provide security measure for eye retina.

It was not until 1850 that the Scottish scientist Sir David Brewster took the first photograph with a pinhole camera.

One of the most famous historical testimony of the geometric process for image formation in a pinhole camera has been nicely illustrated by Albrecht Dürer in 1525 through his woodcut shown in Figure .

3.1.2. The prospective acquisition system

The most common model used for camera calibration systems, normally called pinhole camera, is here described. The image formation process is completely determined by choosing a perspective projection center called *optical center* and a retinal plane (*image plane*). The projection of a scene point is then obtained as the intersection of a line passing through the considered point and the center of projection $\bar{c}$ with the retinal plane Π.

Intrinsic parameters

The point P (see Figure) having coordinates (x, y, z) in the reference frame centered in the optical center c and oriented with z axis hortogonal to image plane Π, defines on it a *projection point* (x_p, y_p) whose coordinates can be simply calculated by the relations:

$$\begin{cases} (x_p - x_c)z = fx \\ (y_p - y_c)z = fy \end{cases}$$

where (x_c, y_c) are the coordinates of the *principal point*, intersection of the optical axis and the image plane, and f is the focal length, that is the distance between the optical center c and the image plane.

The projection of the point on the image plane can be represented by the

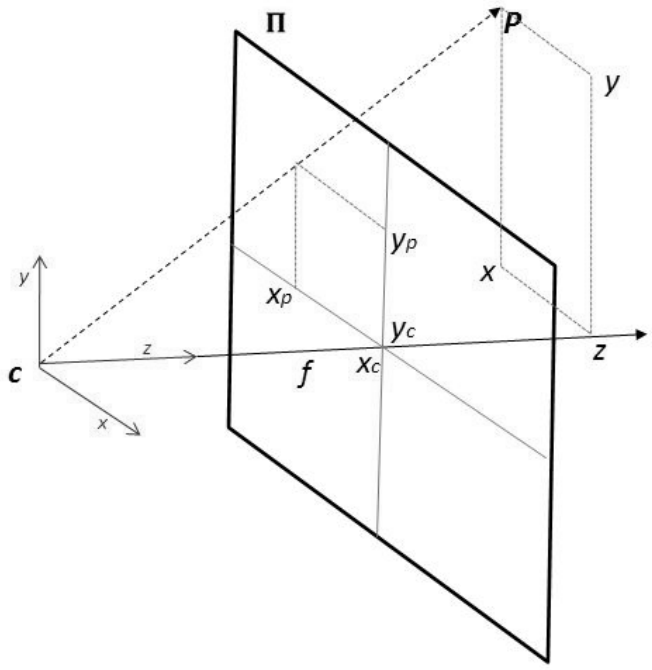

Figure *The scheme represents the projection of the point P with coordinates (x,y,z) in the reference frame of the camera on the image plane* Π *identifying the projection point* (x_p, y_p).

so called *Intrinsic Matrix operator*:

$$\widetilde{K} = \begin{bmatrix} f & & x_c \\ & f & y_c \\ & & 1 \end{bmatrix} \rightarrow \begin{bmatrix} x_p \\ y_p \\ 1 \end{bmatrix} \propto \widetilde{K} \begin{bmatrix} x \\ y \\ z \end{bmatrix} \qquad ()$$

in which the zero values are omitted. The coordinates of a projected point $\{x_p, y_p\}$ are obtained, as expressed in (), by simply multiplying the 3D vector $\{x, y, z\}$ for the *intrinsic matrix* $\widetilde{K}$ and dividing the result for its last term (this is the cause of the presence of the parallel operator $\propto$ in the equation). Equation () can also be written as:

$$\begin{bmatrix} x_p \\ y_p \\ 1 \end{bmatrix} \times \widetilde{K} \begin{bmatrix} x \\ y \\ z \end{bmatrix} = 0$$

Nonlinear intrinsic parameters such as lens distortion are also important although they cannot be included in the linear camera model described by the intrinsic parameter matrix. Many modern camera calibration algorithms estimate these intrinsic parameters as well[1].

These techniques will be explained with more details in the following sections; here we give a more complete overview of the pinhole camera still expressed in () without any remark to effective camera structure.

Equation () does not consider the presence of a pixel grid and transpose metrical terms $\{x, y, z\}$ to $\{x_p, y_p\}$ which are still in a metrical definition.

To define the correct transformation, however, we need to analyze a discrete digital image. Considering the digital structure of the image characterized by a pixel grid with a sensor pixel size of (p_x, p_y) we can transform () in:

[1] Classical method for camera calibration is to acquire different photos of the same target in different positions. The target used in these processes has to respect two fundamental points:

- it has to be well known both from a topological or metrical point of view. Accuracy in the knowledge of the target defines the precision of the calibration .

- it needs texture features well recognizable in the images

These two requirement have historically brought imaging community to choose as classical target a simple chessboard or a cube (topologically more complete) formed by chessboards.

$$K = \begin{bmatrix} f_x & s & \widetilde{x_c} \\ & f_y & \widetilde{y_c} \\ & & 1 \end{bmatrix} \rightarrow \begin{bmatrix} i_p \\ j_p \\ 1 \end{bmatrix} \propto K \begin{bmatrix} x \\ y \\ z \end{bmatrix} \qquad ()$$

where:
$$\begin{cases} f_x = \frac{f}{p_x} \\ f_y = \frac{f}{p_y} \\ s = \frac{\tan(\alpha) f}{p_y} \end{cases}$$

In this notation f_x and f_y are the focal lengths measured in width and height of the pixels, and s is a factor accounting for the skew due to non-rectangular pixels (see Figure). The notation $(\widetilde{x_c}, \widetilde{y_c})$ identifies the principal point position expressed in digital units. It corresponds to $(x_c/p_x, y_c/p_y)$.

K is called **intrinsic matrix**.

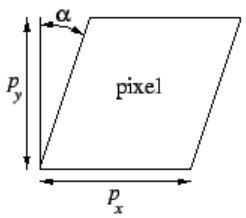

Figure *Pixel, normally rectangular, can actually be irregular and the angle of inclination of the vertical side give the screws effect in ().*

For a camera with fixed optics these parameters are identical for all the acquired images. For cameras which have zooming and focusing capabilities the focal length can obviously change, and also the principal point can vary depending on the scaling factor of the image. An extensive discussion on this subject can be found in the work of Willson[WIL93].

Extrinsic parameters

Moving to a reference frame different from the camera one, we can correct equation () by introducing the rototraslation transformation from the camera reference frame to the new one. Defining this transformation R and $\boldsymbol{c}$ as the optical center in the new reference frame we can write[2]:

$$\begin{bmatrix} \bar{J} \\ 1 \end{bmatrix} \propto K\, R\, (\boldsymbol{x} - \boldsymbol{c}) \qquad ()$$

[2] Let us remember (see Notations) that we identify bidimensional vectors with the straight accent and tridimensional ones with bold case.

where $\boldsymbol{x}$ is the 3D vector representing the point (x, y, z) from (), $\bar{J}$ the 2D vector representing the projection coordinates (i_p, j_p) in pixel units. In a more compact way, we can define the *Complete Projection Matrix* P, element of $\mathcal{M}_{3\times4}$ [3], as:

$$P = K\,R\,[\,I \quad |-\boldsymbol{c}]$$

such that

$$\begin{bmatrix}\bar{\mathrm{J}}\\1\end{bmatrix} \propto \mathrm{P}\begin{bmatrix}\mathbf{X}\\1\end{bmatrix} \qquad ()$$

Until now we have solved the problem of associating to a 3D point $\mathbf{x}$ his projection $\bar{J}$. We now consider the inverse problem. It is useful to understand what we can know if only the image coordinates are known.

To simplify the notation we can consider the projection matrix P as the merging of two matrices:

$$P = [M \quad |\,\boldsymbol{m}] \text{ where } \begin{cases} M = KR \in \mathcal{M}_{3\times3} \\ \boldsymbol{m} = -KR\boldsymbol{c} \in \mathcal{M}_{3\times1} \end{cases}$$

Note that in this notation the optical center $\mathbf{c}$ can be written as $\boldsymbol{c} = -M^{-1}m$.

This is the common matrix description of the pinhole camera, very useful for making simple calculations. We direct now our attention to a different point of view.

Vectorial point of view

The coordinates of the point $\mathbf{x}$ clearly are in some geometrical relation with the coordinates of the projection $\bar{J}$. Any point of the image can be associated to a normalized vector $\boldsymbol{v}_J$ which identifies the direction of the image projection with respect to the optical center. See Figure for a better explanation.

[3] Notation $\mathcal{M}_{3\times4}$ represents the set of the matrices with 3 rows and 4 columns.

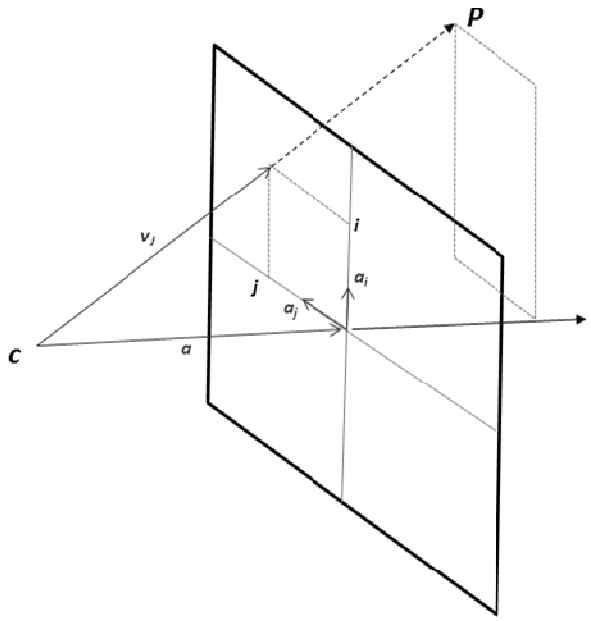

Figure *Scheme of the pinhole model. The point P is projected on the image plane at the coordinate (i,j). The v_j, a, a_i, a_j vectors are representative of the terms used in equation ().*

In this way we can write the equation for the line:

$$l: \mathbf{x} = \boldsymbol{c} + \lambda \boldsymbol{v}_J$$

The definition of the vector $\boldsymbol{v}_J$ comes from the definition of projection matrix:

$$\boldsymbol{v}_J = M^{-1} \begin{bmatrix} J \\ 1 \end{bmatrix} \quad ()$$

As shown in Figure , the vector $\boldsymbol{v}_J$ is the composition of three vectors: a_i, a_j and a . Following equation () we can write:

$$\boldsymbol{v}_J = \boldsymbol{a_i} i + \boldsymbol{a_j} j + \boldsymbol{a} = M^{-1} \begin{bmatrix} i \\ j \\ 1 \end{bmatrix} = R^T K^{-1} \begin{bmatrix} i \\ j \\ 1 \end{bmatrix}$$

$$\boldsymbol{v}_J = \frac{\boldsymbol{x} - \boldsymbol{c}}{\boldsymbol{r_3}(\boldsymbol{x} - \boldsymbol{c})} \quad ()$$

The three vectors a_i, a_j and a, represent the column of the matrix M^{-1}. Note that, dividing the rotational matrix R in rows (so defining the three horizontal vectors r_1, r_2, r_3), vectors a_i, a_j can be written respectively as $\boldsymbol{r_1^T}/f_x$ and $\boldsymbol{r_2^T}/f_y$.

So it is possible to write

$$\boldsymbol{v}_J = \frac{\boldsymbol{r_1^T}}{\boldsymbol{f_x}}\ i + \frac{\boldsymbol{r_2^T}}{\boldsymbol{f_y}} j + (\boldsymbol{r_3^T} - \ \boldsymbol{r_1^T}\frac{x_c}{f_x} - \boldsymbol{r_2^T}\frac{y_c}{f_y})$$

In this way, having the coordinates of the image point $\bar{J}$ and the pinhole camera parameterization, we can define the pointing vector $\boldsymbol{v}_J$ and the line l which connects the point **x** to the optical center **c.**

If we consider a point x observed by a camera, we can describe the stereo system around it by defining a projection plane parallel to the real one. To this end, we can divide matrix M^{-1} in columns $M^{-1} = [\boldsymbol{a_i}, \boldsymbol{a_j}, \boldsymbol{a}]$**.**

The metric system around a point can be described by the three axes:

$$[\bar{\bar{\boldsymbol{a}}}_{\boldsymbol{i}} \quad \bar{\bar{\boldsymbol{a}}}_{\boldsymbol{j}} \quad \bar{\bar{\boldsymbol{a}}}\,] = R^T K^{-1} \boldsymbol{r_3}(\,\boldsymbol{x} - \boldsymbol{c}) \qquad ()$$

or rather:

$$\begin{cases} \bar{\bar{\boldsymbol{a}}}_{\boldsymbol{i}} = \dfrac{\boldsymbol{r_1^T}}{\boldsymbol{f_x}} \boldsymbol{r_3}(\,\boldsymbol{x} - \boldsymbol{c}) \\ \bar{\bar{\boldsymbol{a}}}_{\boldsymbol{j}} = \dfrac{\boldsymbol{r_2^T}}{\boldsymbol{f_y}}\ \boldsymbol{r_3}(\,\boldsymbol{x} - \boldsymbol{c}) \\ \bar{\bar{\boldsymbol{a}}} = \left(\boldsymbol{r_3^T} - \ \boldsymbol{r_1^T}\dfrac{x_c}{f_x} - \boldsymbol{r_2^T}\dfrac{y_c}{f_y}\right)\boldsymbol{r_3}(\,\boldsymbol{x} - \boldsymbol{c}) \end{cases}$$

Note that $\bar{\bar{\boldsymbol{a}}}$ is not orthogonal to the plane defined by the vectors $\bar{\bar{\boldsymbol{a}}}_{\boldsymbol{i}}$ **,** $\bar{\bar{\boldsymbol{a}}}_{\boldsymbol{j}}$**.**

Figure shows the best approximation of the projection system around a point x .

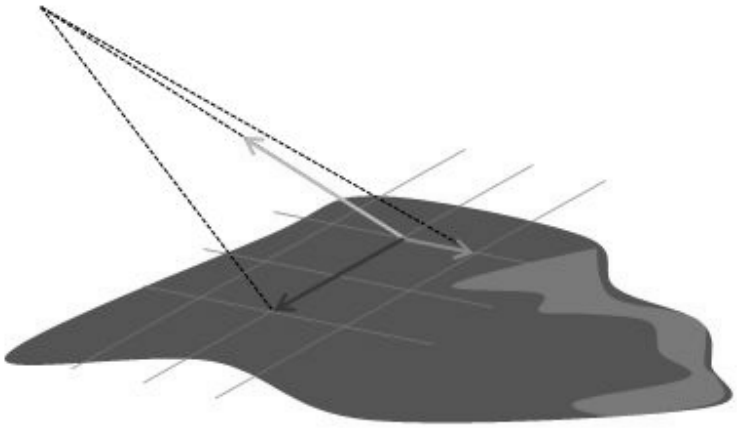

Figure *The image shows how is it possible to trace an image plane (the transparent grid) around a point defined by the three vectors* $\boldsymbol{v_i}$*(left one)* $\boldsymbol{v_j}$*(button one) and* $\boldsymbol{v_J}$*i(versus top one).*

The description of the projective system from a vectorial point of view con be considered completed. We analyze now the singular case in which the focal length can be considered equal to infinity.

Orthogonal projection

The orthogonal projection systems can be extended by imposing the focal length equal to infinity or in another way the orthogonal systems are systems in which the projection lines can be considered parallel as in improper beam .

In equation () the parallel operator allows to divide the matrix by an arbitrary value f . Under this condition we can write equation () as:

$$\begin{bmatrix} \bar{J} \\ 1 \end{bmatrix} \propto \begin{bmatrix} \frac{1}{p_x} & \frac{\tan(\alpha)}{p_y} & \frac{x_c}{f p_x} \\ & \frac{1}{p_y} & \frac{y_c}{f p_y} \\ & & \frac{1}{f} \end{bmatrix} R\,(\boldsymbol{x} - \boldsymbol{c})$$

Imposing the focal length equal to infinity[4] we obtain

$$\boldsymbol{lim_{f\to\infty}} \rightarrow \quad \bar{J} = \begin{bmatrix} \frac{1}{p_x} & \\ & \frac{1}{p_y} \end{bmatrix} \begin{bmatrix} \boldsymbol{r_1} \\ \boldsymbol{r_2} \end{bmatrix} (\boldsymbol{x} - \boldsymbol{c})$$

Defining the intrinsic matrix K_2 as the diagonal matrix of the scale factors, we can write

$$\bar{J} = K_2 \begin{bmatrix} \boldsymbol{r_1} \\ \boldsymbol{r_2} \end{bmatrix} (\boldsymbol{x} - \boldsymbol{c})$$

where r_1, and r_2 are the first two rows of the rotation matrix R. As shown in Figure they represents the axes of the image plane. It is clear that this equation is not unique to represent the same orthogonal map: for instance, we can use any $\boldsymbol{c} + \lambda r_3$ instead of $\boldsymbol{c}$.

$$\bar{J} = K_2 \begin{bmatrix} \boldsymbol{r_1} \\ \boldsymbol{r_2} \end{bmatrix} \mid K_2^{-1} \begin{matrix} x_c \\ y_c \end{matrix} \begin{bmatrix} \boldsymbol{x} \\ 1 \end{bmatrix}$$

where $\{ x_c = -r_1\boldsymbol{c}$ and $y_c = -r_2\boldsymbol{c} \}$, represents the coordinates of the center in digital units on the projective plane.

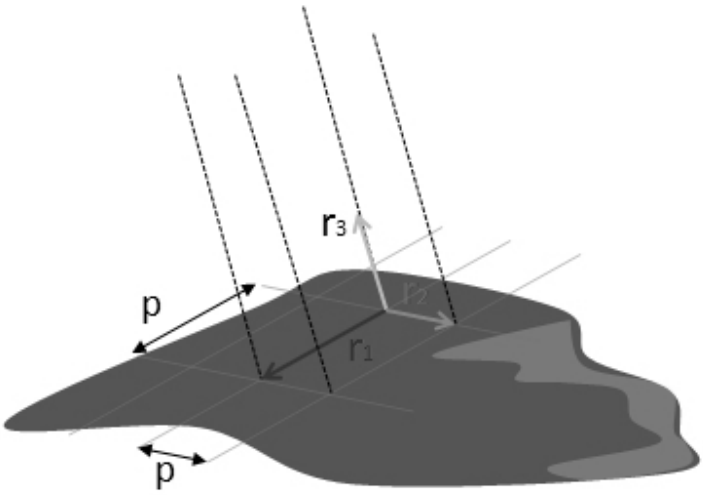

Figure *Scheme of the orthogonal projection. Point x is projected on the image plane and then decomposed in its component $r_1 e\ r_2$. Each term is then scaled with grid dimension p.*

[4] This is equivalent to consider the hypothesis that the projection line on the surface are almost parallel.

From projective to orthogonal

Considering that orthogonal case is easier to be managed than projective one we approximate the second one with the first one around a known point.

Equation (7) suggests an approximation in the orthogonal system $\bar{J} = G(\boldsymbol{x})$ to be used in the projective one $\bar{J} = P(\boldsymbol{x})$. Knowing the position of a point $\boldsymbol{x_m}$ and its projection $\overline{J_m}$ on the image, we can deduct a local orthogonal projection which can be used to approximate the projection as orthogonal case.

The coordinates $\bar{J}$ have to be predicted by a linear transformation G which equals to $\overline{J_m}$ in $\boldsymbol{x_m}$.

This transformation can be totally defined by two not yet defined 3D vectors $\boldsymbol{s_i}, \boldsymbol{s_j}$ in the form:

$$\bar{J} = G(\boldsymbol{x}) = \begin{bmatrix} \boldsymbol{s_i^T} \\ \boldsymbol{s_j^T} \end{bmatrix} (\boldsymbol{x} - \boldsymbol{x_m}) + \overline{J_m} \qquad ()$$

Remembering the definitions given in (), other conditions can be found to characterize the G function.

The first condition depends on the fact that $\overline{\overline{\boldsymbol{a}}}$ is the optical axis of the orthographic system, and this implies that the projection $\bar{J}$ is invariant to movements along this vector.[5]

On the other side, a pixel variation on $\bar{J}$ can be predicted when the movement is along $\overline{\overline{\boldsymbol{a}}}_{\boldsymbol{i}}, \overline{\overline{\boldsymbol{a}}}_{\boldsymbol{j}}$ direction.

Summarizing:

$$\begin{cases} \bar{J}(x + \lambda\overline{\overline{\boldsymbol{a}}}) = \bar{J}(x) \\ \bar{J}(x + \overline{\overline{\boldsymbol{a}}}_{\boldsymbol{i}}) = \bar{J}(x) + \begin{bmatrix} 1 \\ 0 \end{bmatrix} \\ \bar{J}\left(x + \overline{\overline{\boldsymbol{a}}}_{\boldsymbol{j}}\right) = \bar{J}(x) + \begin{bmatrix} 0 \\ 1 \end{bmatrix} \end{cases}$$

This means that $\boldsymbol{s_i} \propto \overline{\overline{\boldsymbol{a}}} \times \overline{\overline{\boldsymbol{a}}}_{\boldsymbol{j}}$ and that $\boldsymbol{s_j} \propto \overline{\overline{\boldsymbol{a}}} \times \overline{\overline{\boldsymbol{a}}}_{\boldsymbol{i}}$. To define the system () we need to find an explicit for of $\boldsymbol{s_i}, \boldsymbol{s_j}$. The new results allow to write:

[5] See Figure for the definition of vectors.

$$\begin{bmatrix} \boldsymbol{s_i^T} \\ \boldsymbol{s_j^T} \end{bmatrix} [\bar{\bar{\boldsymbol{a}}}_{\boldsymbol{i}} \quad \bar{\bar{\boldsymbol{a}}}_{\boldsymbol{j}} \quad \bar{\bar{\boldsymbol{a}}}] = \begin{bmatrix} 1 & 0 & 0 \\ 0 & 1 & 0 \end{bmatrix}$$

$$\downarrow$$

$$\begin{bmatrix} \boldsymbol{s_i^T} \\ \boldsymbol{s_j^T} \end{bmatrix} = \frac{\begin{bmatrix} 1 & 0 & 0 \\ 0 & 1 & 0 \end{bmatrix} KR}{q_{(\boldsymbol{x_m})}}$$

where $q_{(\boldsymbol{x_m})} = \boldsymbol{r_3}(\boldsymbol{x} - \boldsymbol{c})$ and where we use the definition of matrix $[\bar{\bar{\boldsymbol{a}}}_{\boldsymbol{i}} \quad \bar{\bar{\boldsymbol{a}}}_{\boldsymbol{j}} \quad \bar{\bar{\boldsymbol{a}}}]$ readable in ().

So we can write[6]:

$$\bar{J} = G(\boldsymbol{x}) = \frac{K_{2\times3}R}{q_{(\boldsymbol{x_m})}}(\boldsymbol{x} - \boldsymbol{x_m}) + \frac{K_{2\times3}R}{q_{(\boldsymbol{x_m})}}(\boldsymbol{x_m} - \boldsymbol{c})$$

Although these equations seem to make complicate a simple process as the projective or the orthogonal one, the last equations will result very useful in understanding the approximations used in the definition of this work.

Summarizing:

Considering a projective system $\begin{bmatrix} \bar{J} \\ 1 \end{bmatrix} \propto K\ R\ (\boldsymbol{x} - \boldsymbol{c})$ *, which brings the point* $\boldsymbol{x_m}$ *to the pixel coordinates* $\overline{J_m}$ *, it can be locally approximated around* $\boldsymbol{x_m}$ *as a orthographic system* $\bar{J} = G(\boldsymbol{x})$ *where*

$$G(\boldsymbol{x}) = \frac{K_{2\times3}R}{q_{(\boldsymbol{x_m})}}(\boldsymbol{x} - \boldsymbol{c}) \qquad ()$$

where $q_{(\boldsymbol{x_m})} = \boldsymbol{r_3}(\boldsymbol{x_m} - \boldsymbol{c})$ *and* $K_{2\times3}$ *is the sub-matrix built with the first two rows of the intrinsic matrix*

[6] See Appendixes for other notes.

A generalization

We propose now a different point of view that will be useful in better understanding the final purpose of this work:

We can describe the target as a triplette $\{\mathcal{S}, \mathbb{C}, \bar{s}\}$ where:	
$\mathcal{S}$	is the map $\Omega^{\mathbb{R}}_{\mathbb{R}^2}$ which associates to all the pairs of ground coordinates x, y the elevation $z = \mathcal{S}(x, y)$ of the corresponding point
$\mathbb{C}$	is map $\Omega^{\mathbb{R}}_{\mathbb{R}^2}$ which associates to all the ground coordinates (x,y) the *effective albedo* (see Section 3.2.3) of the corresponding surface point $\rho = \mathbb{C}(x, y)$.
$\bar{s}$	is the versor identifying the direction of the illumination source, considered as point-like and located at infinity.
In absence of *variegation*[7], the image process can be described by the following equation: $$I_1(\bar{x}) = P_1(\mathcal{S}, \mathbb{C}, \bar{s})$$ where P_1 can be defined as the *projective function*.	

Schedule *Generalization model for the acquisition camera systems for open surface.*

In this way if the target is an open surface that be expressed as a injective map between the on ground grid and the elevation value ($z = \mathcal{S}(x, y)$), by knowing both local effective albedo ($\rho = \mathbb{C}(x, y)$) and the invariant direction of a point light ($\bar{s}$) we can express the acquisition system for all the possible positions or pointing of the camera.

[7] The absence of variegation can be considered in the hypothesis of homogeneous land target.

3.2. 3D reconstruction methods

If in the previous section we dwelled on the mathematical models describing the monocular view based on a pinhole approximation and the consequences that could emerge by approximating a projective system to an orthogonal one around a 3D point, this section will explain the models used to play with 3D information in case more acquisition systems can be applied to the same target. Redundancy is not the kernel of the issue but rather the different kind of information we can obtain by having different points of view and how this can be used in the inverse projective problem.

Different methods for the 3D reconstruction are presented and particular attention is given to solving the stereo problem. Moreover, considering the reconstruction of small bodies as another possible application, also other methods as “segmentation” and “shape from silhouettes” are presented.

3.2.1. Stereo method

As well known in physiology, one of the processes used by human brain for the detection of external geometry is the use of eyes to apply a triangulation system.

A stereo vision is the capability to sense the depth of the observed scene. The human vision is capable to see the depth and to distinguish the distances of different objects, thanks to the fact that humans have two eyes. Human eyes are located on the same horizontal line, and the brain gets almost the same picture from both eyes, but with the picture elements horizontally shifted one relative to other. Each object in the scene is shifted differently, depending on the physical distance to the object and this effect is called photogrammetry parallax. Our brain extracts the depth information from these different shifts: in fact, the different position of the projection of a same target on the two retinal spaces supply the parallax information, making it able to determine the distances between the eyes and the target.

In human perception, the stereo process is limited to the so called next-vision or, to be more precise, to a range of about ten meters. This fact comes out from the bound distance between the two eyes which, as described in this section, does not allow to the stereo human vision better performance.

Baseline geometrical model and epipolar geometry

In analytical way, the geometrical vinculum imposed by () can be written as:

$$\begin{cases} \mathbf{J_1} \propto \mathrm{P}_1 \begin{bmatrix} \mathbf{X} \\ 1 \end{bmatrix} \\ \mathbf{J_2} \propto \mathrm{P}_2 \begin{bmatrix} \mathbf{X} \\ 1 \end{bmatrix} \end{cases} \qquad ()$$

where we introduced $\mathbf{J_1}, \mathbf{J_2}$ to simplify the notation, indicating the 3D coordinates of the projection points on the retinal plane (with z=1).

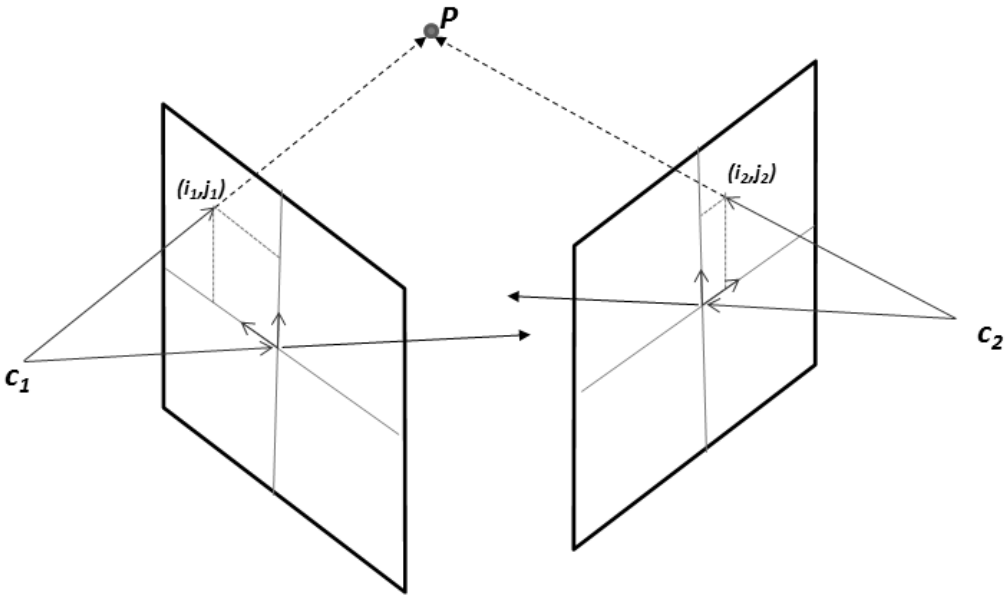

Figure *Scheme for the projection of a 3D point P on two different acquisition systems representing a stereo-baseline.*

The expression in () can be written as a complete system by dividing the projective matrix in four sub-matrices, separating the first two rows from the third one and the first three columns from the last one. The resulting matrix $\mathrm{P_i}$ is the composition of matrices M_i, m_i and N_i, n_i: $M_i \in \mathcal{M}_{2\times3}$ and $m_i \in \mathcal{M}_{2\times1}$ define the first two rows, while $N_i \in \mathcal{M}_{1\times3}$ and $n_i \in \mathcal{M}_{1\times1}$ define the last one.

With these substitutions, equation (11) can be written as:

$$\begin{cases} \mathbf{J_1}[\mathrm{N_1}|\mathrm{n_1}]\begin{bmatrix}\mathbf{X}\\1\end{bmatrix} = [\mathrm{M_1}|\mathrm{m_1}]\begin{bmatrix}\mathbf{X}\\1\end{bmatrix} \\ \mathbf{J_2}[\mathrm{N_2}|\mathrm{n_2}]\begin{bmatrix}\mathbf{X}\\1\end{bmatrix} = [\mathrm{M_2}|\mathrm{m_2}]\begin{bmatrix}\mathbf{X}\\1\end{bmatrix} \end{cases}$$

This brings to final writing:

$$\begin{bmatrix}\mathbf{J_1}\mathrm{N_1} - \mathrm{M_1}\\ \mathbf{J_2}\mathrm{N_2} - \mathrm{M_2}\end{bmatrix}\mathbf{x} = \begin{bmatrix}\mathrm{m_1} - \mathbf{J_1}\mathrm{n_1}\\ \mathrm{m_2} - \mathbf{J_2}\mathrm{n_2}\end{bmatrix} \qquad ()$$

The system in () allows to solve the triangulation[8] problem using OLS (ordinary least square). In fact, given a couple of stereo images, knowing the coordinates of all the points in one image corresponding to the points of the other, it is possible to calculate the 3D coordinates of these points and generate a 3D model of the acquired target.

As previously done for the simplest case of monocular view, we can even apply a local approximation to not projective system obtaining from () and ():

$$\begin{aligned} \bar{J_1} &= \frac{K_{2\times3}R_1}{q_{1_{(\boldsymbol{x_m})}}}(\boldsymbol{x}-\boldsymbol{c_1}) \\ \bar{J_2} &= \frac{K_{2\times3}R_2}{q_{2_{(\boldsymbol{x_m})}}}(\boldsymbol{x}-\boldsymbol{c_2}) \end{aligned} \qquad ()$$

After the process of triangulation a 3D model of the scene can be created. In photogrammetric field this model is called Digital Terrain Model (DTM)[9].

All these considerations allow to determine the effective 3D position (with some tolerances that we will describe later) of a point knowing the acquisition camera parameters, the relative geometry and the correspondences between all the points of the first image and the so called *homologous*[10] on the second one.

The aim of the stereo matching methods in digital stereo systems is to solve the so-called *correspondence problem*, that is to find what are the homologous points in two stereo images and mapping the relative differences. The map between the points of the first image to the *homologous points* on the second image is called *disparity map* $\mathfrak{D}$; it belongs to $\Omega_{\mathrm{H_1}\times\mathrm{W_1}}^{\mathrm{H_2}\times\mathrm{W_2}}$, where H and W represent the height and the width of one of the images.

[8] The system presented in () has as solution the 3D point which minimizes the error of the system. However in photogrammetry it is a rule considering "fixed" the coordinates of one of the images and to minimize the error only on the coordinates of the other image.

[9] The first Digital Elevation Model (DEM), or DTM since it was applied to the Earth, in astronautic field was produced on February 22, 1986 by SPOT 1 (Satellite Pour l'Observation de la Terre), a high-resolution, optical imaging Earth observation satellite system. SPOT 1 transmitted Earth surface images with a spatial resolution of 10 or 20 meters, providing the first usable data of a sizeable portion of the planet landmass for realizing a DTM.

[10] Etymology from Greek *omos*=equal and *logos*=concept, in this case referred points in different images representing the same features.

A generalization

We can describe the target as an open surface and define the stereo system as a triplette $\{\mathcal{S}, \mathbb{C}, \bar{s}\}$ where:

$\mathcal{S}$	is the map $\Omega^{\mathbb{R}}_{\mathbb{R}^2}$ which associates the elevation $z = \mathcal{S}(x,y)$ to all pairs of ground coordinates (x,y)
$\mathbb{C}$	is the map $\Omega^{\mathbb{R}}_{\mathbb{R}^2}$ which associates the *effective albedo* $\rho = \mathbb{C}(x,y)$ (see section 3.2.3) to all the ground coordinates (x,y) $\rho = \mathbb{C}(x,y)$.
$\bar{\boldsymbol{s}}$	is the versor identifying the direction of the source of illumination considered as point-like and located at infinity.
The stereo process can be described by the following equations: $$I_1(\bar{x}) = P_1(\mathcal{S}, \mathbb{C}, \bar{\boldsymbol{s}})$$ $$I_2(\bar{y}) = P_2(\mathcal{S}, \mathbb{C}, \bar{\boldsymbol{s}})$$ $$I_1(\bar{x}) \simeq I_2(\bar{y}) \quad \text{where} \quad \bar{y} = \mathfrak{D}(\bar{x})$$	
$\mathfrak{D}$ is called disparity map of the system.	

Schedule *Generalization model for a stereo acquisition camera systems for open surface.*

One of the major problems in this description of the method, and more generally of all the stereo methods, is the operator $\simeq$ in the last formulation.

What is the meaning of "similar" or "quite equal" in two images? Two areas, one per image, can be considered similar in case they represent the same "concept" or "logo" but how to determine for each point of the first image what is the most similar on the second one is not a well posed question.

Differences of intensity and chrominance due to slope of the target, prospective points of view, rotation and noise make very complicate the definition of this kind of likeness. Some examples will be presented in Section 2.3.1.

If the aim of the stereo methods is the detection of the disparity map $\mathfrak{D}$, the way to obtain it is recognizing the corresponding features in the images. If most of the methods the human brain uses to define these correspondences are based on mnemonic or intuitive processes, to make this analytically it is necessary to be able to define an "aesthetical" metric.

depicts two pinhole cameras looking at point p with its projection x_R and x_L on the right and left image planes respectively. Since the focal points of the two cameras are distinct, each focal point projects a distinct point into the other camera's image plane: these two image points are denoted by e_L and e_R and are called *epipoles* or *epipolar points*. Both epipoles e_L and e_R in their respective image planes and both focal points c_L and c_R lie on a single line.

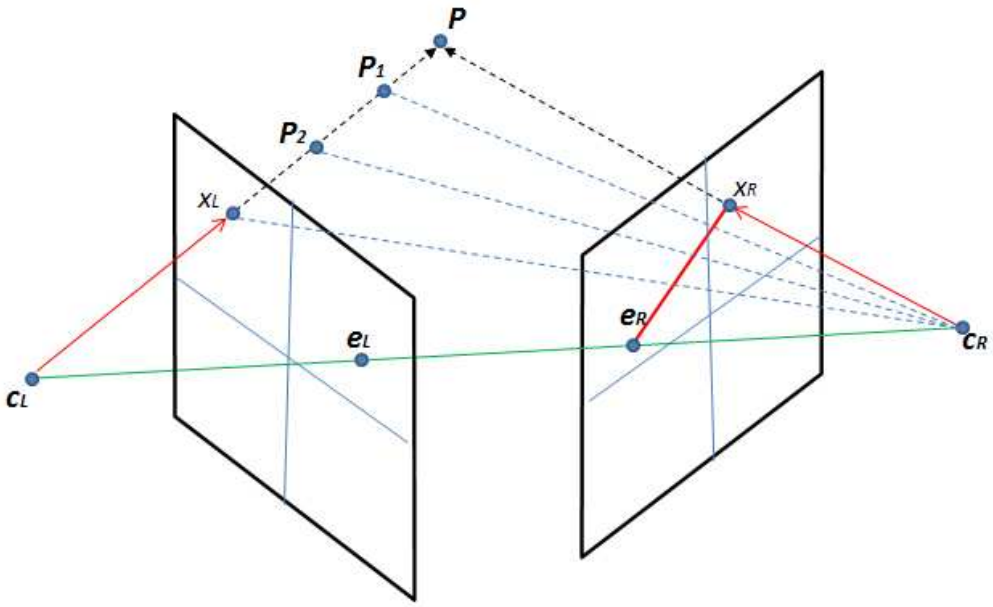

Figure *Epipolar geometrical model. In red the vectors that identify the epipolar plane associated to the projection line for point P. The connection between the two focal centers is called epipolar line and identifies the two points* $e_{L,}$ e_R.

The line $c_L - P$ is seen by the left camera as a point because it is directly connected to that camera's focal point. However, the right camera sees this connection as a line in its image plane. That line $(e_R - x_R)$ in the right camera is called an epipolar line. On the other side, the line $c_R - x$ seen by the right camera as a point is seen as the epipolar line $e_L - x_L$ by the left camera.

An epipolar line (see Figure) is a function of the 3D point X, i.e. there is a set of epipolar lines in both images if we allow P to vary over all the 3D points. Since the 3D line $c_L - P$ passes through camera focal point x_L, the corresponding epipolar line in the right image must pass through the epipole e_R (and

correspondingly for epipolar lines in the left image). This means that all epipolar lines in one image must pass on the epipolar point of that image P.

As an alternative visualization, let us consider the points P, c_L and c_R that form a plane called the *epipolar plane*. The epipolar plane intersects each camera's image plane forming lines—the epipolar lines. All epipolar lines intersect the epipole regardless of where **P** is located.

If the relative translation and rotation of the two cameras is known, the corresponding epipolar geometry leads to two important observations.

If the projection point x_L is known, then the epipolar line e_R–x_R is known and the point p is projected into the right image on a point x_R which must lie on this particular epipolar line. This means that for each point observed in one image the same point must be observed in the other image on a known epipolar line. This provides an epipolar constraint which corresponding image points must satisfy; this constraint can be used to test if two "corresponding" points actually correspond to the same 3D point.

If the points x_L and x_R are known, their projection lines are also known, and if the two image points correspond to the same 3D point p the projection lines must intersect precisely at p. This means that X p can be calculated from the coordinates of the two image points, a process called triangulation.

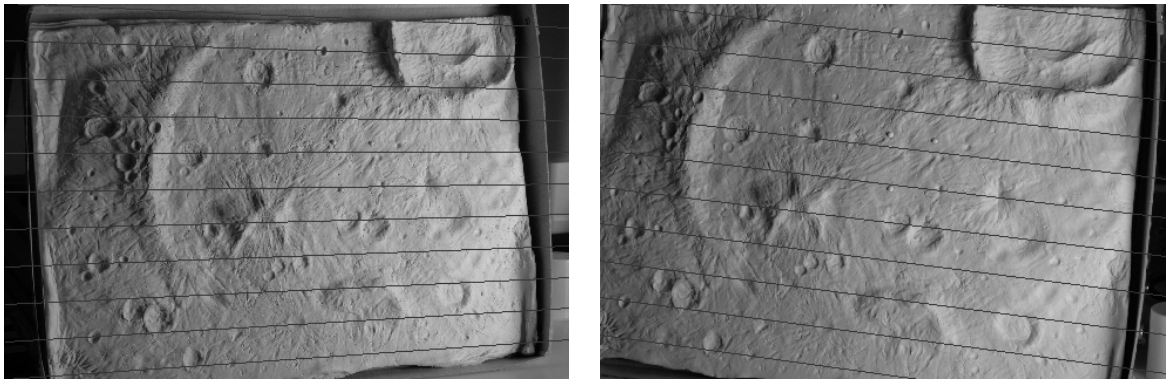

(a) (b)

Figure *Example of epipolar lines for a stereo pair. Images represent a plastic simulation of a crater site. Note that all the points in a line row of image (a) can be found on the corresponding line on image (b).*

The epipolar geometry is simplified if the two camera image planes coincide. In this case, the epipolar lines also coincide ($e_L - x_L = e_R - x_R$). Furthermore, the epipolar lines are parallel to the line $c_L - c_R$

between the focal points, and can in practice be aligned with the horizontal axes of the two images. This means that for each point in one image, its corresponding point in the other image can be found by looking only along a horizontal line. If the cameras cannot be positioned in this way, the image coordinates from the cameras may be transformed to emulate having a common image plane. This process is called image rectification. An example of rectified images is shown in Figure .

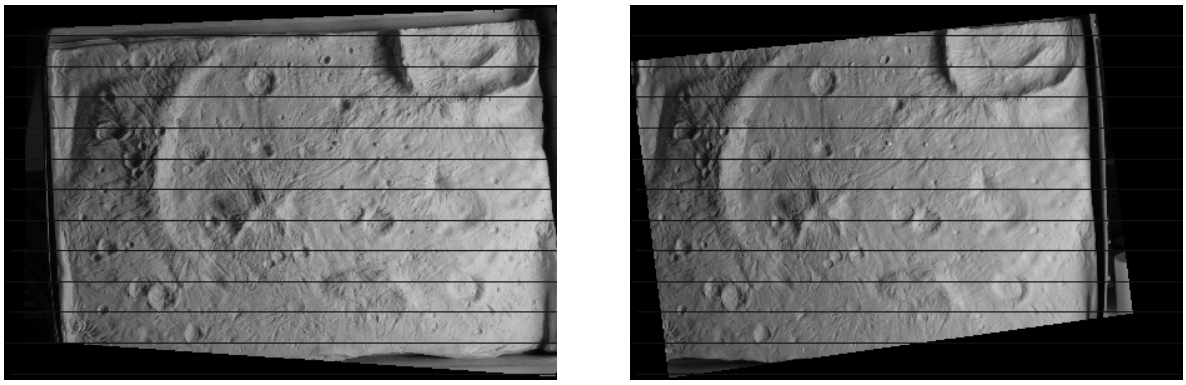

(a) (b)

Figure *Example of epipolar lines for a stereo pair after a process of rectification. Images represent a plastic simulation of a crater site. Note that all the points in a row of image (a) can be found on the corresponding row on image (b)*

For rectified images the disparity function can be considered as a map $\Omega_{H_1 \times W_1}^{H_2}$ reducing the complexity of the problem (see Figure).

Summarizing: we have defined the stereo problem as a correspondence problem, generally helped by the knowledge of the geometrical acquisition system that allows to reduce the terms of the disparity map. To find the correspondences we still need to define some metric which permits to quantify the concept of “similarity” and to optimize the resulting disparity map.

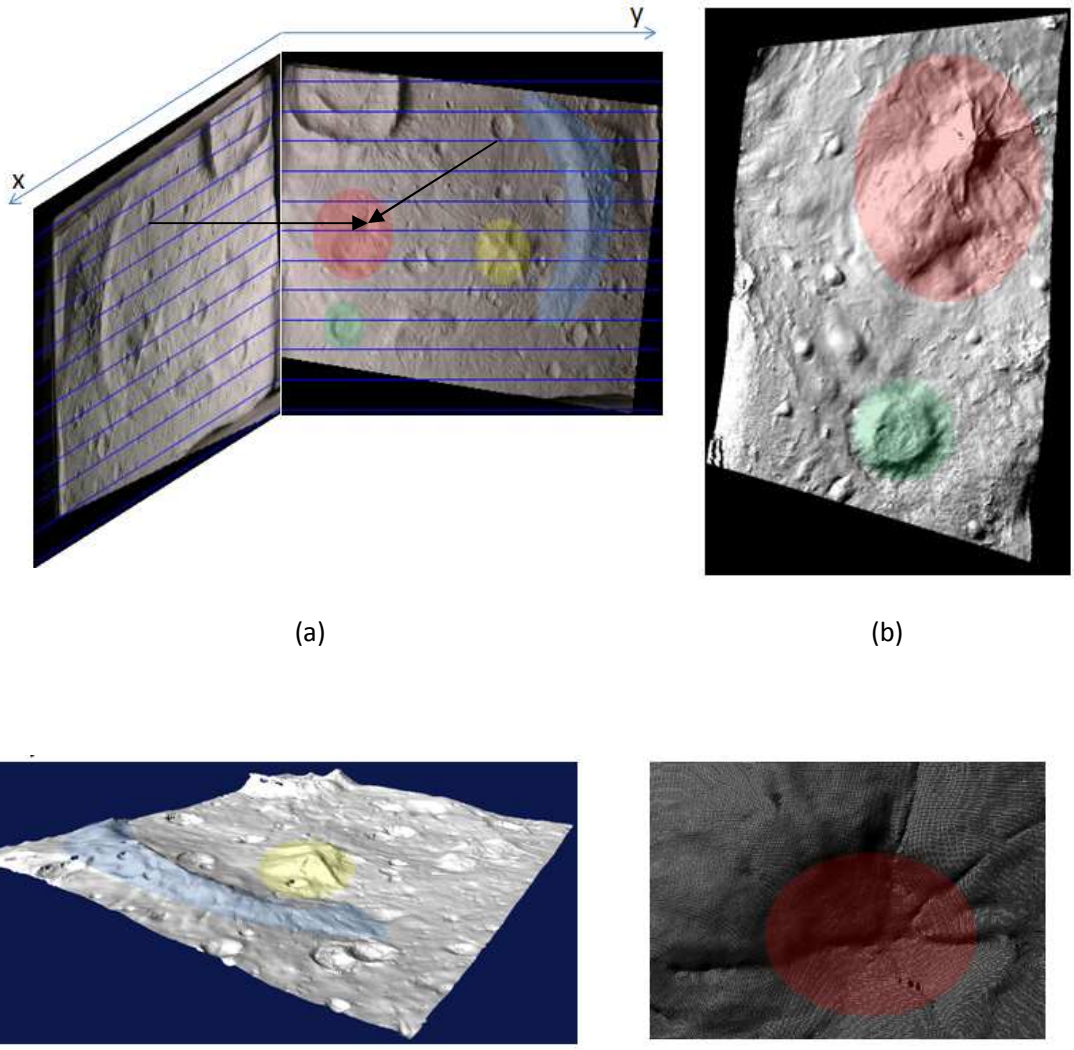

(a) (b)

(c) (d)

Figure *Figure (a) shows that finding the correspondences with rectified images is a one dimensional problem. After having found all the correspondences between the x and y coordinates for all the rows, the triangulation allows to obtain the 3D reconstruction. In figures (b), (c) and (d) the model reconstructions at 3 different levels of precision are shown; colored zones represent the user tool for orienting the partial reconstructions.*

Similarity metrics

Historically, three are the functions normally used to define the similarity between areas in two different images.

The functions we consider here are known as *similarity functions* [KHA07]: they are the sum of squared distance (SSD), the sum of absolute differences (SAD) and the normalized cross correlation (NCC).

Considering a pixel on one image having coordinates i_1, j_1, we can define around it a window of "radius" w as the subset $I_1(i_1 + k, j_1 + h)$ with $k, h \in \{-w, -w+1, \dots, w-1, w\}$. In a similar way, another window can be defined on the second image around a point i_2, j_2. Under these hypotheses we can write:

$$
\begin{aligned}
SSD_{\{I_1,I_2\}}(i_1 j_1, i_2 j_2) &= \sqrt{\sum_{k,h=-w}^{w} \big(I_1(i_1 + k, j_1 + h) - I_2(i_2 + k, j_2 + h)\big)^2} \\
SAD_{\{I_1,I_2\}}(i_1 j_1, i_2 j_2) &= \sum_{k,h=-w}^{w} \|I_1(i_1 + k, j_1 + h) - I_2(i_2 + k, j_2 + h)\| \\
NCC_{\{I_1,I_2\}}(i_1 j_1, i_2 j_2) &= \sum_{k,h=-w}^{w} \overline{\overline{I_1}}(i_1 + k, j_1 + h) \cdot \overline{\overline{I_2}}(i_2 + k, j_2 + h)
\end{aligned}
$$

where we have indicated with $\overline{\overline{I_i}}$ the image with its local mean and variance normalized.

Unless the first and the second metrics are really faster, NCC is the most used one and will be adopted also in this work. The reason for this choice is that SSD and SAD are more affected by image noise and by differences in illumination between the two images.

NCC values range between –1, when the two images are complementary or rather the pixel by pixel of the images is always 1, to 1 when they are equal.

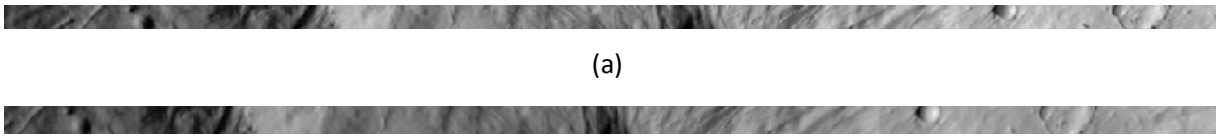

(a)

(b)

Figure *Two corresponding sections of the two rectified images in Fig. 11. Note that all the features shown in section (a) can be seen also on section (b).*

As an example of application of NCC to find similarities between two images, we can consider the two rectified images in Figure . As previously discussed, rectified images can be compared row by row, so the problem is reduced to analyze the correlation between two one-dimensional images. For comparing the results of using different types of metric, and for sake of simplicity, we can extract from these images two corresponding strips, as shown in Figure. 12, and then apply the different correlation filters.

The obtained results are shown in Figure , 15 and 16. These images show the value of the similarity function, expressed as a pseudo-color map, when comparing any local part of the strips. Note in all the cases the presence of a more or less diagonal path defining the correct correspondence between the two strips.

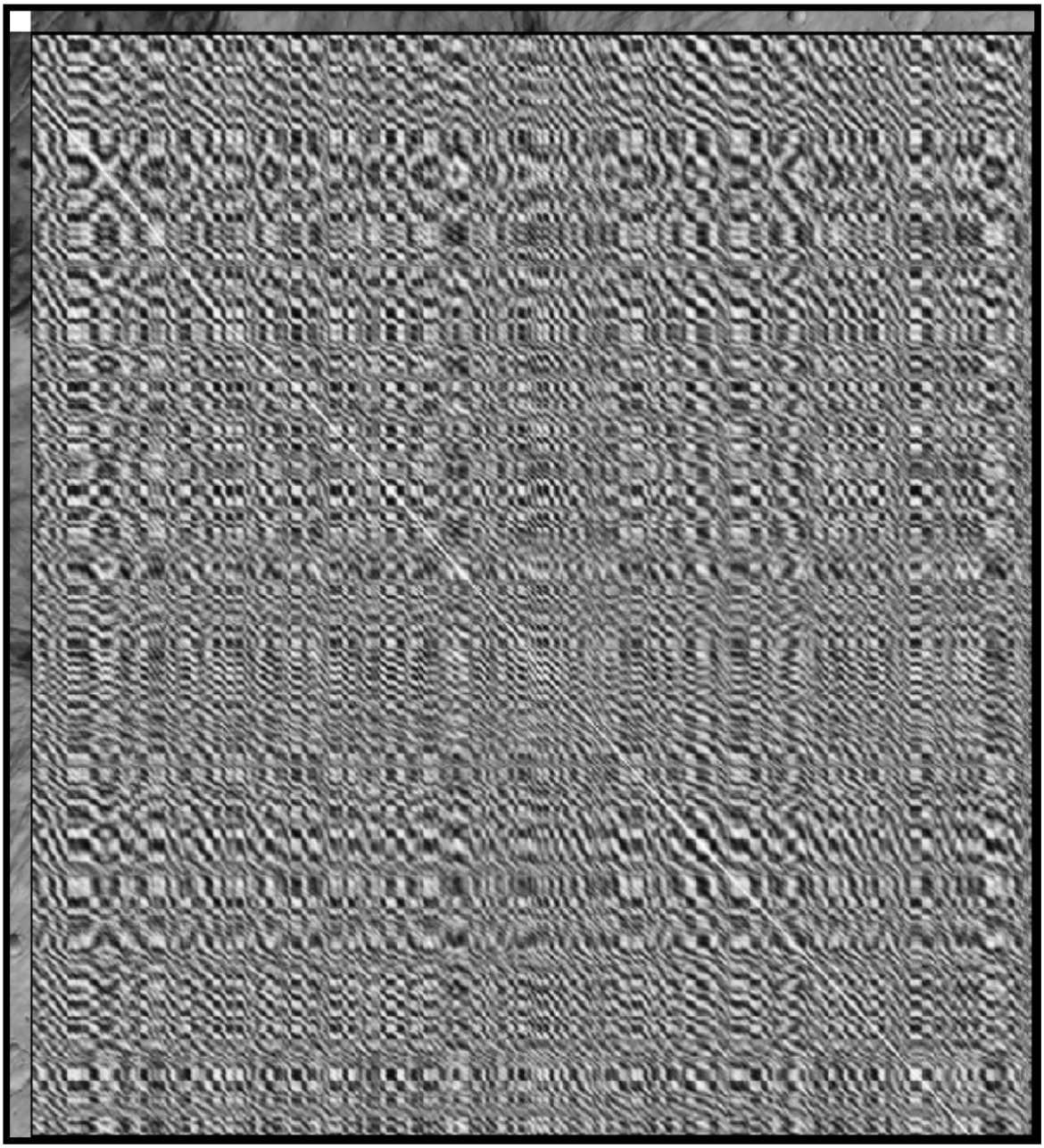

Figure *This image shows the result of the application of the NCC (central square) to the two selected strips assuming a 7 pixel window-matching. The two strips are shown on the top (Figure .a) and on the left (Figure .b) of the image. The searched correspondence is rather evident as a white diagonal path.*

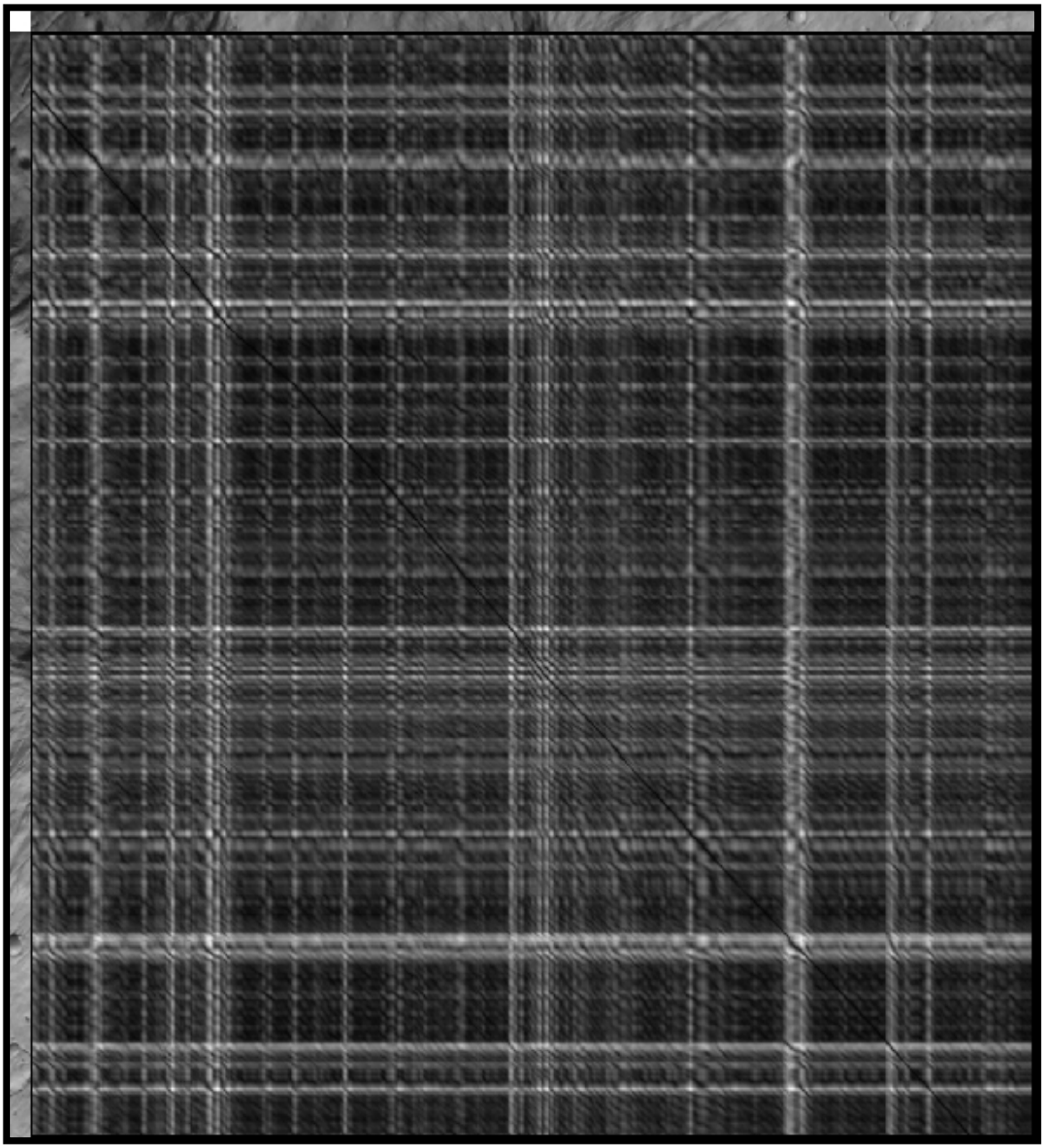

Figure *As* Figure *, but having applied the SAD or SSD (quite similar results) instead of NCC. Differently from NCC, the disparity is seen as a black path because the optimal value is reached where the similarity function reaches the zero.*

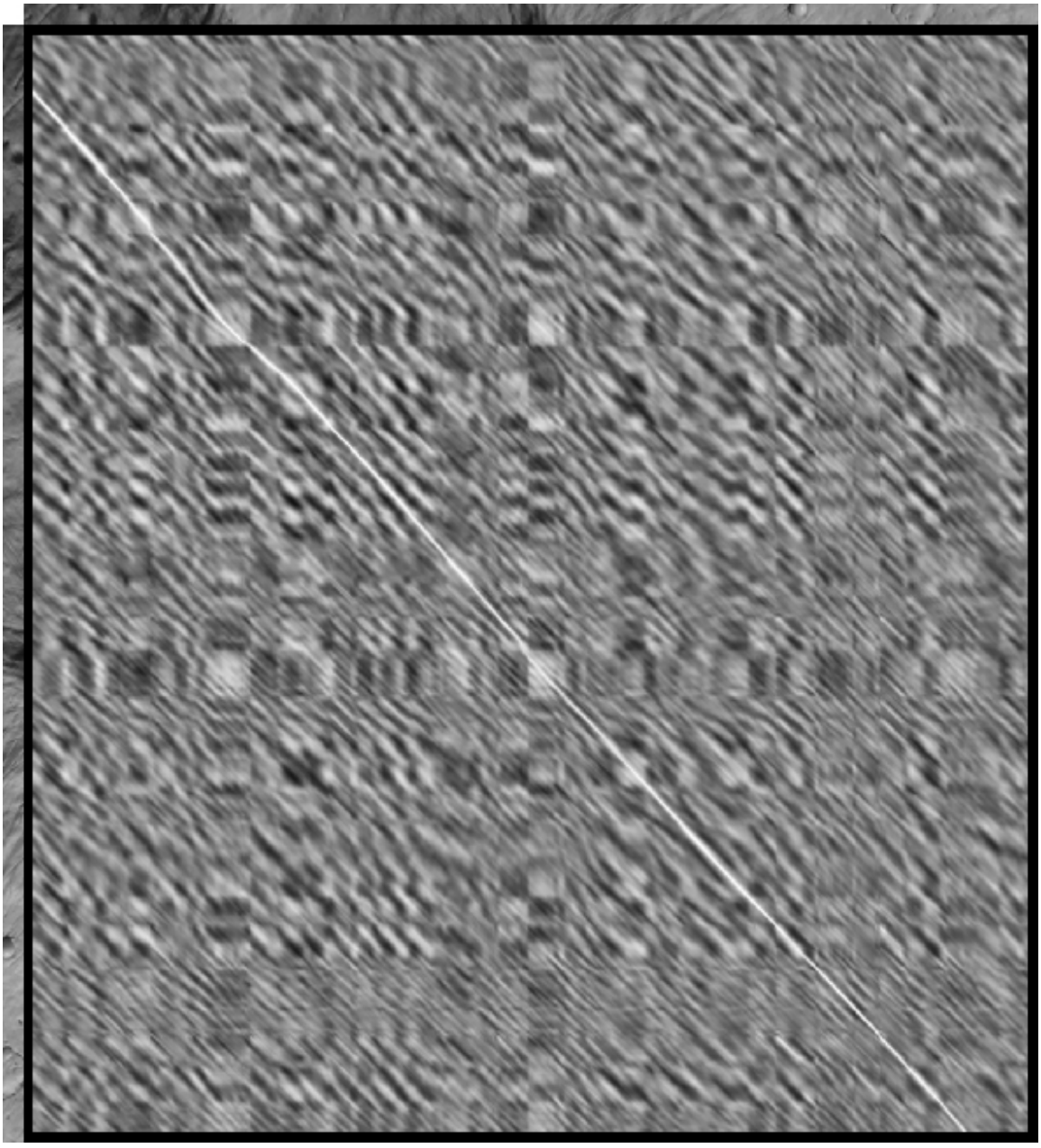

Figure *As* Figure *, but having applied a 21 pixel window-matching. On one side, increasing the window size and consequently the amount of information makes the path we are looking for more evident; but on the other side it introduces a low pass filter making less sharp and defined the searched correspondence path.*

Problems

If we approximate locally the disparity map as linear we can consider all the correspondences as due to local homographies (transformation between two projective planes). The homografies introduce a great problem on using the classical similarity functions because they are not spatial-invariant. Zoom effects, surface slope or prospective differences make not robust the uniform use of the similarity function and they have historically forced to use methods adopting matching windows different in dimensions and shape [KAN94]. Moreover, different response to illumination due to material and slope, the possible saturation, and the presence of shadow or self-shadow normally introduce other problems when using these functions (see Figure).

An overview of the most frequent problems which have to be considered in the stereo approach about the use of the similarity function is well explained by the example in Figure .

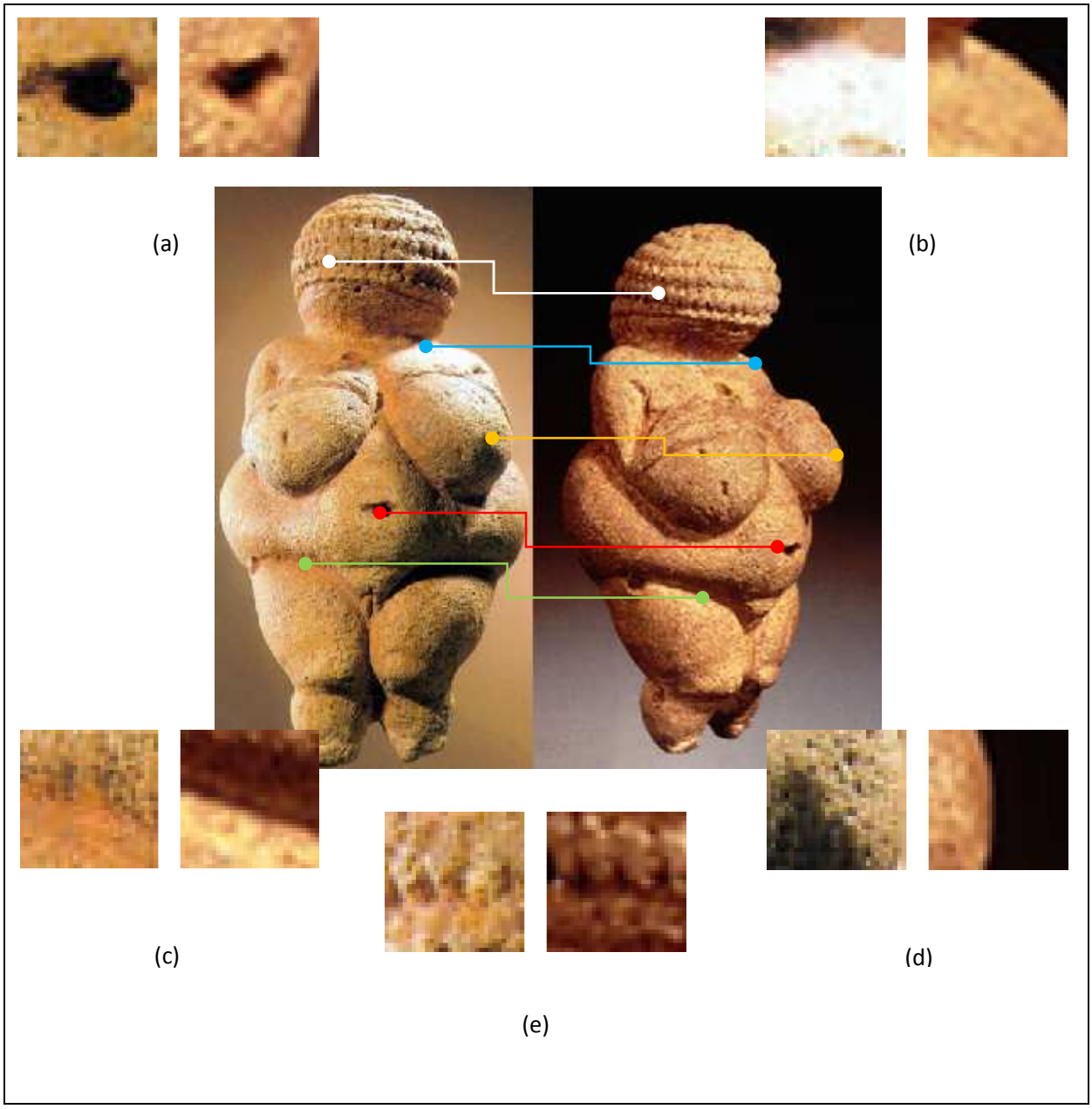

Figure *Example of a stereo-pair of the Willendorf Venus (Natural sciences museum, Vienna). Most of the more common problems in the use of similarity functions are shown: (a) homography effect distort the shape of the features (red), (b) saturation of camera or lack of texture make constant image pixels (blue), (c) shadows and self-shadows generate different features with different illuminations (green), (d) occlusions problem: not all the targets can be seen from two different points of view (yellow), (e) periodical patterns generate ambiguity (white).*

In planetary field, for low value of the ratio baseline/height most of these problems are not present: orbit choice generally does not produce occlusions and all the cameras see the same zone of the target, self shadow are limited to deep craters or cracks, periodical structures are not present, angle of views are limited and the effect is a low prospective distortion between the two images. However, all these anomalies have to be kept in mind to understand the possible mismatching in the estimation of the disparity map.

Algorithms

Approaches to the correspondence problem can be broadly classified in two categories: the *intensity-based matching* and the *feature-based matching* techniques. In the first category, the matching process is applied directly to the intensity profiles of the two images, while in the second, features are first extracted from the images and the matching process is applied to the features.

(a) (b)

Figure *Example of the application of a features extractor on the image (a) representing the intern of Beelitz Hospital, (Berlin). On image (b) it is possible to see all the linear features identified and easily usable for stereo reconstruction in features based algorithms.*

The kind of application in which stereo matching process is engaged will determine of the selection of the approach.

Usually in urban or sub-urban environment, rich of human buildings or structures, the feature-based algorithm is mostly used.

Intensity based matching is generally required every time the aim of the application is the reconstruction of an open surface as in planetary sciences or photogrammetric field.

According to a recent taxonomy [SST01], stereo algorithms that generate dense depth measurements can be roughly divided into two classes, namely *global* and *local* algorithms. Global algorithms, e.g. [KZG01], rely on iterative schemes that carry out disparity evaluation on the basis of the minimization of a global cost function. These algorithms yield accurate and dense disparity measurements, but exhibit a very high computational cost that renders them unsuited to real-time applications. Local algorithms, e.g. [FAU93,KAN85], also based on area-based algorithms, calculate the disparity at each pixel on the basis of the photometric properties of the neighboring pixels.

Compared to global algorithms, local algorithms yield significantly less accurate disparity maps but, nowadays, thanks to both research and technology advances, they can run fast enough to be deployed in many real-time applications.

3.2.2.Segmentation

Since computer graphics has became a valid method for scientific or industrial investigation the possibility to detect or, more often, recognize objects in images has involved a lot of scientists in analyzing and refining methods to define the division of the image in sub-sets limited by topological boundaries.

This process is called segmentation and refers to the process of partitioning a digital image into multiple segments (sets of pixels) (also known as super-pixels). The goal of the segmentation is to simplify and/or to change the representation of an image into something that is more meaningful and easier to analyze. Image segmentation is typically used to locate objects and boundaries (lines, curves, etc.) in images. More precisely, image segmentation is the process of assigning a label to every pixel in an image such that pixels with the same label share certain visual characteristics.

The result of image segmentation is a set of segments that collectively cover the entire image, or a set of contours extracted from the image (process more known as *edge detection*). The pixels in a region are similar with respect to some characteristic or computed property, such as color, intensity, or texture. Adjacent regions are significantly different with respect to the same characteristic(s).

Applications of this method can be found in medical imaging for the diagnostic analysis of meta-images acquired with micro-optical instrumentations or systems in not-visible spectral range. More investigated applications are the location of tumors or other pathologies, the volume measurement, the diagnosis around blood anomalies or the presence of particular anatomical structures in ultrasounds. Even in the industry the method has allowed a good improvement of the chain systems and security controls. In astronautics the segmentation is a valid and now robust tool for the identification of roads, forests or different kind of cultivations for Earth orbits or objects tracking for inflight operations.

Most of the methods include the use of different processes of filtering to achieve a boolean version of the images where the TRUE values indicates region researched and FALSE values identifies the scene background.

Algorithms structures

We can divide the different algorithms, working on the segmentation problem, in some classes.

Cluster methods which partitioning an image into the so call clusters define a set of locations, and analyze the cluster separately.

Histogram method analysis defines the different structures by multidimensional thresholds on the local histograms.

Edge detection is a well-developed method used in image processing. Region boundaries and edges are closely related, since there is often a sharp adjustment in intensity.

The edges identified by this method are often disconnected, however to segment an object from an image closed region boundaries are needed. Thus, the discontinuities are usually bridged if the distance between the two edges is within some predetermined threshold. One such method is the *edge linking method*, proposed by Pathegama and Gol [PA04].

Dual *transformation methods* are more used when a precise model of the shape of the feature to be recognized is proposed. As an example, Atiquzzaman in [ATI92] defined the so called Hough transformation for the detection of circular or elliptical shapes in the image.

Graphs can also be effectively used for image segmentation. Usually a pixel or a group of pixels are vertices and the edges define the (dis)similarity among the neighborhood pixels. Some popular algorithms of this category are random walker, minimum mean cut, minimum spanning tree-based algorithm, normalized cut, etc.

A very interesting method adopted in this work is based on the snakes. We think it is one of the most robust methods used for the segmentation and we will describe it in the next section.

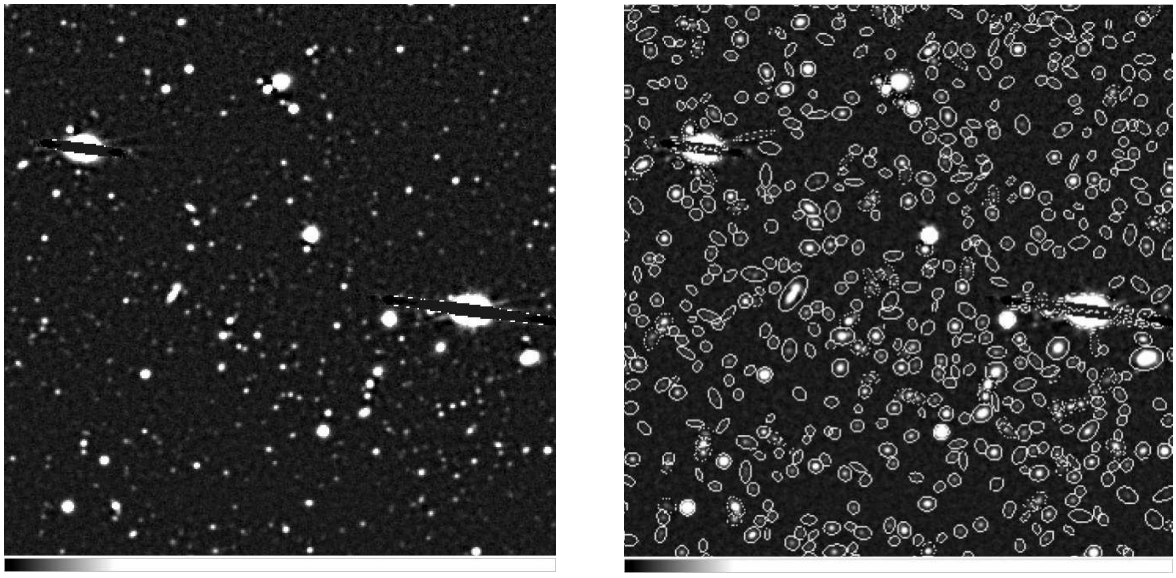

Figure *Segmentation used to identify and catalog sky objects in an image by boundaries detection.*

3.2.3.Snakes

Overview of the basic snake models

A bidimensional *snake* represents a chain of points that can move in a plane maintaining their connections (see Figure). The movement of the snake points is due to applied forces which, on one side, define the continuity and the rigidity of the snake and, on the other side, drive the chain of points to a target border.

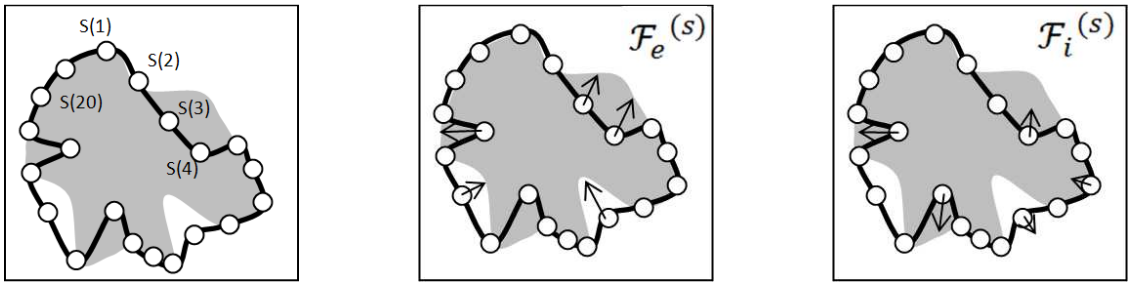

(a) (b) (c)

Figure *Example of a snake used for segmentation. In (a) the snake is defined as a map* $\Omega_{12}\{1,2,\dots,20\} \rightarrow \Re^2$. *In (b) the largest external forces are shown. Their aim is to move the snake components towards the boundary of the shape through the optical flow. In (c) the largest internal forces are shown. Their aim is to move the snake components to avoid peaks and maintain continuity. The composition resulting by the application of the two different forces defines the motion of the snake.*

Normally a *snake* is defined by *N* ordered points and can be parametrically defined as a time variant map $s \in \Omega_{12}: I \rightarrow \Re^2$ given by $s(i) = [u_{1i};\ u_{2i}]$ (the time dependence is not explicitly shown here), where $1 \leq i \leq N$ and $[u_{1i};\ u_{2i}]$ are the two Cartesian coordinates of the i^{th} point of the curve.

To bring the snake contour towards the target border, an iterative process is applied which, at every cycle, evaluates two different snake "energies": the *external energy* $\mathcal{E}_e$, which corresponds to the overall "distance" between the snake and the target border (usually defined as the local *optical flow,* see Horn 1981 as a reference), and the *internal energy* $\mathcal{E}_i$, (used to impose some regularity to the contour shape). The snake is defined as a sequence of points connected by twos to compose a unique line. The external forces move the points to the boundary while the internal one assures that the links

between consecutive points never generate peaks or not-natural features. Then, the total snake energy $\mathcal{E}_{snake}$ can be defined as the sum of these two energies applied to all the points of the snake:

$$\mathcal{E}_{snake} = \sum_i \left[\alpha \mathcal{E}_i\big(s(i)\big) + \beta \mathcal{E}_e(s(i))\right] \qquad ()$$

The parameters α and β define the relative weight of the two energies and have to be set empirically.

It can be easily seen that the optimal snake contour is obtained when $\mathcal{E}_{snake}$ is minimized. To this end, two different types of force acting on the snake points are introduced, each associated to one of the two energies: the external forces $\mathcal{F}_e^{(s)}$ try to move the snake points towards the target boundary, to reduce the external energy $\mathcal{E}_e$; the internal forces $\mathcal{F}_i^{(s)}$, instead, try to avoid possible artifacts in the contour, as narrow spikes, to minimize the internal energy $\mathcal{E}_i$. At each cycle of the iterative process, suitable external and internal forces are applied to the snake in the attempt to minimize the total snake energy. The process continues until the snake stability is achieved.

Another useful definition is the snake velocity $\dot{s}$:

$$\dot{s} = \alpha\ \mathcal{F}_e^{(s)}\ + \beta\ \mathcal{F}_i^{(s)} \qquad ()$$

By this definition the components to add to the snake at every cycle are directly obtained.

Generalization to the multidimensional case

It is also possible to generalize the snake definition to a multidimensional case. In this case, the snake is defined as a time variant map $S \in \Omega_{mn}$: $\Re^m \rightarrow \Re^n$ given by $s(\bar{\imath}) = s(i_1, i_2, \ldots, i_m) = (u_{1\bar{\imath}}, u_{2\bar{\imath}}, \ldots, u_{n\bar{\imath}})$, between the *m* coordinates $i_{\bar{\imath}}$ of the *m*-dimensional snake points and the *n* coordinates u_k of the point. Extending the definition of snake velocity to this multidimensional case, we obtain:

$$\dot{S} = \mu \sin\theta \, \mathcal{F}_e^{(S)} + \mu \cos\theta \, \mathcal{F}_i^{(S)} \qquad ()$$

where $\mathcal{F}_e^{(S)} \in \Omega_{mn}$ represents the external forces, and $\mathcal{F}_i^{(S)} \in \Omega_{mn}$ represents the internal ones. In () the scalar coefficients α and β used in () have been redefined in radial sense by means of the relations $\mu^2 = \alpha^2 + \beta^2$ and $\tan\theta = \frac{\alpha}{\beta}$. In this representation the μ coefficient is related to the evolution rate of the snake and tanθ gives the ratio of the weights of the external forces with respect to the internal ones.

A relatively small value for the μ coefficient provides better stability avoiding problems due to time integration; the coefficient θ has to be set as a function of the smoothing effect we expect on the surface. Generally, if the target multi-dimensional surface has high frequency features, it is convenient to reduce the weight β of the internal forces with respect to the weight α of the external ones, giving rather large values of the angle θ. In the tests described in the following, we have used $70° \leq \theta < 90°$.

Equation () can be brought to a more practical form for implementation in a software code. In fact, in every snake problem the external forces $\mathcal{F}_e^{(S)}$ are defined as the opposite of the gradient along the range coordinates of the external energy $\mathcal{E}_e^{(S)}$. The external energy value depends on the snake position relative to the target border and is normalized in order to be positive everywhere and zero at

the ideal target boundary. Moreover, the internal forces $\mathcal{F}_i^{(S)}$ can be defined as the Laplacian $\Delta^i S$ of the snake in the coordinates of the domain. The application of these forces increases the snake continuity.

Under these assumptions, equation () can be rewritten as:

$$\dot{S} = \mu \left[sin\theta \cdot -\left(\nabla_u \mathcal{E}_e{}^{(S)}\right) + cos\theta \Delta^i S \right] \qquad ()$$

3.2.3. Shape from silhouette

The segmentation is proposed as a good method for recognizing different structures in the same image; even the identification of the simple boundary of a target body with respect to the scene has found an interesting application in qualitative 3D reconstruction.

Considering an object O defined by a close surface *S*(*x*) and a bench of images I_i, representing the object acquired by different points of view all around 360°, it is possible to identify by segmentation the boundaries; then, a the projective process will use this information to generate a convex model of the object.

These were the earliest attempts in reconstruction of 3D models from photos: using the silhouette of objects as source of information on the shape. A 2D *silhouette* is the set of close contours that outline the projection of the object onto the image plane. Segmentation of the silhouette from the rest of the image and combination with multiple silhouettes of the same object, taken from different point of views, provide a strong cue for shape understanding.

This technique is called *shape from silhouettes*. The computed silhouettes for every image along with the centre of the corresponding camera is then used to define a volume which, if projected to 3D space, can be assumed to bound the object. The intersection of these volumes associated with the set of acquired images yields a reasonable approximation of the real object. This intersection volume has been named the *visual hull* by Laurentini et. al. [LAU94] and described as the maximal object that gives the same silhouette with the real object from any possible viewpoint or in other words the convex hull containing the same object.

A property of the visual hull is that increasing the number of images the fit of the object volume becomes tighter. However, this number can be proved [LAU97] to be unbound for reconstruction of general polyhedral objects. Even if the acquisition of an infinite number of images is possible, silhouettes might be insufficient clues for fully compute the shape of not convex objects. An example where the silhouette methodology fails is illustrated in Figure . The reason for this limitation is that concavities in the object geometry result in self occluded areas for the object that cannot be resolved from any point of view unless additional information is provided.

Unfortunately, the type of object is not the only parameter affecting its corresponding visual hull form. The positioning of the cameras can significantly influence the computed model especially when the number of acquisition locations is small.

In this sense, *shape from silhouettes* is a particularly good approach if only a rough model of the real world is required. The methodology is intuitive and easy to implement and this is the main reason that systems generating and replaying 3D digital video as well as commercial object modeling packages [NIE94] are based on it. Nevertheless, reconstruction is restricted to small solid objects for which their whole geometry can be captured from photos around them and it is not applicable to scene modeling.

For a better understanding, let us explain the application of *shape from silhouette*s to multi-imaging acquisition.

We consider the closed surface $S(\bar{p})$ where $\bar{p}$ is any kind of parametrization of a subset of R^2, and a volume $V(x)$ whose values, are 0 if x is external to S and 1 if it is internal.

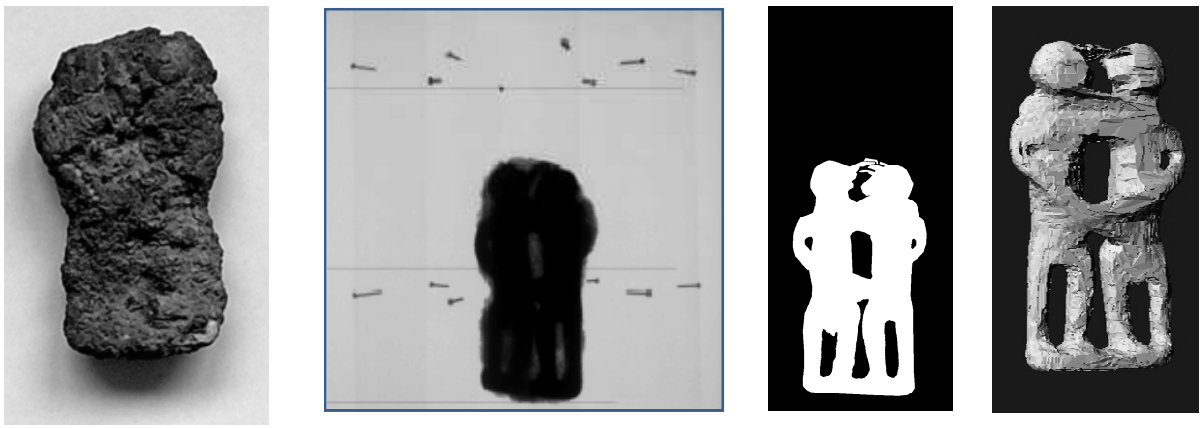

(a) (b) (c) (d)

Figure *Example: first image (a) shows a bronze paleolitic discovered next to Este (TV) in bad oxidation state. X-ray acquisitions were obtained using same nails as reference points (see image b).Knowing the acquisition system parameters a 3D model can be obtained by using the segmented images (an example can be seen in c) as silhouettes for the method. A deeper explanation of the process of reconstruction will be explained in detailed in Chapter 7.*

In any image I_i we can identify an area $\widetilde{S_i} = P_i(S)$ projection of the same surface S in the i[th]-image.

It is clear that considering a point or a volume inside or outside surface $S(p)$, its projection will be found in all the $\widetilde{S_i}$ if the considered structure is inside the surface. On the other side, if an image I_ii exists in which the projection of the structure results outside the associated area $\widetilde{S_i}$, the structure has to be considered inconsistent and removed by initial structure model. So the heuristic is the following:

$$\exists i: P(v) \notin \widetilde{S_i} \rightarrow v \notin V \; and \; V(v) = 0$$

The method consists in eliminating time by time the region not identified as a boundary in the i[th] image.

Most of the algorithms using *shape from silhouettes* have spread their efforts in finding a correct, robust method to reach a greedy division of the volume Vin its subsets v. In these cases the algorithm can be written as

```
Define V

For any  v_k ∈ V following the heuristic

      If    P(v) ∉ S̃_i

      then  V = V ∩ v_k

endif

end_heuristic
```

In absence of high resolution, a carpet analysis can be used dividing the considered space V in uniform subset as a 3D grid. All the points of the grid can be projected on all the images and a check about its consistency can be done.

After having defined all the values of the functional $V(x)$, the surface S has its best approximation in the iso-curve $S_0 = x$: $\lim_{x^* \to x} V(x^*) = 1^-$.

The *shape from silhouettes* has the limit, shown in Figure , that even a large number of images can be acquired around a subset without being able to extract the concavities in the final reconstruction model. *Shape from silhouettes* remains blind to the concavity of the target measuring system so we can consider the remaining parts after the heuristic as a representation of the convex model of the target.

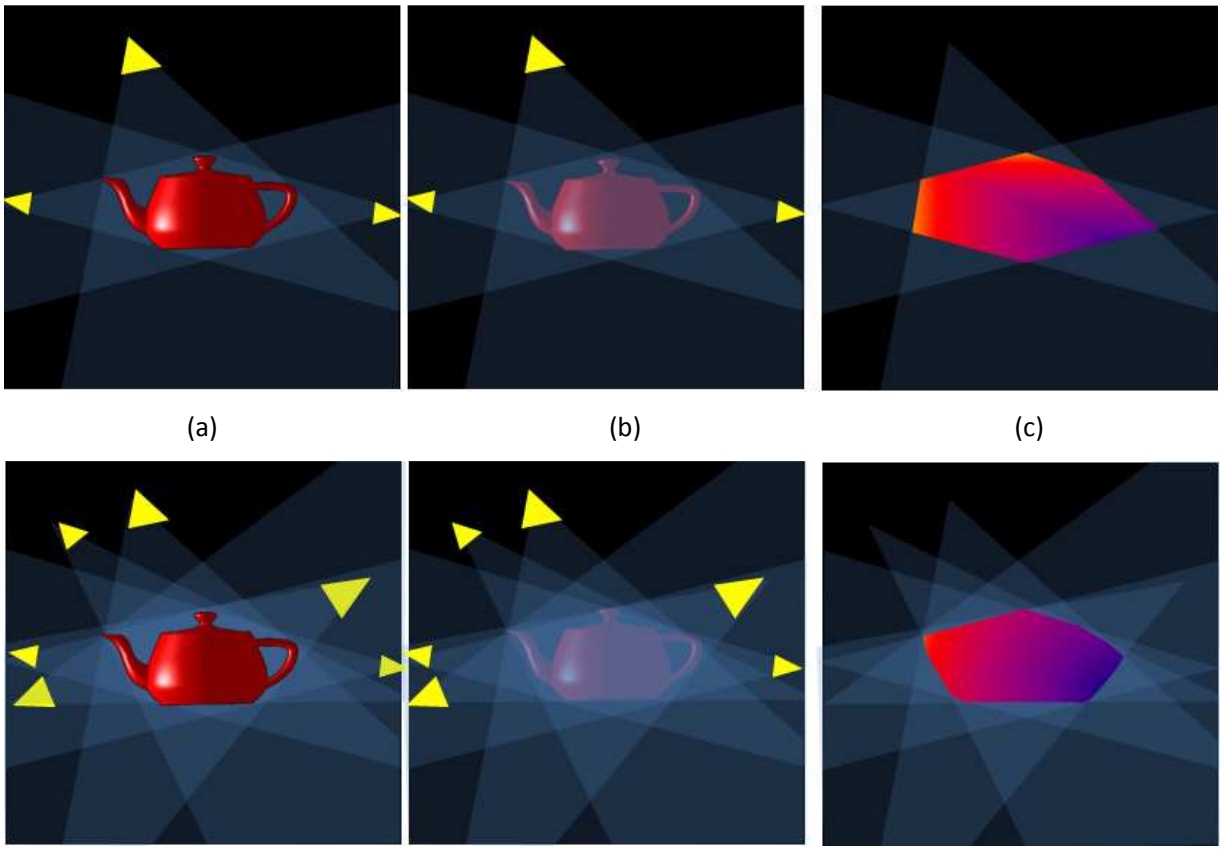

(a) (b) (c)

(d) (e) (f)

Figure *Example. The teapot is acquired by 3 different point of views in images a,b,c. Image (a) shows the target, image b underlines the point of view and the region described by the acquisition system. Image c the final result. Same operation can be done using more point of views (images d e f). The higher numbers of point of views get more precise the result (image f compared to image c) but it is still evident that convex parts are not shown.*

3.2.4.Shape from shading

Shape from shading is the process of computing the three-dimensional shape of a surface from an image of that surface using as *information* the local relationship between the reflectance of the surface and its first order approximation. Contrary to most of the other three-dimensional reconstruction models (for example, stereo and photometric stereo), in *shape from shading* the needed data are minimal: a single image! As a consequence, this inverse problem is intrinsically difficult. In this chapter we describe the main difficulties of the problem and the approximation we can use in the case of planetary surface images.

The *shape from shading* technique computes the three-dimensional shape of a surface from the brightness of one grayscale image (see Figure).

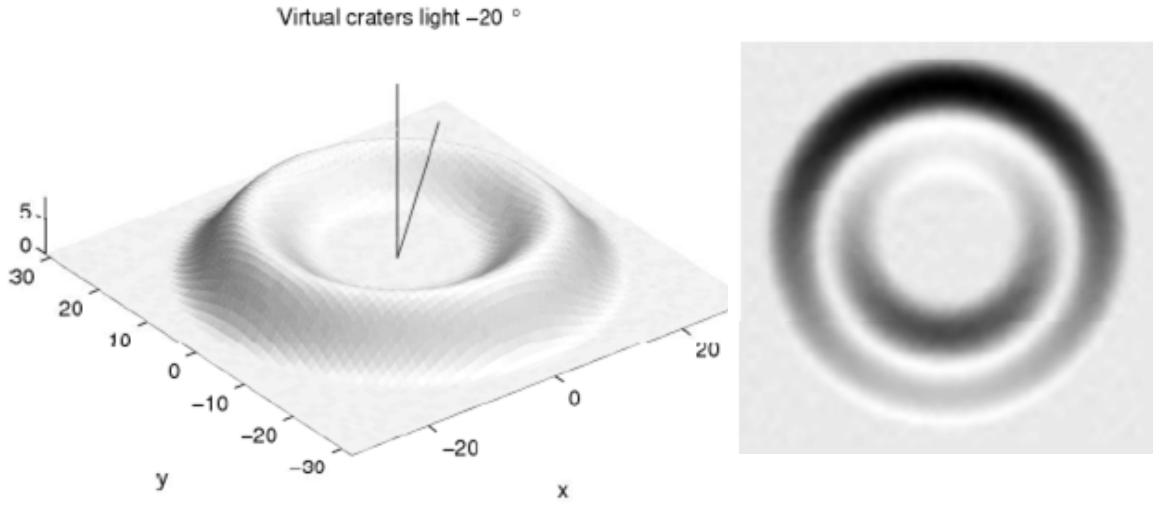

Figure *Example of the result of the light effect for a virtually lambertian crater. On the left the 3D model is shown. The vertical line represents nadir direction, while the tilted one indicates the Sun illumination direction. On the right the image resulting from a nadir observer, obtained with rendering, is shown.*

In the 70's, Horn [HOR75] was the first to formulate the *shape from shading* problem, simply and rigorously, as that of finding the solution of a nonlinear first-order Partial Differential Equation (PDE) called the brightness equation. In a first period (in the 80's), a lot of effort was put in the computational part of the problem, trying to calculate directly numerical solutions. Questions about the existence and uniqueness of solutions of the problem were simply never posed at that time, with the important

exception of the work of Bruss [BRU85] and Brooks [BRO83]. Nevertheless, due to the poor quality of the results, these questions as well as those related to the convergence of numerical schemes for computing the solutions became central in the last decade of the 20th century. Today, the *shape from shading* problem is known to be an ill-posed problem.

Figure *From the image we perceive two craters, a small and a big one. But we can turn these craters into volcanoes (although upside down) if we imagine the light source to be at the bottom of the picture rather than at the top. This picture is actually that of a pair of ash cones in the Hawaiian Island.*

Several papers show that the solution is not unique [OLI91/PRA02]. The encountered difficulties have often been illustrated by such concave/convex ambiguities as the one displayed in Figure . In this figure, the ambiguity is due to a change of the estimation of the parameters of the illumination. In fact, this kind of ambiguity can be widely generalized. In [BEL99], Belhumeur and colleagues proved that when the direction of the illumination and the Lambertian[11] reflectance (albedo[12]) of the surface are unknown, then the same image can be obtained by a continuous family of surfaces (depending linearly of three parameters). In other words, they show that neither shading nor shadowing of an object, seen from a

[11] If a surface exhibits Lambertian reflectance, light falling on it is scattered such that the apparent brightness of the surface to an observer is the same regardless of the observer's angle of view. More technically, the surface luminance is isotropic

[12] The albedo of an object is the extent to which it diffusely reflects light from the sun. It is therefore a more specific form of the term reflectivity. Albedo is defined as the ratio of diffusely reflected to incident electromagnetic radiation. It is a unitless value indicative of a surface's or body's diffuse reflectivity. The word is derived from Latin albedo "whiteness", in turn from albus "white". The range of possible values is from 0 (dark) to 1 (bright).

single point of view reveals its exact 3D structure. This is the *bas-relief ambiguity*, see [BEL99]. Being aware of these difficulties, we therefore assume here that all the parameters of the light source, the surface reflectance and the camera are known.

Formulation

As we have mentioned above, the modeling of the *shape from shading* problem introduced by Horn leads to a PDE: the brightness equation. This equation arises from the following hypothesis: we define an orthonormal system XYZ centered on the surface, with the Z axis in the same direction of the acquisition system , and where the plane XY is parallel to the image plane.

We can define the image as the brightness function that maps every point $\bar{u} \in H \times W$ (image domain) to the reflectance map of the 3D point $\boldsymbol{x} \in \mathcal{R}^3$, projective source of the point $\bar{u}$. This function depends on the shape and the albedo of the surface and on the illumination at the time of acquisition.

If we assume the surface as Lambertian we can write:

$$\begin{cases} I(\bar{u}) = L(\boldsymbol{x}) \\ L(\boldsymbol{x}) = \rho(\boldsymbol{x})\hat{s}(\boldsymbol{x})^T\hat{n}(\boldsymbol{x}) \end{cases} \quad ()$$

where ρ id the *effective albedo* , $\hat{s}$ is the versor of the direction of the light on $\boldsymbol{x}$ and $\hat{n}$ is the normal to the surface on the same point $\boldsymbol{x}$.

In astronautic field, working with planetary surfaces, the light source is assumed as a point at infinity and we lose in this manner the dependence of the vector $\hat{s}(\boldsymbol{x})^T$ from the point considered. Moreover, taking into account a little section of the image we can also consider the albedo as constant. This brings to write:

$$L(\boldsymbol{x}) = \rho\hat{s}^T\hat{n}(\boldsymbol{x}) = R(\hat{n}(\boldsymbol{x})) \quad ()$$

where R represents the reflectivity of the surface in one point as a function of its normal vector.

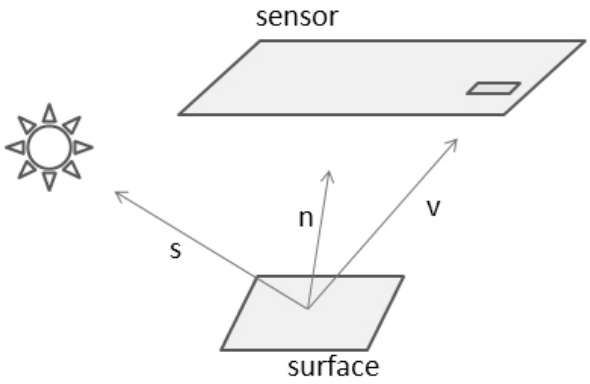

Figure *Convention on the direction of the vectors: s from the target surface to the light source, n the normal to the surface and v the projection vector from the surface to the pixel sensor.*

Equation () is the *brightness equation* or brightness vinculum. It expresses the injectivity[13] between the gray-scale value in a point of the image and the direction of the vector normal to the surface in the same point.

In this way, all the points where the surface has the same normal vector (remember the hypothesis on the reference frame) will impress the sensor with the same digital value.

Unfortunately, the problem is locally under-vincolated. From the *brightness equation* we can obtain the angle between $\hat{n}$ and $\hat{s}$, but this then forces $\hat{n}$ to stay on a cone of directions around $\hat{s}$. Multiple images can be used to supply other information and to add new vincula to the system.

All these considerations were done always assuming a orthographic acquisition system. In projective systems, equation () has to be rewritten taking in account the variability of v (*the projection vector from the surface to the pixel sensor*) with respect to the pixel considered.

Anyway, as we have seen in section , if we consider a small part of the image we can assume the projective system as orthographic[14] and we obtain $\boldsymbol{x} = [\bar{u}, \mathcal{S}(\bar{u})]^T$.

Finally, another additional vinculum can be considered for planetary surface: the *integrability vinculum* coming from the continuity of the surface.

[13] In mathematics, an injective function is a function that preserves distinctness: it never maps distinct elements of its domain to the same element of its codomain. In other words, every element of the function's codomain is mapped to by at most one element of its domain.

[14] We can consider the projection lines as parallel and so the projective system as orthographic. In this case we can simplify the formulation of the problem and we do not consider the scalar factor between the image and the surface, imposing the ratio between focal length and mean-distance equal to 1.

We can define the gradient of the surface as $[p, q]^T$ where:

$$\begin{cases} p = \dfrac{d\mathcal{S}}{du_1} \\ p = \dfrac{d\mathcal{S}}{du_2} \end{cases} \quad ()$$

From equation () we obtain a new model for the normal vector:

$$\hat{\boldsymbol{n}} = \frac{[-\boldsymbol{q}, -\boldsymbol{p}, \mathbf{1}]}{\sqrt{1 + p^2 + q^2}} \quad ()$$

Equation () can became more explicit introducing the angular form of the normal vector:

$$\hat{\boldsymbol{n}} = \begin{bmatrix} \mathbf{cos\,\alpha\,sin\,\beta} \\ \mathbf{sin\,\alpha\,sin\,\beta} \\ \mathbf{cos\,\beta} \end{bmatrix}^{\mathbf{T}} \quad ($$

where α and β represent respectively the *tilt-angle*[15] and the *slant-angle*[16] (see Figure for better understanding).

[15] *The tilt-angle, also called azimuth, is the angle between the X axis and the projection of the vector on the XZ plane.*

[16] *The slant-angle is created by the vector with Z axis in radial sense.*

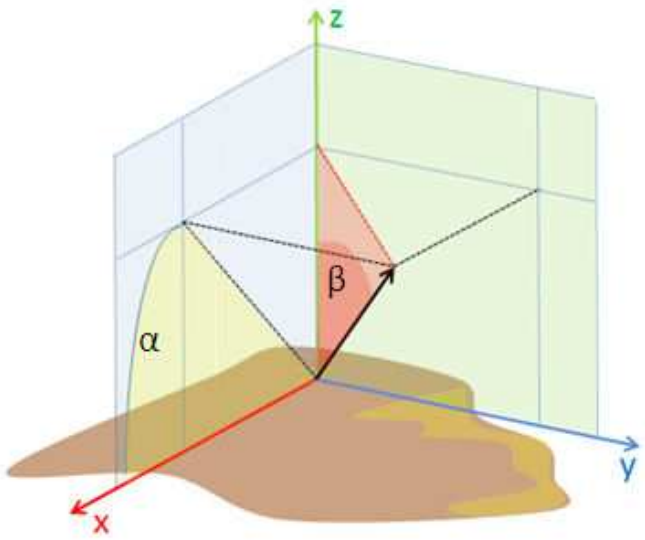

Figure *The image shows in details the slant and tilt assumptions. In green is identified the Z axes and the plane YZ, in blue the Y axis and the plane XZ. In red the X axis.*

The yellow sector represents the tilt α. In red, the plane between the vector and the Z axis and the slant angle β on that plane *are identified.*

The same model can be used to characterize the light-vector $\hat{s}$ by its *tilt* τ and its *slant* σ.

$$R(p,q) = \frac{-p\ cos\tau\ sin\sigma\ \ - q\ sin\tau\ sin\sigma\ + cos\sigma}{\sqrt{1} + p^2 + q^2}$$

$$\Updownarrow \qquad ()$$

$$R(\alpha,\beta) = \rho\ (cos\tau\ sin\sigma\ cos\alpha\ sin\beta + sin\tau\ sin\sigma\ sin\alpha\ sin\beta\ + cos\beta\ cos\sigma\ ).$$

Figure shows the iso-lines of the reflectivity-map $R_{p,q}$ for the nadir direction where the *tilt* τ is $\simeq 45^{\circ}$ and the *slant* σ is $\simeq 10^{\circ}$.

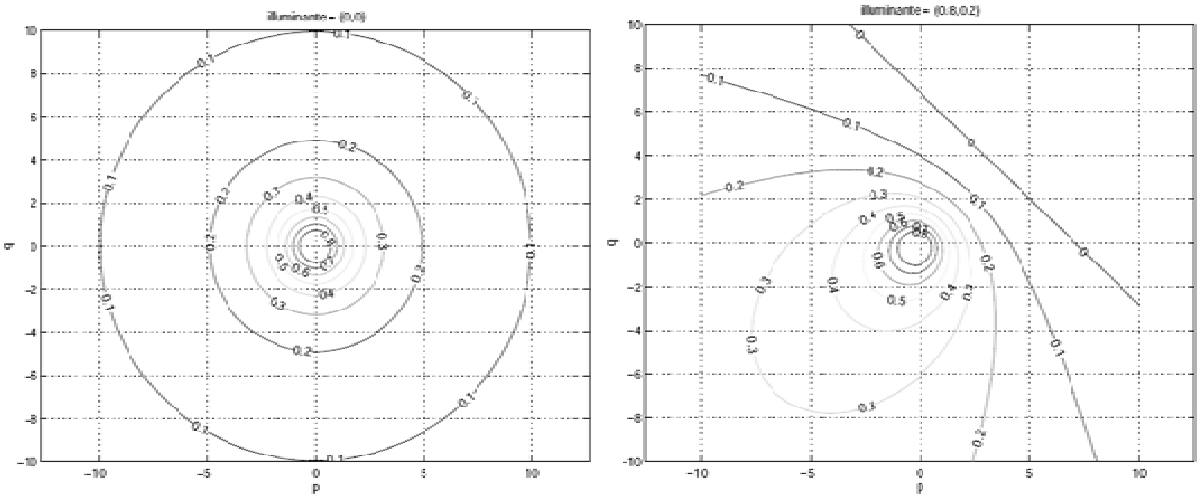

(a) (b)

Figure *Iso-lines of the reflectivity map for two different values of the light-direction.*

Alghorithm overviews

Some different approaches to the problems are shown in following paragraphs.

Horn and Ikeuchi

One of the first approaches to the SFS is due to Horn and Ikeuchi. They recognized that the problem was not clearly stated, and they tried to apply a regularization method that consisted in adding a regularization term (smoothness constraint) to the brightness vinculum penalizing the not regular (or excessively detailed) solutions.

However, the solution obtained with this algorithm is not really satisfactory; in addition, to apply it, it is necessary to know a priori the surface gradient on the boundaries, and this is information is not always available.

Tsai and Shah

The idea of Tsai and Shah [TSA94] is rather different. They rewrote the fundamental equation of SFS () as $\mathrm{I}_{\{\mathrm{x,y}\}} - \mathrm{R}_{\{\mathrm{p,q}\}} = 0$ and then they replaced the terms p and q with the local approximation in the discrete domain:

$$\begin{cases} p = \mathrm{Z}_{\{x,y\}} - \mathrm{Z}_{\{x-1,y\}} \\ q = \mathrm{Z}_{\{x,y\}} - \mathrm{Z}_{\{x,y-1\}} \end{cases}$$

obtaining:

$$\begin{gathered} \mathrm{I}_{\{x,y\}} - \mathrm{R}\_\{\mathrm{Z}_{\{x,y\}} - \mathrm{Z}_{\{x-1,y\}}, \mathrm{Z}_{\{x,y\}} - \mathrm{Z}_{\{x,y-1\}}\} = 0 \\ \Updownarrow \\ \mathcal{F}(\mathrm{I}_{\{x,y\}}, \mathrm{Z}_{\{x,y\}}, \mathrm{Z}_{\{x-1,y\}}, \mathrm{Z}_{\{x,y-1\}}) = 0 \end{gathered} \qquad ()$$

The method is very important in the context of this work for two reason: it solves the problem by the minimization of a unique positive function $\mathcal{F}$ (usable as we will see in Chapter 5 in snake context as Energy) and differently by other methods it is applicable to every reflectance map even if it is not Lambertian.

Zheng and Chellappa

This is the simplest algorithm for the extraction of the albedo value from the images used for solving the SFS system.

The used approximation is relative to the distribution of the vectors normal to the surface. They impose that this distribution is radial[17]. In Figure we show some examples of normal distributions. The gray color represents how much the normal vector to a point of the surface is close to the direction of the normal vector of a reference sphere.

[17] In this approximation, the prevailing direction is the nadir one and the distribution of the normal vectors does not depend by their tilt.

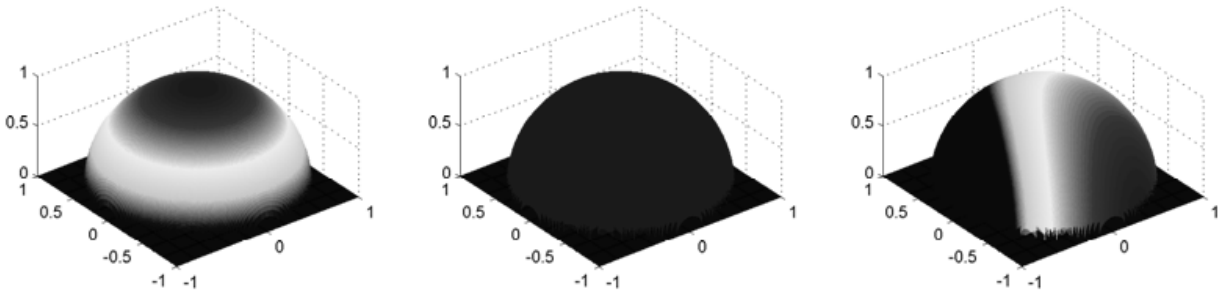

(a) (b) (c)

Figure *Normal vectors statistical distribution for (a) radial assumption, (b) uniform assumption and (c) not-radial assumption.*

It is useful to define here the mean and the variance[18] of the image:

$$E[I] = \int d\alpha \int_0^{\frac{\pi}{2}} d\beta \, \wp(\alpha,\beta) I_{\alpha,\beta}$$

()

$$E[I^2] = \int d\alpha \int_0^{\frac{\pi}{2}} d\beta \, \wp(\alpha,\beta) I_{\alpha,\beta}^2$$

where $\wp(\alpha,\beta)$ is the statistical distribution of the intensity of the image and $I_{\alpha,\beta}$ the same image as functions of the angles.

Equations () can be rewritten as:

$$\begin{cases} E[I] = \int d\alpha \, \wp(\beta) \int_0^{\frac{\pi}{2}} d\beta \, I_{\alpha,\beta} \\ E[I^2] = \int d\alpha \, \wp(\beta) \int_0^{\frac{\pi}{2}} d\beta \, I_{\alpha,\beta}^2 \end{cases} \quad ()$$

[18] Mean and Variance are here considered as the expectation values of the image, considered as a random variable.

From the *brightness vinculum* () and the angular form of the reflectivity map, we obtain by integration:

$$E[I] = 2\,\pi\,\rho\,\cos\sigma \int_0^{\frac{\pi}{2}} \cos\beta\, \wp(\beta)\, d\beta$$

$$E[I] = \frac{\rho^{\,2}}{2}\,\sin^2\sigma\, + \pi\,\rho^2\,(3\cos^2\sigma - 1) \int_0^{\frac{\pi}{2}} \cos^2\beta\, \wp(\beta)\, d\beta$$

Schedule	Summary of the albedo calculation in the radial hypothesis

3.2. Concept integrations

In this section we give a formulation of the *Shape from Shading* and the Stereo method.

We consider again the *brightness vinculum* () and we try to infer other properties of the image. Following[19] Schedule

$$I_1(\bar{x}) = P_1(\mathcal{S}, \mathbb{C}, \boldsymbol{s})$$

$$I_2(\bar{y}) = P_2(\mathcal{S}, \mathbb{C}, \boldsymbol{s})$$

$$I_1(\bar{x}) \simeq I_2(\bar{y}) \quad \text{where} \quad \bar{y} = \mathfrak{D}(\bar{x})$$

Then we try to achieve a linear solution of the *brightness vinculum* by adding limiting less constraining hypothesis.

Hypothesis I *We assume the local albedo constant $\rho = k$. Or we assume locally uniform the reflective structure of the surface considered as a target.*

Under this first hypothesis, previous equations can be reduced to:

$$I_1(\bar{x}) = P_1(\mathcal{S}, \boldsymbol{s})$$

$$I_2(\bar{y}) = P_2(\mathcal{S}, \boldsymbol{s})$$

$$I_1(\bar{x}) \simeq I_2(\bar{y}) \quad \text{where} \quad \bar{y} = \mathfrak{D}(\bar{x})$$

Hypothesis II *We assume the transformation as locally orthographic. This makes linear the transformation between 3D world and images.*

As shown in equation ():

$$\overline{J_1} = \frac{K_{2\times3}R_1}{q_{1_{(\boldsymbol{x_m})}}}(\boldsymbol{x} - \boldsymbol{c_1})$$

$$\overline{J_2} = \frac{K_{2\times3}R_2}{q_{2_{(\boldsymbol{x_m})}}}(\boldsymbol{x} - \boldsymbol{c_2})$$

[19] We identify (see Notations) with the straight accent the bidimensional vectors and with bold case the tridimensional ones.

We can now consider the relative disparity $\mathfrak{D}$ representing the map $\Omega_{22}: \mathrm{N}^2 \to \mathrm{U} \times \mathrm{V}$ between the coordinates $\bar{x}$ of the first image and the relative coordinates $\bar{y}$.

Hypothesis III *The image is rectified. We analyze the case in which the information is only on one of the two coordinates of the disparity;*
In this case $\mathfrak{D} = \{\mathfrak{D}_x, \mathfrak{D}_y\}$ *can be represented by one of its component. So we consider* $\mathfrak{D}(i_1, i_2) = \mathfrak{D}(\bar{x}) = \mathfrak{D}_x$ *as a* $\Omega_{21}: N^2 \to U$ *between the coordinates* $\bar{x}$ *of the first image and one component of the relative coordinates* $(\bar{y} - \bar{x})$.

Under this condition we can assume the transformation between the surface coordinate and the disparity difference as linear at local level:

$$\exists \mathscr{L}: \mathfrak{D}_{\bar{\imath}} = \mathscr{L}(\mathcal{S})$$

where we consider the surface $\mathcal{S}$ as the map $\Omega^{\Re}_{\Re^2}$ which associates to all the pairs of ground coordinates (x,y) the elevation $z = \mathcal{S}(x, y)$ of the corresponding point.

Hypothesis IV *The image orientation is next to terrain reference frame. We can substitute* $\nabla_{\bar{x}}$ *with* $\nabla_{\bar{\imath}}$ *if we assume* $\nabla_{\bar{\imath}} x$ *and* $\nabla_{\bar{\imath}} y$ *as locally constant.*

Calculating the gradient of $\mathfrak{D}$ we obtain other two linear transformations:

$$\begin{cases} \exists \mathscr{L}_i: & \dfrac{\partial \mathfrak{D}_{i_1,i_2}}{\partial i_1} = \mathscr{L}_{i_1}\left(\dfrac{\partial \mathcal{S}_{x,y}}{\partial x}\right) \\ \exists \mathscr{L}_j: & \dfrac{\partial \mathfrak{D}_{i_1,i_2}}{\partial i_2} = \mathscr{L}_{i_2}\left(\dfrac{\partial \mathcal{S}_{x,y}}{\partial y}\right) \end{cases} \qquad ()$$

In a more compact notation, we can write equations () following our notations:

$$\begin{cases} \exists \mathscr{L}: & \mathfrak{D}_{\bar{\imath}} = \mathscr{L}(\bar{x}, \mathcal{S}_{\bar{x}}) \\ \exists \widehat{\mathscr{L}}: & \nabla_{\bar{\imath}} \mathfrak{D}_{\bar{\imath}} = \widehat{\mathscr{L}}(\nabla_{\bar{x}} \mathcal{S}_{\bar{x}}) \end{cases} \qquad ()$$

We remember that the versor normal to the surface can be written as

$$n'(\boldsymbol{x}) = \begin{bmatrix} -\nabla_{\bar{x}} & \mathcal{S}_{\bar{x}} \\ 1 & \end{bmatrix} \rightarrow \hat{n} = \frac{\hat{n}'(\boldsymbol{x})}{\|\hat{n}'(\boldsymbol{x})\|} \qquad ()$$

As we have seen in () we can even transform this vector $n'(\boldsymbol{x})$ as a function of the disparity, and the result will be:

$$n(\boldsymbol{x}) = \frac{\begin{bmatrix} -\widehat{\mathscr{L}^{-1}}(\nabla_{\bar{\imath}}\mathfrak{D}_{\bar{\imath}}) \\ 1 \end{bmatrix}}{\sqrt{1 + \widehat{\mathscr{L}^{-1}}(\nabla_{\bar{\imath}}\mathfrak{D}_{\bar{\imath}})^2}} \qquad ()$$

Now we can write the *brightness vinculum* as a function of the disparity values:

$$\mathrm{I}_{\bar{\imath}} = \rho\, \hat{\boldsymbol{s}}^{\boldsymbol{T}}\, \hat{n}(\boldsymbol{x}) = \rho \hat{\boldsymbol{s}}^{\boldsymbol{T}} \frac{\begin{bmatrix} -\widehat{\mathscr{L}^{-1}}(\nabla_{\bar{\imath}}\mathfrak{D}_{\bar{\imath}}) \\ 1 \end{bmatrix}}{\sqrt{1 + \widehat{\mathscr{L}^{-1}}(\nabla_{\bar{\imath}}\mathfrak{D}_{\bar{\imath}})^2}} \qquad ()$$

or:

$$\mathrm{I}_{\bar{\imath}} = \rho \frac{\cos(\beta_s) - \widehat{\bar{s}^T \mathscr{L}^{-1}}(\nabla_{\bar{\imath}}\mathfrak{D}_{\bar{\imath}})}{\sqrt{1 + \widehat{\mathscr{L}^{-1}}(\nabla_{\bar{\imath}}\mathfrak{D}_{\bar{\imath}})^2}} \qquad ()$$

where we divided $\hat{s}^T$ in its first two components and the third one, $\hat{s}^T = [\bar{s}^T | s_3]$, and we used the definition of the slant angle for a versor $s_3 = \cos(\beta_s)$.

Raising to the second power, we obtain:

$$\left(1 + \widehat{\mathscr{L}}^{-1}(\nabla_{\bar{\imath}}\mathfrak{D}_{\bar{\imath}})^2\right) \mathrm{I}_{\bar{\imath}}^2 = \rho^2 \left(\cos(\beta_s) - \bar{s}^T \widehat{\mathscr{L}}^{-1}(\nabla_{\bar{\imath}}\mathfrak{D}_{\bar{\imath}})\right)^2 \quad ()$$

The attempt is to simplify equation () to reach a model close to:

$$I_{\bar{\imath}} = \mathcal{L}_f(\nabla_{\bar{\imath}}\mathfrak{D}_{\bar{\imath}}) \rightarrow \nabla_{\bar{\imath}} I_{\bar{\imath}} = \mathcal{L}_f\left(\Delta^{\bar{\imath}}\,\mathfrak{D}_{\bar{\imath}}\right) \quad ()$$

where the final linear transformation $\mathcal{L}_\mathrm{f}$ summarizes all the other transformations. In so doing, we were able to identify the relationship between the Laplacian of the disparity and the gradient of the image.
We can try to understand the meaning of equation () using an image. In Figure two different parts, red and blue squares, are selected. If we analyze the red area it is evident that it has no intensity variance along the vertical lines. All the light-information is compressed along the horizontal line. It is easy verify that the $\frac{\partial I_i}{\partial i_1} \gg \frac{\partial I_i}{\partial i_2}$ where i_1 is the horizontal coordinate. In this direction in fact we can assume the surface as constant. In the blue area both the derivatives are not zero and so even the d_i varies in both directions.

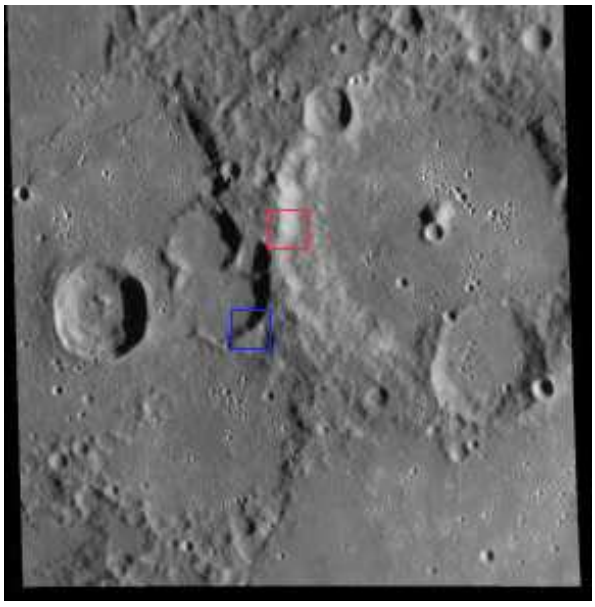

Figure *Image obtained with the NAC instrument on board the MESSENGER mission, during the first flyby with Mercury. The red square identifies an horizontal slope for the intensity of the image, while the blue square represents the vertical one*

These are not conclusive equations for the scope of the work want to reach. The present attempt is to find an easy model for the definition of an "energy"[20] to be associated to *shape from shading*. Different models were taken in account and new ones are actually in review. The contribution of different people in photo-clinometry could give new solution for a usable model.

[20] The meaning of "energy" will be better explained in the following of the thesis: now we can simply say that this concept is at the basis of the new algorithm we have developed for realizing 3D reconstruction starting with a couple of stereo images.

References

[HAY21] Ibn al-Haytham **Book of Optics** *Book,*Cairo,Egypt,1021

[WIL93] R.Willson and S. Shafer **A Perspective Projection Camera Model for Zoom Lenses** *Proceedings Second Conference on Optical 3-D Measurement Techniques*, Zurich Switzerland, October 1993.

[KHA07] Khaleghi, B. et al **Performace Evaluation of Similarity Metrics for Stereo Corresponce Problem** *Electrical and Computer Engineering, 2007. CCECE 2007. Canadian Conference on Volume , Issue , 22-26 April 2007 Page(s):1476 - 1478*

[KAN94] Takeo Kanade and Masatoshi Okutomi **A stereo Matching Algorithm with Adaptive Window: Theory and experiments** *IEEE Transaction on pattern analysys and machine intelligence VOL 16, NO. 9, September 1994*

[SST01] D.Scharstein and R. Szeliski.**A taxonomy and evaluation of dense two-frame stereo correspondence algorithms** *Microsoft Research Technical Report* MSR-TR-2001-81, 2001.

[KZG01] V.Kolmogorov and R. Zabih.**Computing visual correspondence with occlusions using graph cuts.** *In Proceedings of International Conference on Computer Vision*, 2001.

[FAU93] O. Faugeras et al.**Real-time correlation-based stereo: algorithm, implementation and applications** *INRIA Technical Report n. 2013, 1993.*

[KAN95] T. Kanade et al **Development of a video-rate stereo machine.** *In Proc. Of International Robotics and Systems Conference (IROS '95), volume 3, pages 95 – 100, August 1995.*

[PA04] M. P. Pathegama and Ö. Göl**, An Artificial Neural Process to Create Continuous Object Boundaries in Medical Image Analysis, International** *Scientific Journal of Computing, vol. 3, Issue 1, 2004.*

[ATI92] Atizuzzaman M. **Multiresolution Hough transform- an efficient method of detecting patterns inimages,** *IEEE Transactions Pattern Analysis Machine Intelligence 14,1090-1090*

[LAU94] A. Laurentini. **The visual hull concept for silhouettes -based image understanding.** *IEEE Transactions on pattern analysis and machine intelligence*, 16(2):150-162, 1994.

[LAU97] A. Laurentini. **How many 2d silhouettes does it take to reconstruct a 3d object?** *Computer Vision and Image Understanding*, 67(1):81-87, 1997.

[HOR75] B. Horn**. Obtaining shape from shading information***. In P. Winston,editor, The Psychology of Computer Vision. McGraw-Hill, New York, 1975.*

[BRU85] A. Bruss. **The eikonal equation: Some results applicable to computer vision**. *Journal of Mathematical Physics, 23(5):890–896, 1982.*

[BRO83] M. Brooks. **Two results concerning ambiguity in shape from shading.***In AAAI-83, pages 36–39, 1983.*

[OLI91] J. Oliensis**. Shape from shading as a partially well–constrained problem***. CVGIP: Image Understanding, 54(2):163–183, 1991.*

[OLI91] J. Oliensis. **Uniqueness in shape from shading. IJCV**, *2(6):75–104,1991.*

[ROU92] E. Rouy and A. Tourin. **A Viscosity Solutions Approach to Shapefrom-Shading**. *SIAM J. of Numerical Analysis, 29(3):867–884, 1992.*

[BEL99] P. N. Belhumeur, D. J. Kriegman, and A. L. Yuille**. The bas-relief ambiguity***. IJCV, 35(1):33–44, 1999.*

[DUR00] J.-D. Durou and D. Piau**. Ambiguous shape from shading with critical points***. JMIV, 12(2):99–108, 2000.*

[PRA02]E. Prados, O. Faugeras, and E. Rouy**. Shape from shading and viscosity solutions***. In ECCV'02, volume 2351, pages 790–804, 2002.*

[PRA03] E. Prados and O. Faugeras. **"Perspective Shape from Shading" and viscosity solutions.** *In ICCV'03, volume 2, pages 826–831, 2003.*

[HON91] K. Ikeuchi and K.S. Hong: **"Determining Linear Shape Change: Toward Automatic Generation of Object Recognition Programs"**, *Computer Vision, Graphics, and Image Processing: Image Understanding, Vol.53, No.2, pp.154-170, March 1991.*

[THO98] Thomas et al. (1998). "**OSIRIS-the optical, spectroscopic and infrared remote imaging system for the Rosetta Orbiter**". *Advances in Space Research* **21**: 1505–1515.

[TSA94] Tsai, M. Shah, **Shape from shading using linear approximation***, Image Vision. Computer. 12 (8) (1994) 487–498*

Chapter 4

BepiColombo Mission

Contents

Introduction

This Chapter will give a brief explanation of the context in which the new method is introduced.

The following sections will explain the mission BepiColombo to Mercury and the STC instrument design.

4.1 BepiColombo mission

4.1.1. Overview

BepiColombo[1] is the fifth cornerstone mission of the European Space Agency (ESA) foreseen to be launched in August 2014 with the aim of studying in great detail Mercury, the innermost planet of the Solar System.

Mercury is very important from the point of view of testing and constraining the dynamical and compositional theories of planetary system formation. In fact, being in close proximity to the Sun, in its history it has been subjected to the most extreme environmental conditions, such as high temperature and large diurnal variation, rotational state changes due to Sun induced tidal deformation, surface alteration during the cooling phase, and chemical surface composition modification by bombardment in early history.

As we will see in the conclusion of this chapter the extreme characteristic of the planet and the ambition of the mission are the reasons which have brought to the decision to apply a new method for the tridimensional reconstruction of its surface.

Mercury has been studied by the **Mariner 10** spacecraft (S/C) in 1974-75 [DEV78] –[SLA97], when less than half of the planetary surface has been imaged at low resolution (scale factor of about 1-2 km/px) and its magnetic field and exosphere was discovered (see Figure 1). Since then, the only other satellite reaching Mercury is the **NASA Messenger**, that has very recently realized three flybys with the planet [SOL08]; Messenger will be inserted in orbit around Mercury in March 2011.

The BepiColombo payload, especially designed to fully characterize the planet, will consist of two modules: the **Mercury Planet Orbiter (MPO)**, realized in Europe, carrying remote sensing and radio science experiments, and the **Mercury Magnetospheric Orbiter (MMO)** [HAY04] ,realized by JAXA[2] in Japan, carrying field and particle science instrumentation. These two complementary packages will allow to map the entire surface of the planet, to study the geological evolution of the body and its inner structure, i.e. the main MPO tasks, and to study the magnetosphere and its relation with the surface, the exosphere and the interplanetary medium, i.e. MMO targets. Instruments on board of both the modules are presented in Table 1,Table 2.

[1] BepiColombo is named after Professor Giuseppe (Bepi) Colombo (1920-1984) from the University of Padua, Italy, a mathematician and engineer of astonishing imagination. He was the first to see that an unsuspected resonance is responsible for Mercury's habit of rotating on its axis three times for every two revolutions it makes around the Sun. He also suggested to NASA how to use a gravity-assist swing-by of Venus to place the Mariner 10 spacecraft in a solar orbit that allowed it to flyby Mercury three times in 70'.

[2] Japanese Aerospace Exploration Agency.

	Name	Aim and objectives	PIs
BELA	BepiColombo Laser Altimeter	*Topography and surface morphology. Digital terrain model expected will impart information about the internal structure, the geology, the tectonics, and the age of the planet's surface.*	***N. Thomas**, University of Bern,CH, **T. Spohn**, DLR, DE*
MERMAG MAG	The Mercury Magnetometer	*Planetary magnetic field and its source. With attention to origin, evolution and current state of the planetary interior, and interaction between magnetosphere and solar wind.*	***K.H. Glassmeier**, Technical University of Braunschweig, DE*
MERTIS	Mercury Thermal Infrared Spectrometer	*Mineralogical composition, crucial for understanding evolution of the planet.*	***H. Hiesinger**, University Münster,DE*
MGNS	Mercury Gamma ray and Neutron Spectrometer	*Elemental composition of the surface and subsurface,with attention to polar areas, permanently shadowed from the Sun.*	***I.Mitrofanov**, Institute for Space Research, RU*
MIXS	Mercury Imaging X ray Spectrometer	*Global map of the surface atomic composition at high spatial resolution*	***G. Fraser**, University of Leicester, UK*
MORE	Mercury Orbiter Radio Science Experiment	*Gravity field of Mercury, as well as the size and physical state of its core and test theories of gravity with unprecedented accuracy.*	***L. Iess**, University of Rome "La Sapienza", IT*
ISA	Italian Spring Accelerometer	*Supporting MORE experiment, Mercury's interior structure and test Einstein's theory of the General Relativity.*	***V. Iafolla**, CNR-IFSI, IT*
PHEBUS	Probing of Hermean Exosphere by Ultraviolet Spectroscopy	*Mercury's exosphere and research of ice hidden deposits on the surface.*	***E. Chassefière,** Université P&MCurie, FR*
SERENA	Search for Exosphere Refilling and Emitted Neutral Abundances	*Gaseous interaction between surface, exosphere, magnetosphere and solar wind.*	***S. Orsini,** CNR-IFSI, IT*
SYMBIO-SYS	Spectrometers and Imagers for MPO BepiColombo Integrated Observatory System	*Surface geology, volcanism, global tectonics, surface age and composition, and geophysics.*	***E. Flamini,** ASI, IT*
SIXS	Solar Intensity X ray Spectrometer	*Measurements of X rays and particles of solar origin at high time resolution and a very wide field of view .*	***J. Huovelin**, Observatory University of Helsinki, FI*

Table 1 *List of the MPO experiments*

	Name	Aim and objectives	PIs
MERMAG MGF	Mercury Magnetometer	*Detailed description of magnetosphere and of its interaction with the planetary magnetic field and the solar wind*	**W.Baumjohann**, Austrian Academy of Sciences, AT
MPPE	Mercury Plasma Particle Experiment	*Characterization of the magnetosphere particles*	**Y. Saito**, ISAS, JAXA, JP
PWI	Mercury Plasma Wave Instrument	*Analysis of the structure and dynamics of the magnetosphere*	**H. Matsumoto**, RISH, Kyoto Univ., JP
MSASI	Mercury Sodium Atmospheric Spectral Imager	*Sodium measurement in Mercury's exosphere*	**I. Yoshikawa**, Univ. Tokyo, JP
MDM	Mercury Dust Monitor	*Interplanetary dust in the orbit of Mercury*	**K.Nogami,** Dokkyo Med. Univ., JP

Table 2 *List of the MMO experiments*

The MPO orbital characteristics, i.e. elliptical polar orbit with periherm and apoherm altitudes of 400 km and 1500 km respectively, and 2.3 hours orbital period, are mainly determined by the need for the remote sensing instruments to have high spatial resolution not changing too much all over the surface during the one year nominal mission lifetime, and are extremely challenging due to the thermal constraints on the S/C. For a continuous observation of the planet surface during the mission, the S/C is 3-axis stabilized with the Z-axis, corresponding to payload bore-sight direction, pointing to nadir.

4.1.2.Simbiosys

The MPO module is carrying instruments which are devoted to the close range study of the Mercury surface, to the investigation of the planet gravity field and to realize fundamental science and magnetometry measurements. Imaging and spectral analysis are performed in the IR, visible and UV range. These optical observations are complemented by those of gamma-ray, X-ray and neutron spectrometers, which yield additional data about the elemental composition of the surface, and by those of a laser altimeter, BELA [THO07], dedicated to high accuracy measurements of the surface figure, morphology and topography.

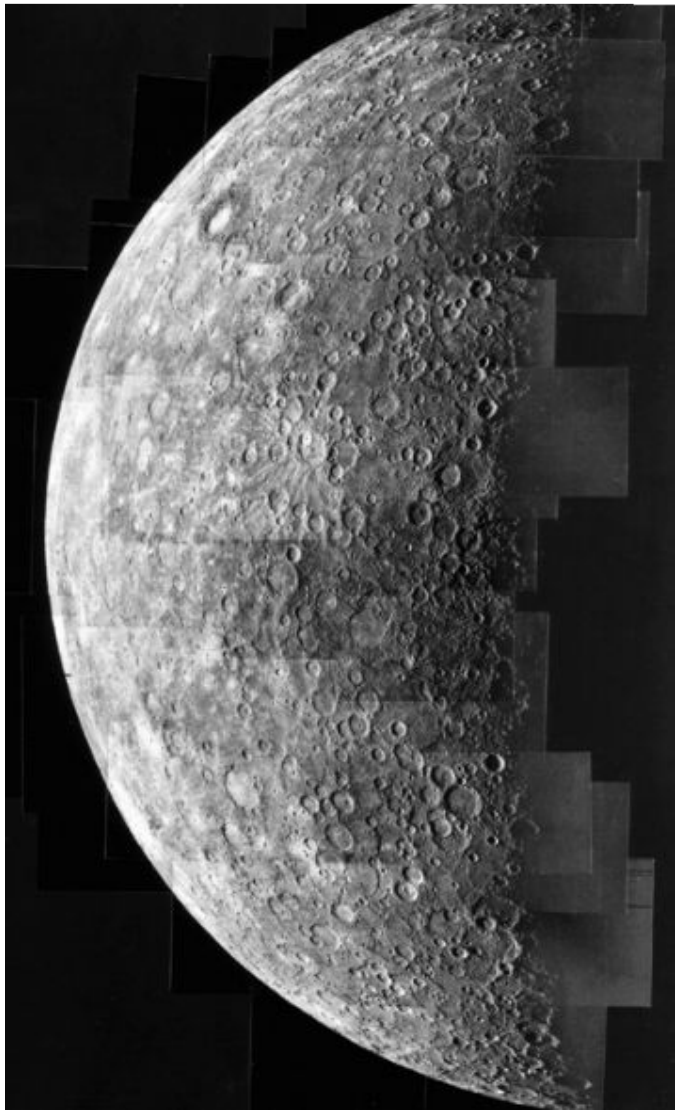

Figure 1 *Hermitian surface acquired at the hands of Mariner10 in 1974*

The imaging and spectroscopic capability of the MPO modulus will be exploited by the Spectrometers and Imagers for **MPO BepiColombo Integrated Observatory SYStem (SIMBIOSYS)**, an integrated system for imaging and spectroscopic investigation of the Mercury surface [FLA10]. A highly integrated concept is adopted to maximize the scientific return while minimizing resources requirements, primarily mass and power.

SIMBIO-SYS incorporates capabilities to perform 50-200 m spatial resolution global mapping in both stereo mode and color imaging, high spatial resolution imaging (5 m/px scale factor at periherm) in panchromatic and broad-band filters, and imaging spectroscopy in the 400-2200 nm spectral range. This global performance is reached using three independent channels: the **Stereoscopic imaging Channel, STC** [DEP10]; the High

Resolution Imaging Channel, HRIC [DEP10]; and the Visible and near-Infrared Hyperspectral Imager, VIHI [CAP05] (see Figure 2).

4.2. STC Stereo Channel

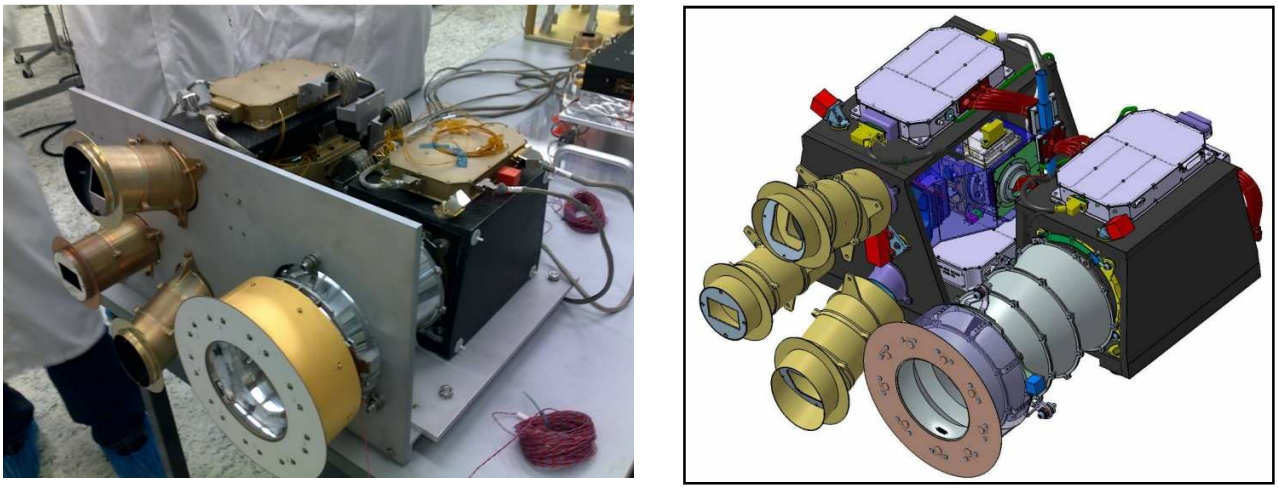

(a) (b)

Figure 2 *(a) The structural and thermal model of the SIMBIOSYS instrument at the Selex Galileo premises before its delivery to ESA. (b) Structural scheme of the SIMBIOSYS instrument suite; from left to right: VIHI, STC (with two apertures), and HRIC*

The optical design of STC and its theoretical performance are presented in next sections; the optical design of STC has been considered frozen in October 2009. The structural and thermal model (STM) (see Figure 2) is now experiencing environmental tests and has been delivered to ESA in September 2010. The Flight Model (FM) is presently being built and is going to be tested in Selex Galileo (Campi Bisenzio, Italy) during next year. The actual schedule foresees that it will be delivered to ESA in January 2012.

In 2011 Selex Galileo will calibrate independently the two channels of STC; in the meanwhile, the science team will perform at the Padova CNR IFN LUXOR laboratories a preliminary test to validate the stereo performance of a breadboard model having the same characteristics of STC. Hopefully, the test will be successful, and in such case the setup will be brought to Selex Galileo premises to characterize the stereo performance of the STC flight model.

The calibration of STC is complicated by the fact that the adopted catadioptric design is really original, optimally aberration balanced and able to satisfy all the scientific and technical requirements imposed by that

particular space mission. So, to be able to actually measure its performance, the test setup, the so-called Optical Ground Support Equipment (OGSE), has to have a also better quality, putting stringent constraints on the quality of the optical tools.

4.2.1. Optical Design

STC is a double wide angle camera designed to image each portion of the Mercury surface from two different perspectives, providing panchromatic stereo image pairs required for reconstructing the Digital Terrain Model (DTM) of the planet surface. In addition, it has the capability of imaging some portion of the planet in four different spectral bands (see Figure 3)

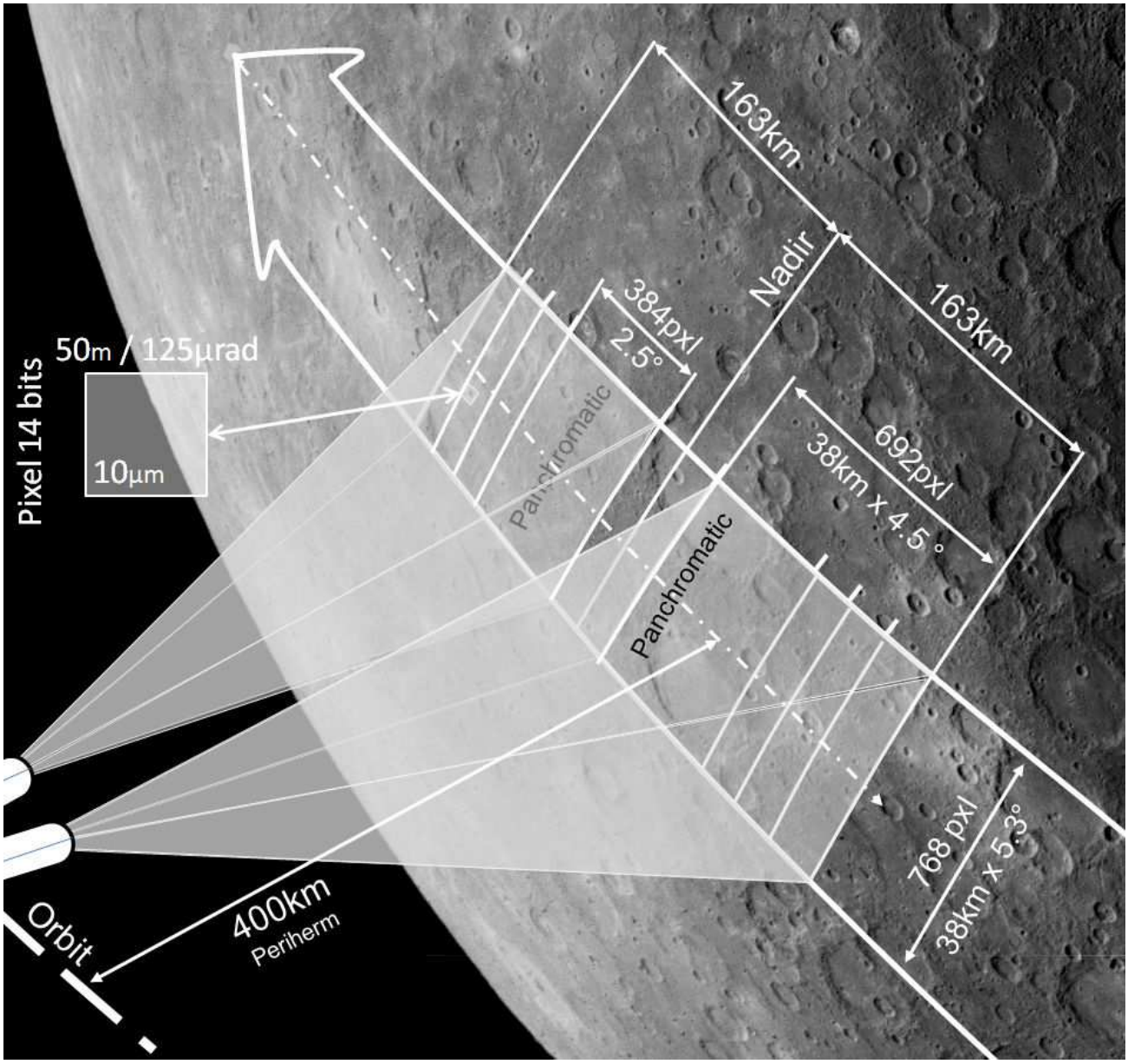

Figure 3 *Scheme of the acquisition system of STC stereo channel. In the image the two symmetrical channels are shown on the bottom left; on the Mercury surface there are the collected image projections, with the division of the acquisition field of view in the different filters*

This is not the first use of a stereo camera on a satellite: **Mar Express**[3] was the precursor with High Resolution Stereo Camera (HRSC). However, the characteristics of STC are greatly different: in particular, the available mass is much smaller (the whole SIMBIOSYS, with three optical heads, weighs about 11.5 kg, that is half the weight of HRSC), and many technological innovations had to be considered to have an instrument adaptable to the Mercury hostile environment**.** These and other constraints, brought to the choice for STC of the push-frame technique instead of the more common push-broom normally utilized even on the terrestrial remote sensing satellites, to grant more reliability on data acquisitions. Moreover, on STC there is a single focal plane assembly for both stereo channels, while very often a stereo system consists of two identical cameras, each with its own detector.

Figure 4 shows different solutions of the satellite photogrammetric approach indicating even some examples of experiments using the different configurations.

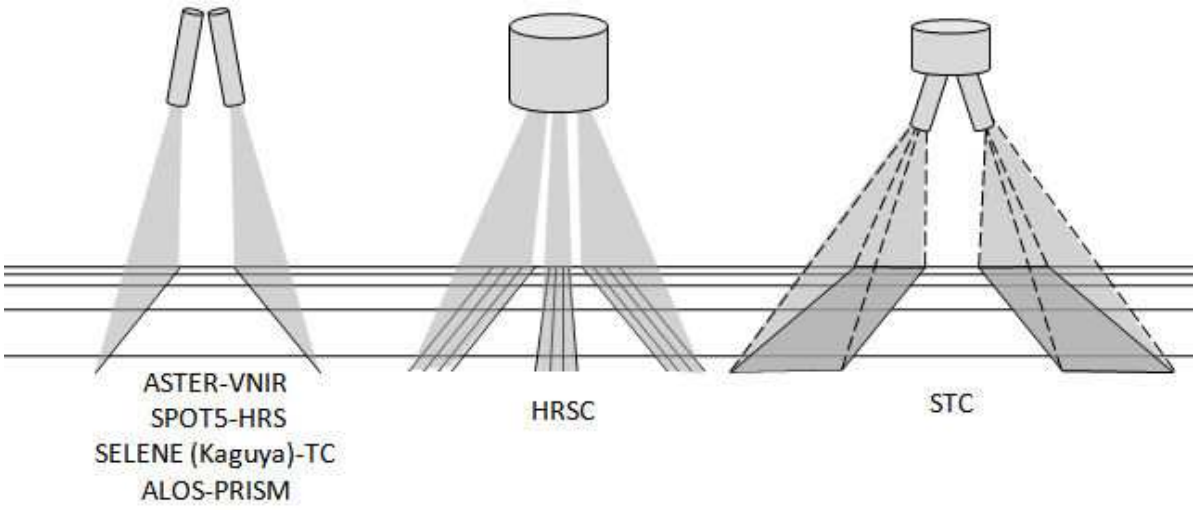

Figure 4 *Possible stereo imaging configurations (see [OBE03]). (a) Generic stereo imaging configuration based on two independent cameras oriented along two slanted viewing directions.*
In (b), there is a single camera with large FoV simultaneously covering both stereo angles and also the nadir-looking direction, if needed. In (c), the stereo configuration proposed for STC, in which most of the optical elements and the detector are common to both sub-channels, is represented. Not drawn to scale.

[3] Mars Express is a space exploration mission being conducted by the European Space Agency (ESA). The Mars Express mission is exploring the planet Mars. "Express" originally referred to the speed and efficiency with which the spacecraft was designed and built. However "Express" also describes the spacecraft's relatively short interplanetary voyage, a result of being launched when the orbits of Earth and Mars brought them closer than they had been in about 60,000 years.

In the BepiColombo Payload Study Document it was suggested to have two cameras, one at low and the other at high resolution, and to use them to perform stereo imaging assuming they have the same FOV. Unfortunately this condition could not be easily realized, mainly if HRIC spatial resolution requirement of 5 m/pixel had to be satisfied. Moreover, since the two cameras had to have substantially different optical designs, many problems were going to be introduced by the camera inter-calibration, which is a necessary requirement for performing stereo reconstruction. So at the end, it was preferred adopt the solution of having a moderate spatial resolution Stereo Camera, that is a camera system which could provide both moderate/low resolution imaging and stereo performance.

Different optical designs of the STC camera, better described in the following, and showing how the camera evolved during the study phase, is shown in Figure 5. In Figure 6 there is a description of the camera Field of View, where it is shown how the different filters cover different angular portions.

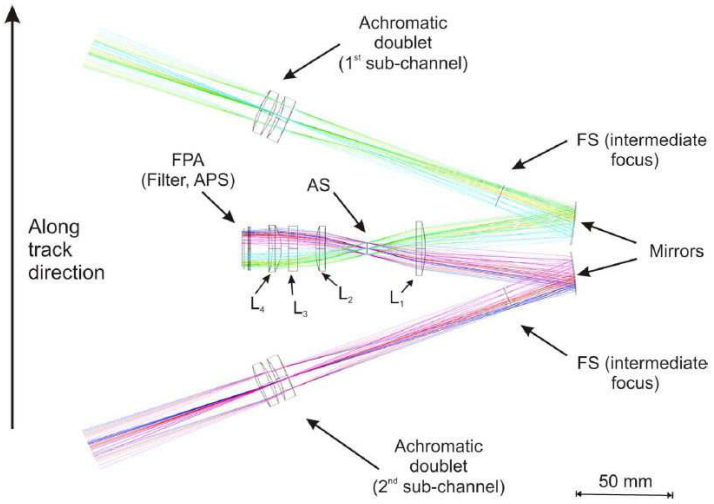

(a)

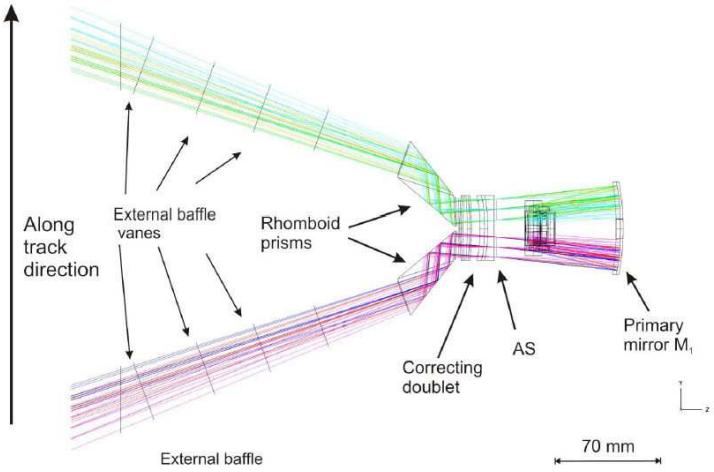

(b)

Figure 5 *Different designs of STC during the project evolution. In (a) Stereoscopic Imaging Channel initial optical design, with a common aperture stop. A one-mirror system and the sensor bore-sight in opposition to nadir direction. In (b) the second design very similar to the final one, with a Rhomboid prism approach as beam deviating optical element .*

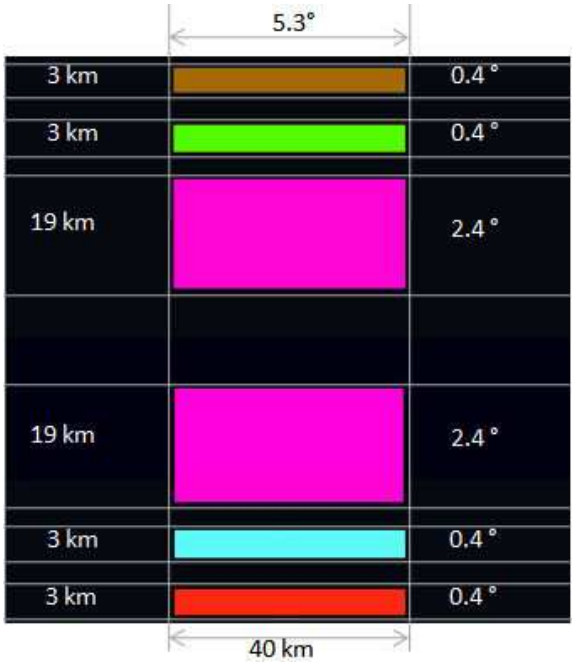

Figure 6 *Position and size of useful filter strips images on the detector area. On the left side of the figure the corresponding size on Mercury surface at peri-herm are indicated for each filter*

4.2.2.STC Stereo Design Concept

The STC final design is composed of two "sub-channels" looking at the desired stereo angles, that share the majority of the optical elements and the detector (see Figure 7, Figure 8). With respect to more classical two- or single-camera designs, this solution allows to reach good stereo performance with general compactness, saving of mass, volume and power resources.

In general, in the space missions in which the satellite has a polar orbit around the observed planet, stereo cameras adopt a push-broom acquisition mode: the detector is a linear array and the full bidimensional image is reconstructed placing side by side each of the lines successively acquired at a suitable rate determined by the spacecraft velocity. For STC, instead, a push-frame mode has been chosen: in this case the detector is a CMOS **Active Pixel Sensor (APS)**[4] bidimensional array, so actual 2D images of the planet surface are acquired, then buffered and read while the spacecraft moves. Only when the image on the detector has shifted along track by an amount almost corresponding to the FoV of each filter, another image is acquired.

The selected APS device has the snapshot option, that is substantially an electronic shutter; for this reason, no mechanical shutter has been foreseen for this instrument. The push-frame acquisition method allows to have some overlap of the imaged regions in the along-track direction, increasing the image matching accuracy and taking into account possible small drifts of the satellite pointing.

[4] An active-pixel sensor (APS), also commonly written active pixel sensor, is an image sensor consisting of an integrated circuit containing an array of pixel sensors, each pixel containing a photo-detector and an active amplifier. There are many types of active pixel sensors including the CMOS APS used most commonly in cell phone cameras, web cameras and in some DSLRs. Such an image sensor is produced by a CMOS process (and is hence also known as a CMOS sensor), and has emerged as an alternative to charge-coupled device (CCD) imager sensors. The term active pixel sensor is also used to refer to the individual pixel sensor itself, as opposed to the image sensor; in that case the image sensor is sometimes called an active pixel sensor imager, active-pixel image sensor, or active-pixel-sensor (APS) imager.

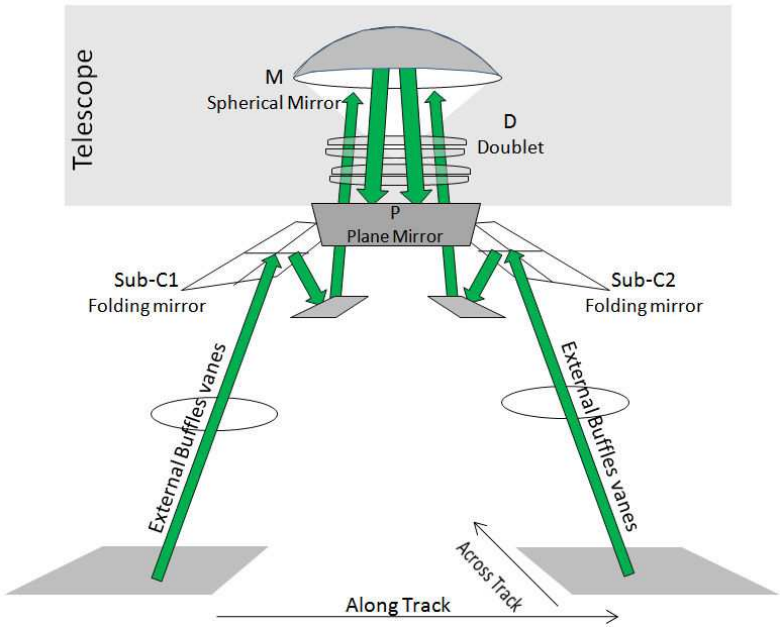

Figure 7 *Schematic of the first part of the final STC optical layout. Only the portion of the optical path from the entrance apertures (bottom of the figure) to the spherical principal mirror M is shown. Optical paths are represented in green, passive side of the mirrors in dark gray and white for the active part*

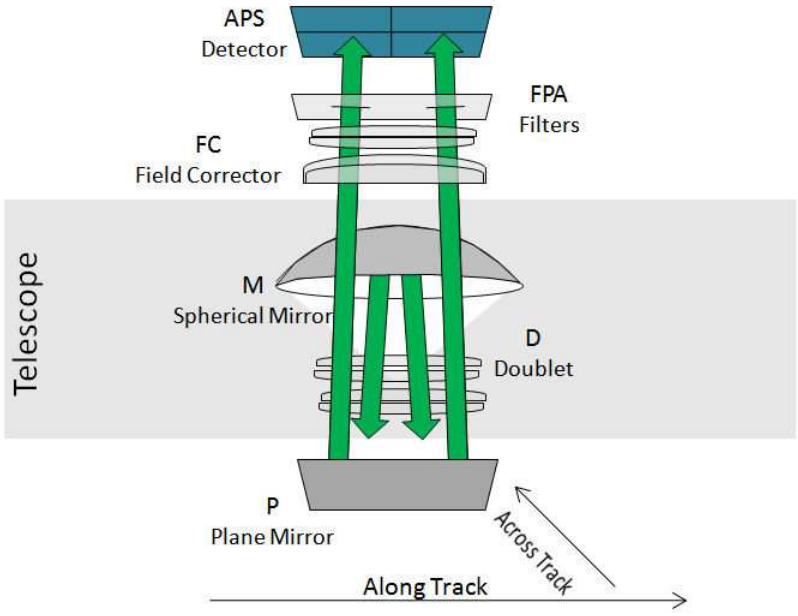

Figure 8 *Schematic of the second part of the STC optical layout. The portion of the optical path from the spherical principal mirror M to the APS detector is shown. Optical paths are represented in green, the detector in blue, passive side of the mirrors in dark gray and white for the active part.*

Optical layout

The first proposed optical design for the stereo camera dated back to 2002; since then the configuration has changed many times to adapt to the evolution of the scientific and technical requirements [DEP10],[CRE04],[DAD08]. The philosophy followed in the design definition has been that of having a compact layout in which the images of the two sub-channels were formed on the same detector.

The STC optical solution (see Figure 7,Figure 8) chosen to be flown on the Bepi-Colombo mission is an original design, which can be thought to be composed by two independent elements: a fore-optics, consisting of two folding mirrors Sub-C1 and Sub C2, one per each channel, and a common telescope unit, which is an off-axis portion of a modified Schmidt design.

The scientific requirements and characteristics of the design are summarized respectively in Table 3 and Table 4. The main characteristics of the optical system can be described following the optical path shown in Figure 7 and Figure 8. First, the couple of folding mirrors Sub-C1/2 redirects the ±20° (with respect to nadir) incoming beam chief rays to a much smaller angle ±3.75°, ones.

Then, a doublet (D), with an essentially null optical power, corrects the residual aberrations of the primary mirror. It has been positioned about half distance between the spherical mirror M and its center of curvature, replacing the classical Schmidt correcting plate (placed in the curvature center), and thus reducing the length by about a factor two with respect to the classical solution. Given that the doublet optical power is near to zero, the residual chromatic aberration in terms of primary and secondary colors is negligible over the whole 410-930 nm spectral range.

Scientific requirements

Ground pixel	scale 50 m/px @400 km (periherm)
Swath	40 km @ 400 km (periherm)
Stereoscopic properties	±21.4° stereo angle withrespect to nadir; both images on the same detector
Vertical Accuracy	80 m
Ensquared Energy MTF	> 70% inside 1 pixel > 60% at Nyquist frequency
Wavelength coverage	410-930 nm
Filters	panchromatic (700± 100 nm)
	420 ± 10 nm
	550 ± 10 nm
	750 ± 10 nm
	920 ± 10 nm

Table 3 *Scientific requirements for the STC-stereo channel of Symbiosis.*

Optical characteristics

Optical concept		Catadrioptic: modified Schmidt telescope plus folding mirrors foreoptics
Stereo solution (concept)		2 identical optical channels; detector and most of the optical elements common to both channels
Focal length (on axis)		95 mm
Pupil size (diameter)		15 mm
Focal ratio		f/6.3
Mean image scale		21.7”/px (105 µrad/px)
FoV	cross-track along-track	5.3° 2.4° (panchromatic) 0.4° (color-filters)
Detector		Si_PIN (format: 2048x2048; 10 µm squared pixel) 14 bits dynamic range

Table 4 *Optical characteristics of STC-stereo channel.*

The aperture stop position, placed in the front focal plane of the M mirror, just after the correcting doublet, has been chosen to allow a good balancing of the aberrations over all the FoV and to guarantee the tele-centricity of the design for preventing wavelength shift at the filter strip assembly (FSA). The telescope mirror is off-axis because of the need to have a free back focal length sufficient to easily integrate the Focal Plane Assembly (FPA), maintaining at the same time the required optical performance. To cope with the field dependent aberrations (i.e. field curvature, lateral color, ..), a two-lens field corrector has been placed in front of the detector. Finally, to reduce the volume of the instrument, the beam exiting M has been folded by a plane mirror P (see the inset of Figure 7,Figure 8) and, for easiness of mounting, the FSA and the detector surfaces are lying in planes parallel to the one including the along track direction and nadir one.

The FSA is mounted just over the detector surface at about 1 mm from it. The FSA is composed by 5 different glass pieces, each with the desired transmission band characteristics, glued together side by side. This solution has the advantage of avoiding the use of cumbersome movable part as a filter wheel; but despite its compactness, it has the drawback that the portions of the filter strips close to the glued edges cannot be used and have to be masked. This masking is anyway useful to cope with the ghosts, both internal and narcissus, which are created by the reflection of the beam inside the filter strip or by multiple reflections on the detector and filter surfaces.

In conclusion, not all the possible FoV is actually recorded, since portions of the incoming beam are blocked and gaps are present between each filtered useful images on the detector (see Figure 6). Thus for each sub-channel, it is possible to acquire simultaneously three quasi-contiguous areas of Mercury surface in different colors and without using movable elements; however, while the nominal FoV of each sub-channel is 5.3° × 4.8°, including gaps, the scientific useful FoV is actually smaller, i.e. 5.3° × 3.2°, and it is divided in three portions (5.3° × 2.4°, 5.3° × 0.4°, 5.3° × 0.4°). At peri-herm, each panchromatic strip corresponds to an area of about 40 × 19 km^2 on the Mercury surface and each colored strip to an area of about 40 × 3 km^2.

Considering that the two sub-channels are projecting their images side by side on the same plane, the useful area on the system focal plane has a rectangular shape, which would obviously be optimally coupled with a rectangular sensor array. However, due to programmatic reasons, a squared 2048 × 2048 pixel array had to be adopted, so that large part of the detector will not be used. In Figure 6 the filter strip image positions on the 2k × 2k detector are schematically represented. The selected detector is a hybrid APS Si_PIN device: this type of detector has been preferred to the more classical CCD because of its radiation hardness, a very critical point given the hostile Mercury environment. Moreover, as already mentioned, its capability of snapshot image acquisition allows both to avoid the use of a mechanical shutter, and to easily obtain the millisecond exposure

times that are necessary to avoid possible image smearing due to the relative motion of the S/C with respect to Mercury surface.

The optical paths of the two sub-channels are well separated; to avoid any interference between the beams, each sub-channel has its own aperture stop, thus obtaining a system with two independent side by side cameras with common optical elements. This solution has the advantage of avoiding the need for an intermediate focus for crosstalk prevention: in fact the stray-light level can be optimally controlled through an ad hoc external baffling system and, since the two sub-channels are kept well apart, by inserting internal separating vanes.

Optical performance

Simulation and camera design optimization have been done by means of **Zemax**[5] ray-tracing software, trying to satisfy the desired optical performance for all the filters over each corresponding FoV and taking care to better optimize the optical performance in the panchromatic band. In addition to having a single detector common to the two sub-channels, the main drivers of the design have been the use of spherical optics only, for easiness of realization, and of using fused silica only as rad-hard glass, for easiness of procurement.

Notwithstanding these extremely critical constraints, an optical configuration which allows to satisfy all the optical requirements has been obtained.

The mean diffraction ensquared energy (EE) has been calculated over all the FoV of each filter, and over the wavelength bands of the filters themselves. The EE including diffraction effects is of the order of 80% all over the FoV of each filter, with the exception of the filter centered at 420 nm where it is just below 80% because of some chromatic focal shift. As an example of the quality of the STC optical performance, the spot diagrams for the panchromatic filter are depicted in Figure 9. It can be seen that the spots are well within the overlaid box having the 10 µm square size of the foreseen detector pixel; a small lateral color residual is present in one corner of the field, but it has been verified to be less than a tolerable value of one third of a pixel.

[5] Zemax is a widely-used optical design program sold by Zemax Development Corporation of Bellevue, Washington (formerly Focus Software). It is used for the design and analysis of optical systems. Zemax can perform standard sequential ray tracing through optical elements, non-sequential ray tracing for analysis of stray light, and physical optics beam propagation.

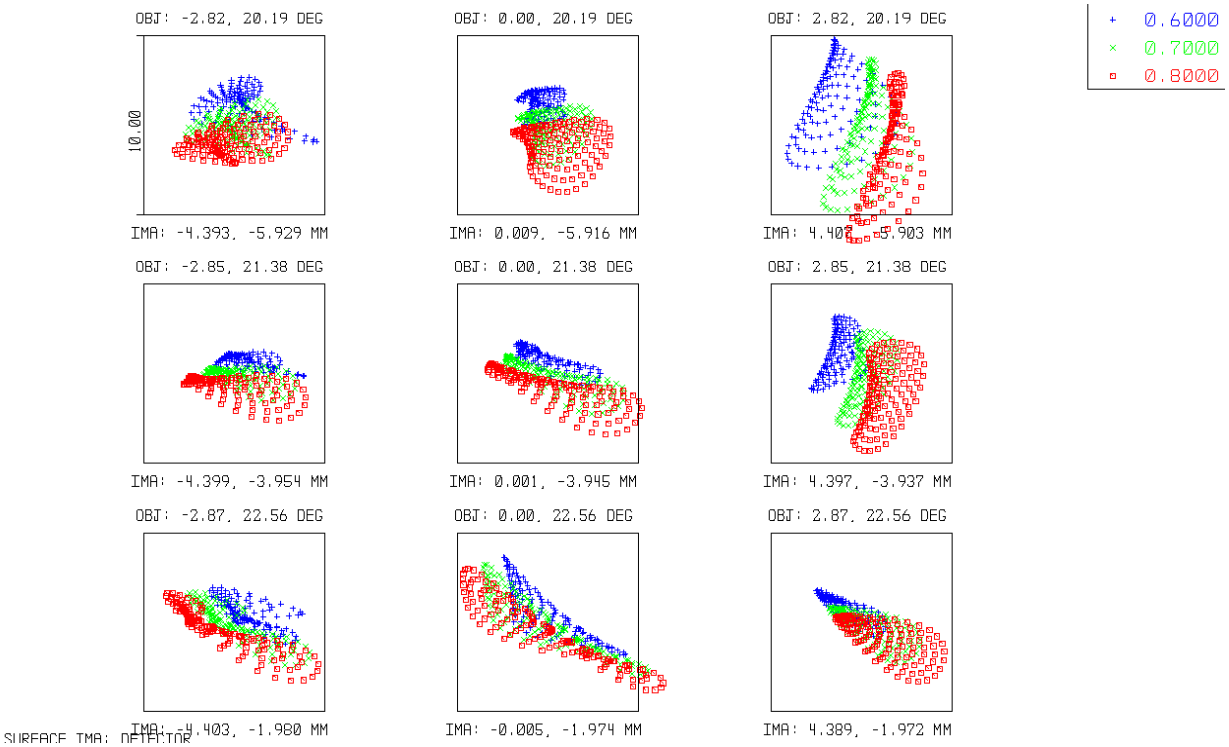

Figure 9 *(a) Spot diagrams in different points (boundary and center are presented in the same configuration of the effective one) of the detector plane for 3 different wavelengths in legend.(b)*

Also the MTF of the optical system has been derived for all the filters over the whole FoV. The mean MTF, at the Nyquist frequency of 50 cycles/mm, is of the order of 60-70%. As an example, the mean MTF for the panchromatic filter is shown in Figure 10 Considering that a reasonable value for the detector MTF is 50-60%, the global MTF of the system, including detector sampling, is of the order of 30-40 %.

In the analysis of this optical design, the study of the tolerances budgeting has also been performed. The tolerancing of a stereo camera is a challenging task: in fact, not only the desired performance has to be reached and maintained separately for each sub-channel, but also the combination of the two sub-channels and their mutual orientations have to be kept as fixed as possible during all the mission lifetime. Having in mind these considerations, an assessment of both manufacturing, alignment and stability tolerances has been undertaken.

This will provide an idea about the amount of work necessary to align the system and at the same time about the sensitivity and stiffness of the optical bench over which the optics have to be mounted. The criteria assumed in this analysis are that the image spot should not degrade by more than 30% its rms radius and that it should not be displaced more than half of a pixel.

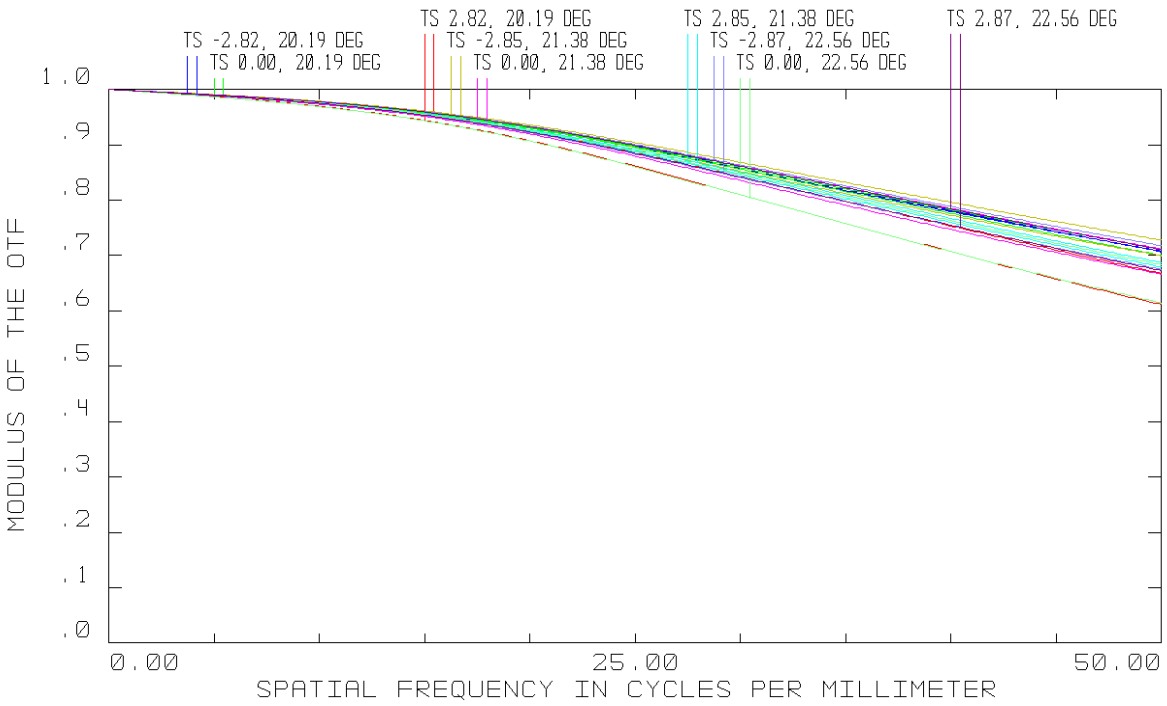

Figure 10 *MTF for the panchromatic filter*

The preliminary tolerance analysis results show that the achievable standard manufacturing tolerances of the optical shops for lenses and mirrors, (0.1-0.2% on curvature radius, 1 arcmin on surface parallelism, 10–3 on refractive index, ..), can be easily compensated by small adjustments during the camera alignment. More critical are instead the tolerances for maintaining the system in-flight performance. Two different subsets of stability tolerances have been considered: the short term tolerances, which have to be satisfied during the interval time needed for the acquisition of two stereoscopic image pair, and the long term ones, that have to be maintained during the whole mission. The former are relative to simple displacements of the boresight direction for each sub-channel, which are very sensitive to displacements and rotations of the spherical M1 mirror and to the rotations of the folding mirrors; the latter implies a degradation of the optical quality, which depends primarily on M1 movements and deformations, since almost all the power of the instrument is on that mirror.

Actually, the time interval between two stereo acquisitions of the same area is less than two minutes at the periherm (where most of the images will be acquired), so the mechanical design has to guarantee 2-3 µm mirror stability during this time interval, and alignment stability through the mission of the order of tens of microns.

Optical performance

The characteristics and foreseen performance of the Stereoscopic imaging Channel for the BepiColombo mission have been presented. The adopted solution, two sub-channels sharing most of the optical elements and the detector, is innovative for a planetary stereo camera, considering that classical stereoscopic designs typically consist of two completely independent twin cameras oriented at the desired stereo angle.
The innovations introduced in the system have brought to the idea of using an innovative algorithm for the 3D reconstruction. In fact, the problems associated to the Mercury environment, as described in first section of this chapter, will increase the already critical stability constraints typical of a space environment, mainly in terms of camera deformation and optical aberration. This is at the basis of our need to realize a more adaptable algorithm, aim of this thesis. If classical algorithms need a critical characterization of the camera system (see Section 3.2.1) to perform a suitable performing reconstruction, the new algorithm described in this work will allow to reconstruct the planetary surface using all the possible source of information from the images, with the only limitation of the used mathematical models. The results obtained after this process could be used as feedback to correct the same STC camera model and to correct the 3D reconstruction.

As the whole STC project, even the stereo-algorithm method here described is an ambitious activity. As will be shown in Chapter 5, trying to use at the same time more than one 3D reconstruction method to avoid the problem of considering the camera model brings timing problems and strong difficulties to create an computing structure able to control all the 3D methods used in the same time. On the contrary, our attempt to deal simultaneously with all the available information within the same code, showed very encouraging preliminary results, demonstrating that the algorithm is able to reach the performance of a classical stereo algorithm also with the use of a limited amount of information. On the other side, some work has still to be done: the STC instrument calibration will be the right moment for testing the algorithm, and for implementing the last changes.

References

[CAP05] F. Capaccioni, M.C. De Sanctis, G. Piccioni, E. Flamini, S. Debei and SYMBIOSYS International Team, "**VIHI: the Visible and Infrared Hyperspectral Imager channel of the SIMBIO-SYS instrument for the BepiColombo mission to Mercury**", *AAS/Division for Planetary Sciences Meeting Abstracts, vol. 37, 2005.*

[**CRE04]** G. Cremonese, M.T. Capria, V. Achilli, F. Angrilli, P. Baggio, C. Barbieri, J. Baumgardner, N. Bistacchi, F. Capaccioni, A. Caporali, I. Casanova, S. Debei, G. Forlani, S. Fornasier, D. Hunten, W.H. Ip, M. Lazzarin, I. Longhi, L. Marinangeli, F. Marzari, M. Massironi, P. Masson, M. Mendillo, B. Pain, G. Preti, R. Ragazzoni, J. Raitala, G. Salemi, M. Sgavetti, A. Sprague, E. Suetta, M. Tordi, S. Verani, J.K. Wilson and L. Wilson, "**MEMORIS: A wide angle camera for the BepiColombo mission**", *Advances in Space Research, vol. 33(12), pp. 2182-2188, 2004.*

[DAD08] V. Da Deppo, G. Naletto, G. Cremonese, L. Calamai, S. Debei and E. Flamini, "**A novel optical design for the stereo channel of the imaging system SIMBIOSYS for the BepiColombo ESA mission**", *in Proceeding of the '7th International Conference on Space Optics, Toulouse - France, 14-17 October 2008, 2008.*

[DEP10] V. Da Deppo, G. Naletto, G. Cremonese, and L. Calamai, "**Optical design of the single-detector planetary stereo camera for the BepiColombo European Space Agency mission to Mercury**", *App. Opt., vol. 49(15),pp. 2910-2919, 2010.*

[DEV78] M.E. Davies, S E. Dwornik, D.E. Gault and R.G. Strom, "**Atlas of Mercury**", *NASA SP-423, 1978.*

[FLA10] E. Flamini, F. Capaccioni, L. Colangeli, G. Cremonese, A. Doressoundiram, J.L. Josset, Y. Langevin, S.Debei, M.T. Capria, M.C. De Sanctis, L. Marinangeli , M. Massironi, E. Mazzotta Epifani, G. Naletto, P.Palumbo, P. Eng, J.F. Roig, A. Caporali, V. Da Deppo, S. Erard, C. Federico, O. Forni, M. Sgavetti, G.Filacchione, L. Giacomini, G. Marra, E. Martellato, M. Zusi, M. Cosi, C. Bettanini, L. Calamai, M.Zaccariotto, L. Tommasi, M. Dami, J. Ficai Veltroni, F. Poulet, Y. Hello and The SIMBIO-SYS Team,"**SIMBIO-SYS: The spectrometer and imagers integrated observatory system for the BepiColombo planetary orbiter**", *Planet. Space Sci., vol. 58, pp. 125-143, 2010.*

[HAY04] H. Hayakawa, Y. Kasaba, H. Yamakawa, H. Ogawa and T. Mukai, "**The BepiColombo/MMO model payload and operation plan**", *Advance in Space Research, vol. 33, pp. 2142-2146, 2004.*

[OBE03] J. Oberst, **"Topographic mapping: laser altimeter or stereo camera?"** *BepiColombo Imaging Team Meeting (2003)*

[SOL08] S.C. Solomon, R.L. McNutt Jr., T.R. Watters, D.J. Lawrence, W.C. Feldman, J.W. Head, S.M. Krimigis, S.L. Murchie, R.J. Philips, J.A. Slavin and M.T. Zuber, "**Return to Mercury: A global perspective on MESSENGER's first Mercury flyby**", *Science, vol. 321, pp. 59-62, 2008.*

[SLA97] J .A. Slavin, J.C.J. Owen, J.E.P. Connerney and S.P. Christon, "**Mariner 10 observations of field-aligned currents at Mercury**", *Planet. Space Sci., vol. 45(1), pp. 133-141, 1997.*

[THO07] N. Thomas, T. Spohn, J.-P. Barriot, W. Benz, G. Beutler, U. Christensen, V. Dehant, C. Fallnich, D. Giardini, O. Groussin, K. Gunderson, E. Hauber, M. Hilchenbach, L. Iess, P. Lamy, L.-M. Lara, P. Lognonné, J.J. Lopez-Moreno, H. Michaelis, J. Oberst, D. Resendes, J.-L. Reynaud, R. Rodrigo, S. Sasaki, K. Seiferlin, M. Wieczorek and J. Whitby, "**The BepiColombo Laser Altimeter (BELA): Concept and baseline design**", *Planet. Space Sci., vol. 55(10), pp. 1398-1413, 2007.*

Chapter 5

A new stereo algorithm based on snakes

Contents

Introduction

As part of the ongoing activities for the space mission BepiColombo to Mercury, a new stereo-matching algorithm is proposed that uses **deformable surfaces** or **snakes** (see Chapter 3) in order to find a **dense** disparity map. Under the external forces, represented by a similarity function, and the internal ones, represented by smoothness constraints on the disparity, the disparity map evolves as a deformable model from an initial approximation state until convergence. The algorithm called *SIEM (Stereo Images Evolving Models)* is expected to provide one of the image matching tools for the Digital Terrain Model generation procedure for the stereo camera on board of BepiColombo. Tests have been performed on synthetic images derived from 3D models of geological features relevant to planetary science. The results show an image measurement accuracy comparable to that of the Least Squares Matching (LSM) algorithm; besides, less object smoothing is obtained, i.e. more details of the terrain can be captured, because the object points do not derive from an implicit averaging over a terrain patch as in area-based methods. Finally, because of the continuity constraint, the method is also expected to feature robustness against blunders in the reconstruction of the parallax field.

5.1 Context

Digital terrain models of rocky celestial bodies

The success of the Mars Express mission ([ALB05],[SCH05]) has perhaps marked a turning point, making full stereo coverage of rocky planets and asteroids a must-have in today's planetary space science missions. This witnesses the increasing importance given by planetary science, and in particular by planetary geology, to the production not only of maps and orthoimages but also of accurate Digital Terrain Models (DTMs) and photorealistic 3D models of planet surfaces.

The scientific goals and the missions constraints, as for example payload mass and data volume, make the design of on-board instruments and sensors specific to each mission. Thus, the sensor architecture and characteristics have to be carefully designed to meet the usually very stringent scientific goals, staying within the normally low available mass and power resources. Moreover, the observation strategy has to be defined on the basis of the orbit characteristics, of the total available data rate and volume, of the compression algorithms, and of the on-board mass memory: all these constraints affect the quality of the data as well as the data processing strategy. This is particularly true for the satellite instrumentation dedicated to planetary surface reconstruction from stereo images ([NEU04]; [MCE07]): in fact, in this case great care has to be put not only on the quality of the sensor, but also on the knowledge of the imaging geometry and on the accuracy of the image matching algorithms. DTM production on a planetary scale from a space mission is a highly articulated procedure, where most of the steps (pre-processing, filtering, coarse-to-fine, matching on pre-rectified images) can be anticipated to be necessary. Their actual implementation and their relevance to the final quality of the DTM is nevertheless specific to the mission and must be refined in a continuous improvement process ([HEI07]; [KIR08];[GWI08]).

Image matching for surface reconstruction

Automatic surface reconstruction from stereo or multiple images has been during the last decades a major subject of investigation; many image matching algorithms have been proposed (see Chapter 3) and successfully implemented in commercial and scientific computer programs. Ideally, matching algorithms should provide accurate (possibly sub-pixel), evenly distributed and dense correspondences between images. They are often grouped in two main categories: feature-based matching (FBM) ([FOR84]) and area-based matching (ABM) [ACK84].

FBM extract features from images and then applies some similarity measure to indentify correspondences. Distinct features are extracted using interest operators [SCH00]; many interest operators have good invariance properties and sub-pixel accuracy. Feature matching is often implemented in a global optimization scheme, to find a subset of correct matches from lists of potential candidates, enforcing the available constraints to reduce the search space. Though most commercial DTM generation software is based on ABMs, some uses FBM ([KRY91];[LEM08]).

ABM can be applied either in image or in object space. Stereo matching in image space, the most extensively studied and applied, works maximizing the similarities between a window in a reference image (template) and another scanning window in a slave image (patch). Of all the developed algorithms, the least squares matching (LSM) [GRU85] has probably the best potential accuracy and the capability to account, to some extent, for the radiometric and the perspective differences between template and patch. Nevertheless, LSM is a local method, that needs good initial values of the input parameters to avoid convergence to false matches; it may fail in areas with poor image texture or repetitive patterns; large templates may help to cope with image noise but at the price of more terrain smoothing and less successful matches in rough terrain; small templates are sensitive to noise and initial values of parameters. To improve reliability (identify and reject mismatches), increase convergence speed and produce a dense point cloud, DTM generation programs embed LSM in an articulated workflow (coarse-to-fine, epipolar resampling, constraints on disparity, etc.).

Multi-image methods have been introduced, such as multiphoto geometrically constrained matching (MGCM)[GRU88] that effectively combine the simultaneous LSM estimation process between a template and several patches with geometric constraints in object space, forcing the homologous rays to intersect. The more images are available the better the reliability of the match; the method has been shown to be robust to occlusions and poor initial values of LSM parameters [BAL91]

Matching in object space includes in the mathematical model the relationship between image grey values and some suitably defined object intensity values (radiometric model) as well as the collinearity condition (geometric model); the object surface is modeled by finite elements [HEI92]. The image formation process is described accounting for the reflectance properties of the object surface and scene illumination, with some necessary approximation (e.g. perfect Lambertian reflection); either stereo or multi-image matching can be performed. Matching in object space has been proposed in several variants ([HEL88]; [EBN88]; [WRO87]; [KRU97]). Theoretically, since there is a physical modeling of the observables and a global reconstruction of the object surface, it offers a better consistency, potential reliability and flexibility than local ABM, at the price of a more complex and computationally demanding algorithm.

During last years, an increasing amount of research effort has been focused on a novel approach to stereo image matching, based on deformable surfaces. *Active contours*, or *snakes*, are mathematical deformable models mainly used in image segmentation. In these applications, they are closed structures that, from an initial state, deform themselves to converge to the border of a target region in the image. Suitably defined external forces act on the snake, trying to change its shape; internal forces react trying to maintain a degree of smoothness of the curve. An external energy function and an internal energy function are associated to the forces and can be computed for every step of the snake evolution; by minimizing the sum of the two energy functions, the snake will find its final shape, where internal and external forces are balanced. The 3D version of snakes is often known as *deformable models* or *active surfaces* in literature.

Active contour models for monocular images have been extensively studied and used in many applications such as facial image processing [DEC00,] object tracking [GRE07], and medical imaging [MCL96]. Unfortunately, some limitations are intrinsic to this method, because the performance of snakes significantly degrades when boundary concavities, object occlusions, background noise and clutter are present. However, the snake approach permits the simultaneous use of all the information provided by the image and can be extended to different 3D reconstruction methods. Thus, different and innovative strategies have been developed to use this tool for stereo reconstruction. For example, Kim [KIM06] proposed a snake-based algorithm for object segmentation in stereo images: this algorithm first calculates a disparity map using a region-based stereo matching technique, and then uses this disparity map to compute the external energy term of the snake; alternatively, in his thesis Ghaffari [GHA02] used evolving snakes to compute the disparity map step by step for the segmentation of medical images from color stereo pairs.

A new image matching algorithm

As seen in Chapter 4, one of the scientific goals of the BepiColombo ESA-JAXA space mission to Mercury is the global mapping of the planet, that will be performed by the Stereo Camera (STC) [CRE09], part of the SIMBIOSYS suite [FLA10]on board. As part of the development activities of the STC and of the planning of planet mapping, a new stereo matching algorithm (SIEM) has been developed, where snakes (represented as “Evolving Models” in the acronym of the algorithm)are used as a tool to evolve an initial approximation of the stereo pair disparity map until an optimum global correspondence between the images is found. The smoothness of the disparity map is the internal force driving parameter, while a similarity function is the driver for the external forces. Since all the information is simultaneously optimized, in the final matching map every

point corresponds to the optimal minimization of the applied constraints. Notice that usually in planetary space missions the extrinsic parameters are not well known; our approach does not need this information but only the image constraints. The disparity map can be computed on a pixel-by-pixel basis, providing a very dense information for surface reconstruction; compare to of ABM methods, the object smoothing due to template size is expected to be significantly smaller. As for matching in object space, since the optimization is global, a better reliability with respect to local FBM or ABM methods is also expected.

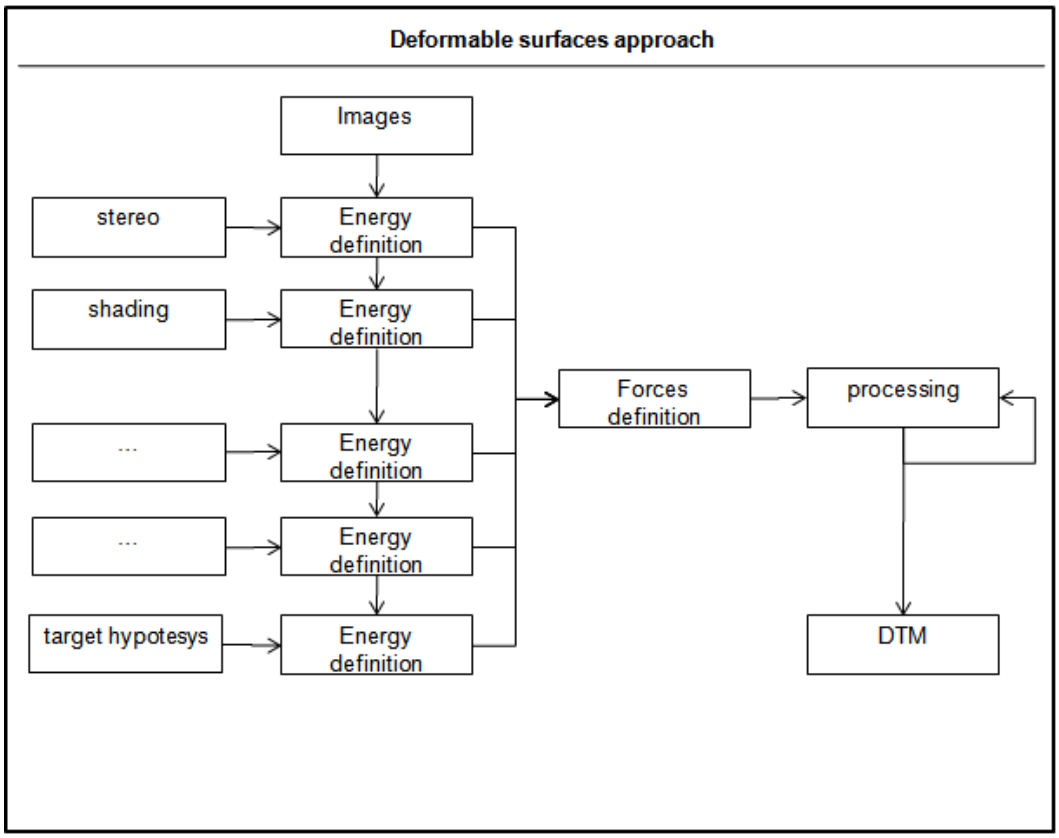

Figure 1 *Approach used by the algorithm SIEM instead of the classical pipeline, all the constrains are use for a definition of the energies and so of the forces. All information is then used in synchronic way.*

In the next second sections an overview and a generalization to the multidimensional case of the snake method is given. Then, a definition of the stereo-snake, of the dual forces and some algorithmic details are provided in the following two sections. Finally, the informatics architecture of the implementation of the SIEM is described in details..

5.2 Stereo matching with Deformable surfaces

Let us now consider a stereo image pair of an open surface and let us assume that there are no occlusions in the images (see Section 4); for simplicity, let both images have the same square size $N \times N$. This implies that the map $\Omega_{22}: N^2 \to N^2$ between the coordinates (i_1, i_2) of the first image and the coordinates (u_1, u_2) of the second image yielding the disparity map D is continuous, bijective and monotonic along the baseline direction (see Figure 2).

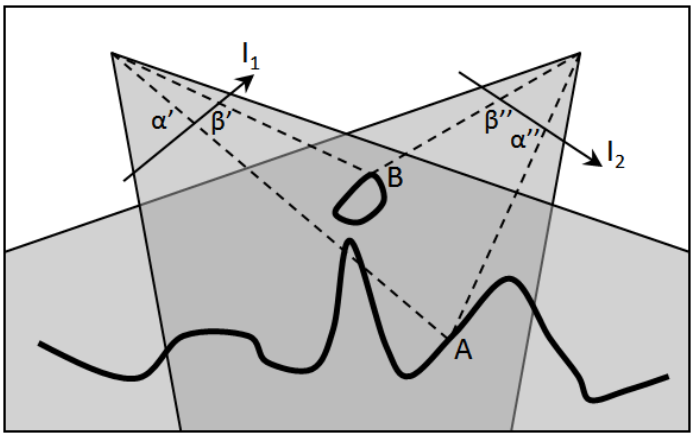

Figure 2 *Example of object surface discontinuity and occlusions in stereo image (the images are drawn as oriented line segments). Object discontinuity in this case leads to an inversion of the map (given α', β' and α'', β'', projections of A and B on the first and second images respectively, it is immediate to verify that they are inverted in the two images).The point A is not seen in the left image because of an occlusion due to a prominent surface feature.*

A significant advantage of the adopted *snake* definition when applied to tridimensional reconstruction from stereo images is that it allows to compress the disparity information. Rather than the classical disparity map D, it is possible to use the *relative* one $\mathfrak{D}$ defined as the map $\Omega_{22}: N^2 \to U \times V$ between the coordinates (i_1, i_2) of the first image and the relative coordinates $(u_1 - i_1, u_2 - i_2)$.

Since, as can be easily verified, $U, V \leq N$, the codomain of the relative disparity $\mathfrak{D}$ is generally smaller than the codomain of D one, allowing to reduce the array size and the amount of calculation in the algorithm implementation.

The *deformable surface* we evolve for this stereo algorithm is the relative disparity map $\mathfrak{D}$ itself. According to Equation 16 of Chapter 3 both the external and the internal energies of the snake must be defined. As far as

the external forces, $\mathcal{F}_e{}^{(S)} = -\nabla_u \mathcal{E}_e{}^{(S)}$, are concerned, a suitable external energy can be the similarity function $\mathcal{C}$, represented by the cross correlation coefficient between matching windows. For easiness of calculation, we inverted the sign of the external forces and applied a normalization such that $\mathcal{C}$ = 1 in the ideal matching case and $\mathcal{C} = -1$ in the worst case. On the other hand, the internal forces $\mathcal{F}_i{}^{(S)} = \Delta^i S$ remain the same. Thus, by inverting the sign of the external forces and substituting the relative disparity $\mathfrak{D}$ for the snake *S*, Equation 16 of Chapter 3 can be rewritten as:

$$\dot{\mathfrak{D}} = \mu\left(\sin\theta\, \nabla_u \mathcal{C}^{(\mathfrak{D})} + \cos\theta\, \Delta^i \mathfrak{D}\right) \quad (1$$

where the forces are expressed by:

$$\mathcal{F}_e{}^{(\mathfrak{D})} = \nabla_u \mathcal{C}^{(\mathfrak{D})} \quad (2$$

$$\mathcal{F}_i{}^{(\mathfrak{D})} = \Delta^i \mathfrak{D} \quad (3$$

The notation Δ^x represents the vectorial Laplacian along the x_i coordinates: $\Delta^x = \sum_i \frac{\partial^2}{\partial x_i^2}$.

As an example of the usefulness of this approach in reducing the amount of calculation, let us consider the simple case of epipolar resampled images. In this case, all the points in a row of the first image have their homologous on the same row of the second image and so the stereo process can be considered as a separate process applicable to all the different lines of the image. Figure 3 shows, in the case of a pair of one-dimensional stereo images $I_1(i_1)$ and $I_2(u_1)$, the similarity function $\mathcal{C}$, that is the values of the NCC (Normalized Cross Correlation) [LEW95] between a matching window centered on i_1 on the first image and on u_1 on the second. The stereo correspondence problem can be solved by optimization of the path on the similarity function image (see Figure 3.a), obtaining the disparity map D, shown as a dotted line. In Figure 3.b the same similarity function and the relative disparity map $\mathfrak{D}$ are shown; the significant reduction of the array size is obvious.

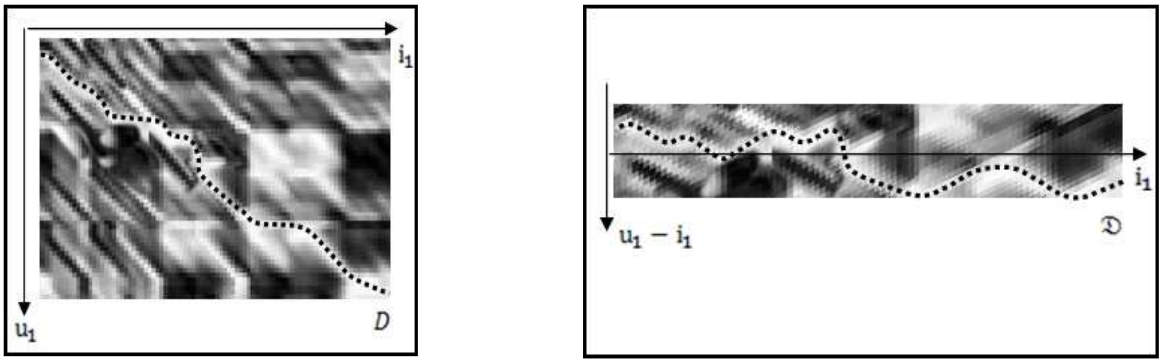

(a) (b)

Figure 3 *Example of disparity and relative disparity maps for two stereo one-dimensional images* $I_1(i_1)$ *and* $I_2(u_1)$ *representing the same target. We can express the second image* $I_2(u_1)$ *as the result of the mapping D and we can write* $I_1(i_1) \approx I_2(D(u_1))$*. (a) shows the values of the NCC between a matching window centered on* i_1 *on the first image and on* u_1 *on the second (dark points correspond to low correlation while bright ones to high correlation); the dotted line is the searched disparity map. (b) shows in the "relative" representation the same similarity function and disparity map*

External forces implementation

In order to implement the definition of external forces, given by equation (**2**), the gradient of the similarity function is computed by the approximation of the similarity function $\mathcal{C}$ with a bicubic interpolation in a 4x4 neighborhood.

The similarity function is computed with a fast NCC [LEW95] and, to speed up the algorithm, is performed in a preprocessing phase.

For the convergence of the snake evolution an accurate and robust boundary estimation of $\mathfrak{D}$ is necessary. The better the approximation, the smaller the processing time and the memory requirements. To estimate the borders $\mathcal{B} = \{x_s, x_e; y_s, y_e\}$limiting of the components $\mathfrak{D}_x, \mathfrak{D}_y$ of $\mathfrak{D}$ ($x_s \leq \mathfrak{D}_x \leq x_e$ and $y_s \leq \mathfrak{D}_y \leq y_e$) a *greedy* procedure is performed (see block diagram in Figure 5): the boundaries are estimated for a limited set of points and their definition is then extended for continuity to the whole image.

A uniform grid of points $[p_1]$ is considered on the first image. For all the points $p_1^i \in [p_1]$ with a local variance greater than an empirical threshold τ, the homologous points p_2^i are chosen in the second image by a search limited by fairly large borders $\mathcal{B}_0$. In this way, a first approximation $\mathfrak{D}_0$ of the relative disparity map for the considered points is computed.

By segmentation of the bidimensional histogram $\mathcal{H}$ of $\mathfrak{D}_0$ the same map, a new boundary $\mathcal{B}_1$ is evaluated (see below) and a *greedy* procedure for the estimation of the relative disparity $\mathfrak{D}$ and of the relative boundary $\mathcal{B}$ is performed.

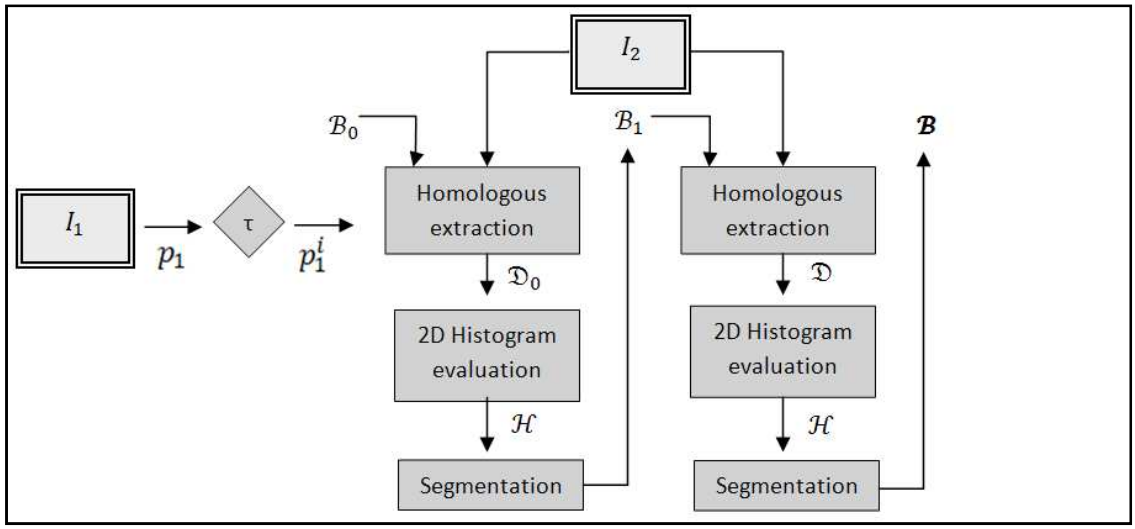

Figure 4

Block diagram describing the procedure to evaluate the relative disparity map boundaries. The p_1^i points selected from the grid $p_1$of the first image are used to compute the 2D Histogram evaluation of the relative disparity. Through histogram segmentation a first estimate of the boundaries is computed. The whole procedure is repeated twice to improve the results.

To better visualize this process to estimate the boundaries of the relative disparity map $\mathfrak{D}$, let us consider an example with a pair of stereo images (see Figure 5). Given a grid of points $p_1^i = (x_1^i, y_1^i)$ on one of the images (red crosses in Figure 5.a), the homologous points $p_2^i = (x_2^i, y_2^i)$ in the other image (blue crosses in Figure 5.b) can be determined by maximization of the similarity function calculated over the whole image.

The relative disparity $\mathfrak{D}$ between the two grids of points is used for a statistical analysis of the disparity over all the image. The bidimensional histogram of $\mathfrak{D}$ is defined as the joint frequency distribution $P\big(x = x_1^i - x_2^i, y = y_1^i - y_2^i\big)$. The relative disparity histogram is shown in Figure 5.c. The histograms of $\mathfrak{D}_x$ *and* $\mathfrak{D}_y$the horizontal and vertical coordinates of are shown in Figure 6d; the continuity of the target surface guarantees a compact histogram for both coordinates.

By histogram segmentation, the region of the domain of the disparity covering the 90% of the statistics is found, to separate the outliers from the kernel of the disparity. This allows to define the statistical limits of $\mathfrak{D}$ and reduces its co-domain from the initial value of N^2 to the final value $U \times V$.

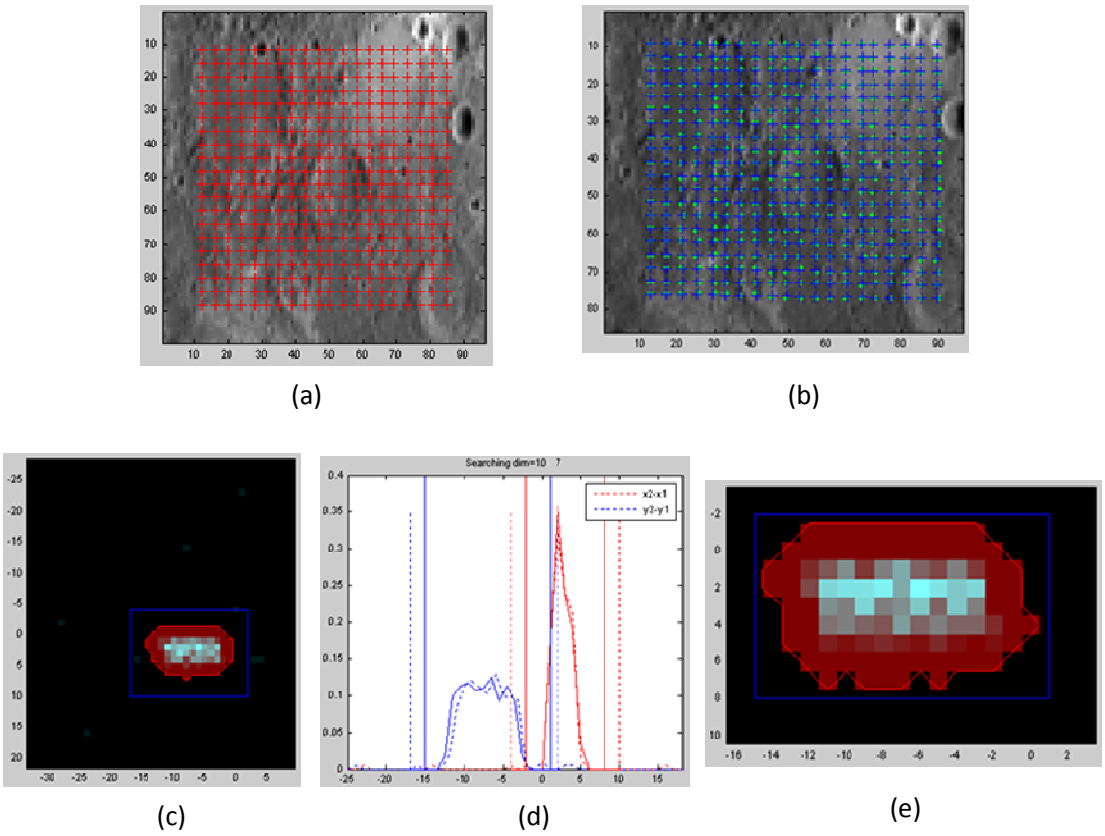

Figure 5 *Determination of the disparity map bounds by statistical analysis. From left to right and top to bottom: a) grid of points* $[p_1]$ *in the reference image; b) grid of points* p_2^i *in the search image; c) statistical bidirectional histogram of the relative disparity* $\mathfrak{D}$ *(the borders obtained by the segmentation are shown in red, while in blue are the resulting boundaries* $\mathcal{B}_1$*); d) statistical histogram for* $\mathfrak{D}_x$ *(red) and* $\mathfrak{D}_y$ *(blue); e) statistical histogram after the new search based on the use of* $\mathcal{B}_1$ *instead of* $\mathcal{B}_0$*.*

After the determination of these boundaries (drawn in blue in Figure 6d and 6e), the similarity function for the matching analysis is computed for all pixel coordinates(i_1, i_2) the function value.

Therefore we can define:

$$\mathcal{C}(i_1, i_2, x, y) = \mathrm{NCC}\big(I_1(i_1, i_2), I_2(u_1, u_2)\big) \qquad (4$$

where

$$\begin{cases} u_1 = i_1 + x \\ u_2 = i_2 + y \end{cases} \text{and} \begin{cases} x_s \le x \le x_e \\ y_s \le y \le y_e \end{cases}.$$

After the definition of the boundaries, the hypercube $\mathcal{C}$ can be evaluated without memory or processing time problems and registered in memory for subsequent use.

To have a better estimate of the local gradient of the similarity function $\mathcal{C}$ along the *x*,*y* coordinates, as required by equation (**2**), for each point (i_1, i_2) on the reference image a 4×4 pixel window is considered in the $\mathcal{C}$ hypercube around the current associated value of the disparity map $\left(D_x(i_1, i_2), D_y(i_1, i_2)\right)$. More in detail, for each point (i_1, i_2) a subset of the hypercube defined by $\mathcal{C}\left(i_1, i_2, D_x(i_1, i_2) + k, D_y(i_1, i_2) + h\right)$ where $(-1 \leq k \leq 2$;and $-1 \leq h \leq 2)$ is considered. Then, a Hermite bicubic surface is interpolated in the 4 x 4 window (at the window corners, the similarity value and its derivative are preserved in the interpolated surface) and at this point the local gradient can be calculated with good accuracy. An example is shown in *Figure 6* where the maximum is reached for *k*=*h*=2: during the evolution of the *deformable surface*, the point optimizes the similarity function moving from its initial position in the middle (*k*=*h*=1.5) to the maximum value of about 1.

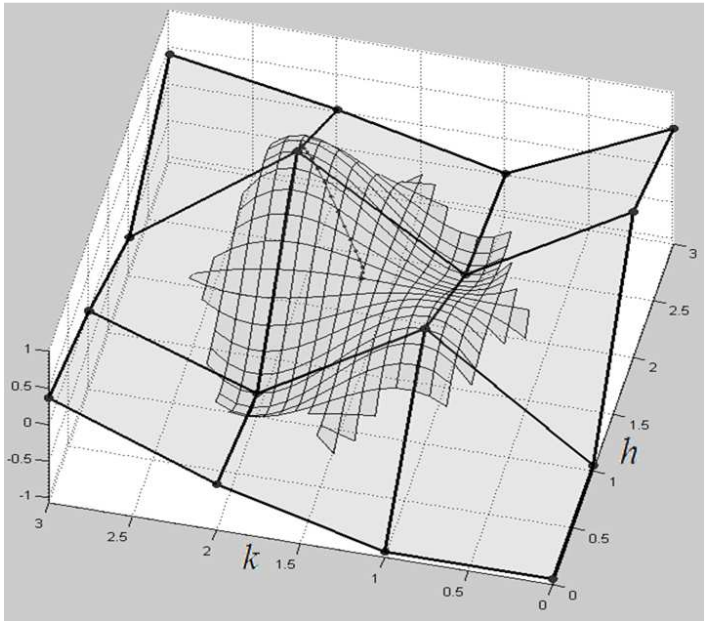

Figure 6 *Interpolation of the similarity function. A grid of* 4×4 *values of the similarity function and the interpolation function are shown. The optimization path is also shown by the position at every cycle of the algorithm of the snake-point moving towards the local maximum.*

Internal forces implementation

As shown above, any point of the reference image (i_1, i_2) can be associated to the time dependent value of the disparity map $\mathfrak{D}(i_1, i_2) = \left(D_x(i_1, i_2), D_y(i_1, i_2)\right)$. This value will change in optimization process of the similarity function because of the external forces. However, without other constraints, this will lead to an optimization of the similarity content for each points without a mutual correlation (interdependence) between the resulting $\mathfrak{D}(i_1, i_2)$ and its neighborhood. This could create unrealistic cases, such as the local peak shown in Figure 7.

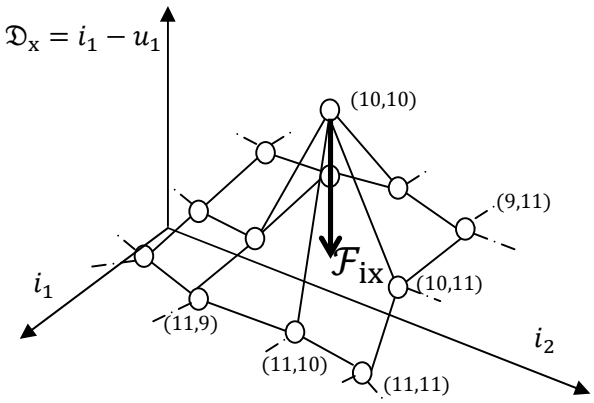

Figure 7 *Example of a possible configuration of the $\mathfrak{D}_x$ component of the relative disparity map. If the external forces produce an isolated peak in $\mathfrak{D}_x$, the $\mathcal{F}_{ix}$ component of the internal forces (shown for the point (10,10)) will react to smooth it.*

To avoid such cases, we can use the internal forces, defined in equation **(1**(**3**) as:

$$\mathcal{F}_i{}^{(\mathfrak{D})} = \Delta^i \mathfrak{D}.$$

The Laplacian effectively prevents the presence of peaks. To speed up the computation, the Laplacian of the two relative disparity components is considered separately:

$$\mathcal{F}_{ix}{}^{(\mathfrak{D}_x)} = \left(\frac{\partial^2}{\partial {i_1}^2} + \frac{\partial^2}{\partial {i_2}^2}\right)\mathfrak{D}_x \qquad (5$$
$$\mathcal{F}_{iy}{}^{(\mathfrak{D}_y)} = \left(\frac{\partial^2}{\partial {i_1}^2} + \frac{\partial^2}{\partial {i_2}^2}\right)\mathfrak{D}_y$$

The two components of equation (**5**) are computed applying an isotropic Laplacian filter:

$$\mathcal{F}_{ix}{}^{(\mathfrak{D}_x)} = L * \mathfrak{D}_x$$
$$\mathcal{F}_{iy}{}^{(\mathfrak{D}_y)} = L * \mathfrak{D}_y \qquad (6$$

Where "$*$" represents the bidimensional convolution and *L* the 9-points McClellan filter(Sergey, 1997):

$$L = \begin{bmatrix} 1/4 & 1/2 & 1/4 \\ 1/2 & -3 & 1/2 \\ 1/4 & 1/2 & 1/4 \end{bmatrix}$$

On the borders of the disparity map the Laplacian cannot be defined as in equation (**6**).This problem is solved by zero-padding and the iteration around the borders has to be computed to normalize the Laplacian filtering local results.

Since the Laplacian is not defined on the image borders, without some normalization or regularization condition applied to the borders, lack of proper application of the internal forces might cause the border points to react to force impulses by absorbing all the energy or, vice-versa, reflecting it back.

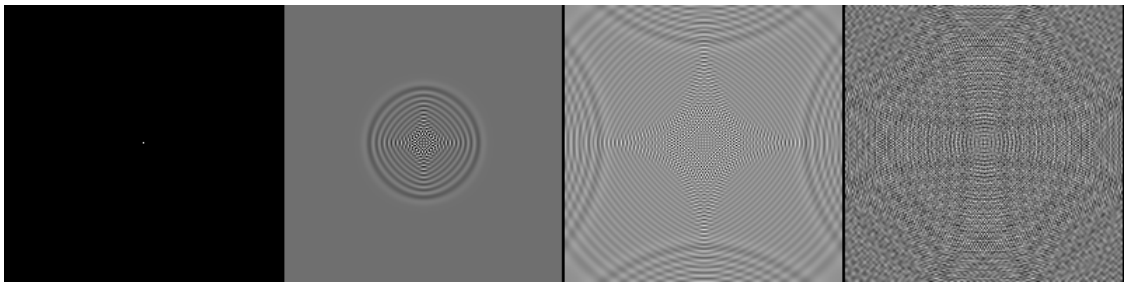

Figure 8 *The figure shows the evolution in different moment of the iteration cycles of the snake in the particular case of the absence of normalization on the borders. A Chromatic scale variation was used to appreciate waves propagation*

To explain this need we consider for a moment the disparity as oriented just on one of its component (horizontal or vertical components). In this case the disparity can be represented as a surface. This is the case of rectified images.

If we suppose that the initial snake is completely null a part of the central pixel where it is characterized by a peak and we evolve the internal forces we obtain the reflection of the components on the border as shown in Figure 8.

By applying a normalization on borders (weighing the filter coefficients in a local manner), the limits of the *deformable surface* do not represent an absorbing or hyperkinetic structure, making the *snake* inertia uniform all over the image.

5.3 Architectural Structure

The greedy algorithm at the basis of the new method here introduced for the analysis of the STC images was developed using two different software environment: MATLAB and C++. This chapter describes the program structure, its architectural design and the main parts in which it is developed. Although the program is still under development (for instance the self calibration is not yet implemented, and not all the possible forces used for the evolution of the snakes are defined), the design here described demonstrates its extendibility and its future-looking organization.

5.3.1 Introduction

The SIEM (*Stereo Images Evolving Models*) represents a snakes' based stereo algorithm mainly realized for imaging analysis of planetary surfaces. This software was developed in the framework of a collaboration among the Italian INAF, the CISAS University of Padova, the Department of Civil engineer of the University of Parma, and with the help of the DLR institute of Berlin.

As explained in Chapter 5 the work has to be interpreted in the wider context of the ESA-JAXA BepiColombo mission, which is the first mission finalized to the topological and morphological complete study of the surface of Mercury.

Berlin DLR institute had a significant importance in the evolution of the algorithm and software, since it supplied test images of the Mercury surfaces from the first flyby of MESSENGER in January 14, 2008. Other very representative stereo test images are granted by a collaboration between INAF and Prof. Haruyama, the PI of the JAXA mission Kaguya (SELENE) to the Moon: stereo image pairs of the Moon surface obtained by the stereo Terrain Camera are made available and have been used for testing the program performance.

5.3.2 Scope of the software

SIEM will provide the stereo-DTM reconstruction for planetary surfaces. Considering the problems of acquisition of stereo-images in long baseline geometrical configuration, as well the problems of camera model definition, which is normally affected by not well known geometrical distortion, the software has the task of both extracting the parameters concerning the self-calibration of the stereo system and realizing the affine reconstruction of a 3D model. The basic hypotheses of the algorithm permit to apply this method to all kind of

surface reconstruction: by integrating both stereo reconstruction and shape from shading, it uses all the available information in the images; moreover, evolving by means of a self-automatic method, it greatly reduces the user work.

It is also worth mentioning that the code has been designed in a modular way, having in mind the possibility of adding in the future new type of information or "dual forces" (see Chapter 5.1).

Primary SIEM principal aims:

- DDM[1] Disparity map evaluation for planetary surface stereo couple.
- Ortho-image self-generation;

SIEM software's benefits and goals are:

- The software is extended to missions different from the survey for which is performed;
- The adopted methodology can be used for future mission planning;
- No input data are needed except the original satellite images; for the Disparity generation
- GUI (Graphic User Interface) routines can be easily implemented: they allow not only to easily manage all the software parameters, but also to perform a quick look analysis of planetary features.
- Coherent integration of shape from shading is the next step for an optimal utilization of the available information.
- Adaptability of the structure permits future integration of all kind of information required to gain best results from image reconstruction.

Relation to current projects

Classical photogrammetric software as ENVI[2] or DLRmatch[3] need specific knowledge to determine the metrical parameters of a surface acquired by two different points of view. This knowledge normally is determined in different ways by on-ground or in-flight calibration methods.

[1] See Chapter 3 for definition

[2] ENVI is a software application currently marketed by ITT Visual Information Solutions used to process and analyze geospatial imagery. It is commonly used by remote sensing professionals, scientists, researchers, and image analysts

[3] Software developed by DLR Institute in Berlin and used for the analysis of Messenger and Mars Express images.

Up to now, to author knowledge, no reduction tool similar to the one described in this work has been developed. The proposed automatic pipeline is intended to be a tool performing all relevant analyses and management of observational data.

5.3.3 Function and purpose of the software

The purpose of SIEM is to provide an automatic geometrical calibration and photogrammetric elaboration for planetary images. SIEM not only could support future missions dedicated to 3D reconstruction of planetary surfaces, but also it might be a new method for the analysis of old datasets: in fact, considering the amount of information used by this algorithm with respect to classical image analysis methods, it is evident that great improvement in the data analysis can be obtained.

To this end, the pipeline shall provide sufficient functionality, versatility, and extensibility.

Environmental considerations

The Users of this software will be scientists and technicians with different levels of:

i. knowledge of the photogrammetry;
ii. reasons of usage of the software;
iii. expectations to the functionality of the software.

All these aspects are assumed to be appropriate guidelines to define the way in which the Users will interact with the software, and the level of required performance and reliability. These guidelines trace the necessary background in astronomical reduction technique, in planetary transit technique, in observational strategy technique required for the S/W utilization.

Thereby, the Users of the software will be:

- ➢ *Scientists with specific knowledge* of photogrammetry: they need a software which automatically generates the surface reconstructions of the survey targets from the raw images analysis; the software has to allow the change of the force parameters, to be able to detect different surface features, or to add new force definitions to improve the algorithm performance.
- ➢ *Scientists with basic knowledge* of imaging or geology who shall exploit the SIEM to analyze and compare different morphological planetary features, as creaks or craters or mountain.

At the present state, the software runs on all the systems equipped with the following minimal resources:

a) a Pentium IV workstation with 2 GHz, 2Gb RAM, 100 GB free disk space at least, disk access time of 10 ms and a screen resolution of at least 1152 x 900 pixels;
b) OS: Windows (all versions) Linux with Fedora 6.0 OS;
c) Matlab (version after v6a).
d) Microsoft Visual Studio (version after 2005)
e) LibTiff, LibJpg, Vigra C++ Libraries;
f) Indeo5 Video codec.

Points (d) and (e) will be removed after the integration of the C++ DLL (*Dynamic Link Library*) in the user interface.

5.4 System Overview

The Software is actually divided in two main part: the **SIEM,** *Dynamic Link Library in C++* for the algorithms architecture and the **GUI**, *Graphical User Interface*:

SIEM
This block of the code supplies the new method for the surface analysis, by means of the complete integration of all the information that can be extracted by images, and of all topological hypotheses that have to be fixed.

This is a C++[4] dynamic link library based on the definition of the DDM, the *Digital Disparity Model*, given by the evolution of a deformable model subject to different multi-dimensional forces.

At the present state, the definition of the internal forces includes the hypotheses on continuity and rigidity of the planetary surface, as well the stereo constraints. Other routines have still to be included to reach the full integration of shape from shading.

[4] C++ is a statically typed, free-form, multi-paradigm, compiled, general-purpose programming language. It is regarded as a "middle-level" language, as it comprises a combination of both high-level and low-level language features.

GUI

GUI is a user interface toolbox for the visualization and for the analysis of extracted data. Developed in MATLAB[5], it permits the pre-processing analysis of the images, the choice of the parameters for the algorithm and the creation of different instances for the SIEM.

On the other side the plug-and-play interface represents the basis for a real instrument for planetary surface analysis. After the integration of the geometrical conversion to transform DDM to a DTM, GUI shall rescue the tools for the measurement of features and slide analysis.

5.4.1. Design method (Data formats and protocols)

The design method used in the realization of this software is the object-oriented one. In particular we used the *Object Modeling Technique* (OMT)[6] [TER97]. The presented model is a decomposition view into components. A top-down approach is used to decompose the system.

The format for the implementation of the force structure has been chosen in such a way to allow its extendibility.

Considering that the algorithm is based on an iterative cycle in which the forces applied to the snake (or disparity map), which is a bi-dimensional data, are suitably changed, a raster[7] implementation of this information was used. The snake, as well every kind of force, is defined as double array data vector with the same dimension of the considered images.

The system is so easily extendible to any other kind of force (see Figure 9). For instance, the crater shape, defined by the impact crater history, could be modeled as a force applicable to the disparity map; the

[5] MATLAB® is a high-level language and interactive environment that enables you to perform computationally intensive tasks faster than with traditional programming languages such as C, C++, and Fortran.

[6] The object-modeling technique (OMT) is an object modeling language for software modeling and designing. It is a method to develop object-oriented systems, and to support object-oriented programming. The purposes of modeling are: testing physical entities before building them (simulation), communication with customers, visualization (alternative presentation of information), and reduction of complexity.

[7] In computer graphics, a raster graphics image or bitmap is a data structure representing a generally rectangular grid of pixels, or points of color, viewable via a monitor, paper, or other display medium. Raster images are stored in image files with varying formats (see Comparison of graphics file formats).

implemented software design would permit to add to the system two new double arrays (horizontal and vertical components) in which the information is collected.

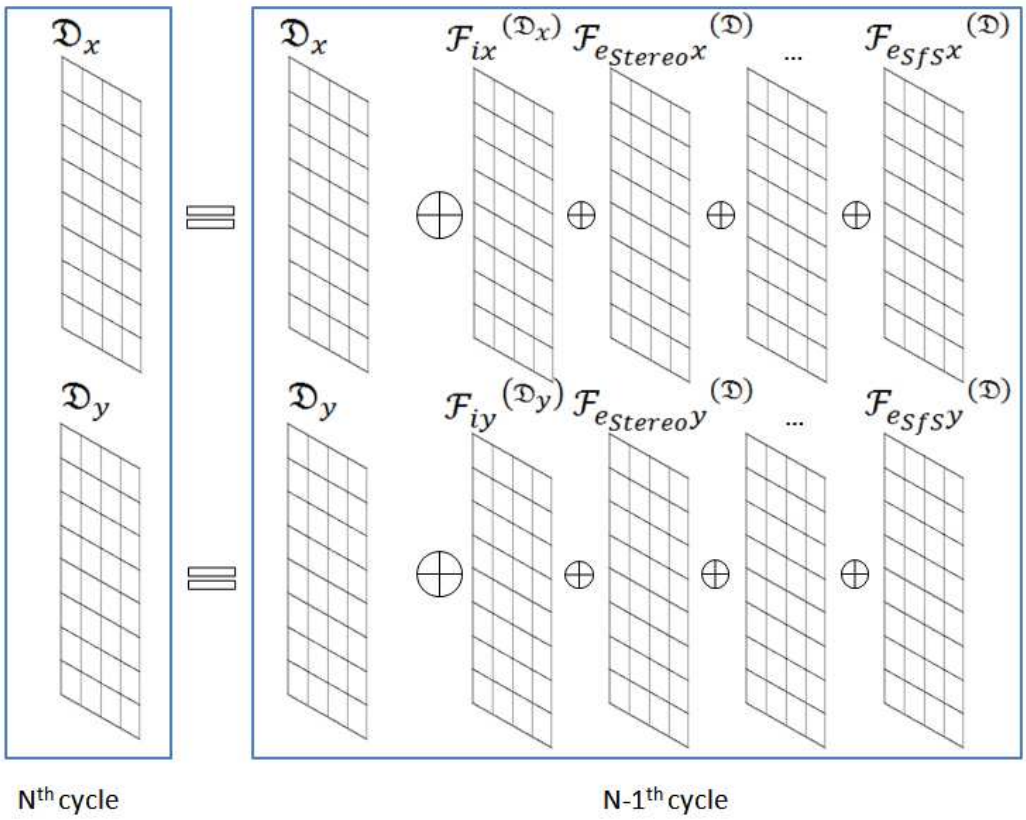

Figure 9 *Schematic design of the informatics definition of the disparity map and of the applied forces. At every cycle of the algorithm, the elaboration of the new disparity map components D_x, D_y is computed by adding the different kind of forces to the previous components. In this figure, the internal forces F_i, the stereo external Forces F_e-Stereo, the forces linked to Shape From Shading F_e-Sfs, and a possible additional force are indicated.*

The assumed data design has forced the adoption of two important protocols for the interfaces between the different blocks of the software:

- **SDP** (*Stereo Data Protocol*)

- **EMP** (*Evolving Model Protocol*)

These protocols are described in following paragraphs.

SDP (Stereo Data Protocol)

A file which implements this protocol is a binary file containing a couple of images, a first approximation of the mean homography between the images and the ortho-rectification of the same images. The structure is defined in the following order:

Order	Definitions	Image	Symbol	Format Type	Number of data
1	N of rows of the image	LEFT	HL	INT	1
2	N of columns of the image	LEFT	WL	INT	1
3	Image (RASTER)	LEFT		FLOATS	HLxWL
4	N of rows of the image	RIGHT	HR	INT	1
5	N of columns of the image	RIGHT	WR	INT	1
6	Image (RASTER)	RIGHT		FLOATS	HRxWR
7	Homography between the images		OM	FLOATS	9
8	N of rows of the image rectified by HO	LEFT	HoR	INT	1
9	N of columns of the image rectified by HO	LEFT	WoR	INT	1
10	Image (RASTER) rectified by HO	RIGHT		FLOATS	HoRxWoR
11	N of rows of the image rectified by OM	RIGHT	HoR	INT	1
12	N of columns of the image rectified by OM	RIGHT	WoR	INT	1
13	Image (RASTER) rectified by OM	RIGHT		FLOATS	HoRxWoR

Although in the case of STC a lot of this parameters could be omitted, the protocol guarantees the use of all the different kinds of images (even if not structured by the defined output of the instrument) used in test phase of the software and of the algorithm. Future work will be the simplification of the protocol when the algorithm will demonstrate its robustness, so accelerating the reading and writing procedure of the files.

EMP (Evolving Model Protocol)

EMP is a protocol to describe in a binary file the momentary definition of a particular force. As an example at the N^{th} cycle of the algorithm the software can save: a file describing the Internal Forces, another describing the External Forces, and a third one containing the possible warnings. All these files implement the EMP.

More generally, an EMP file is a binary file containing the local time description of an information map.

Considering that normally all the forces have two different components, the structure is defined in the following order:

Order	Definitions	Symbol	Format Type	Number of data
1	N of rows of the information	H	INT	1
2	N of columns of the information	W	INT	1
3	Information Rows component (RASTER)		FLOATS	HLxWL
4	Information Columns component (RASTER)		FLOATS	HLxWL

Although in the case of STC a lot of this parameters could be omitted the protocol guarantees the use of all the different kind of images (even if not structured by the defined output of the instrument) used in test phase of the software and of the algorithm. Future work will be the simplification of the protocol when the algorithm will demonstrate its robustness accelerating the reading and writing procedure of the files.

5.4.2 System architecture

This section includes a description of the decomposition of the software for the purpose of realizing a design modularization. This description is given in the form of an OMT-style object diagram, in which the classes have been partitioned into 3 main layers:

- ***GUI-I2P*** *Graphical User Interface (Images to Project):* a graphical interface to generate the project and make a first estimation of the limits of the disparity map.
- ***SIEM-DLL*** *Stereo Image Evolving Model (Dynamic Link Library):* the DLL representing the effective snake algorithm.
- ***GUI-D2M*** *Graphical User Interface (Disparity to Measurements*): the graphical interface used to analyze results of the algorithm and measurements.

Another layer has to be added as future work:

- **SIEM-SCS** *Stereo Image Evolving Model (Self Calibration System):* the code for the effective self-calibration of the stereo-system.

A complete scheme of the layer interface is shown in **Figure 10**.

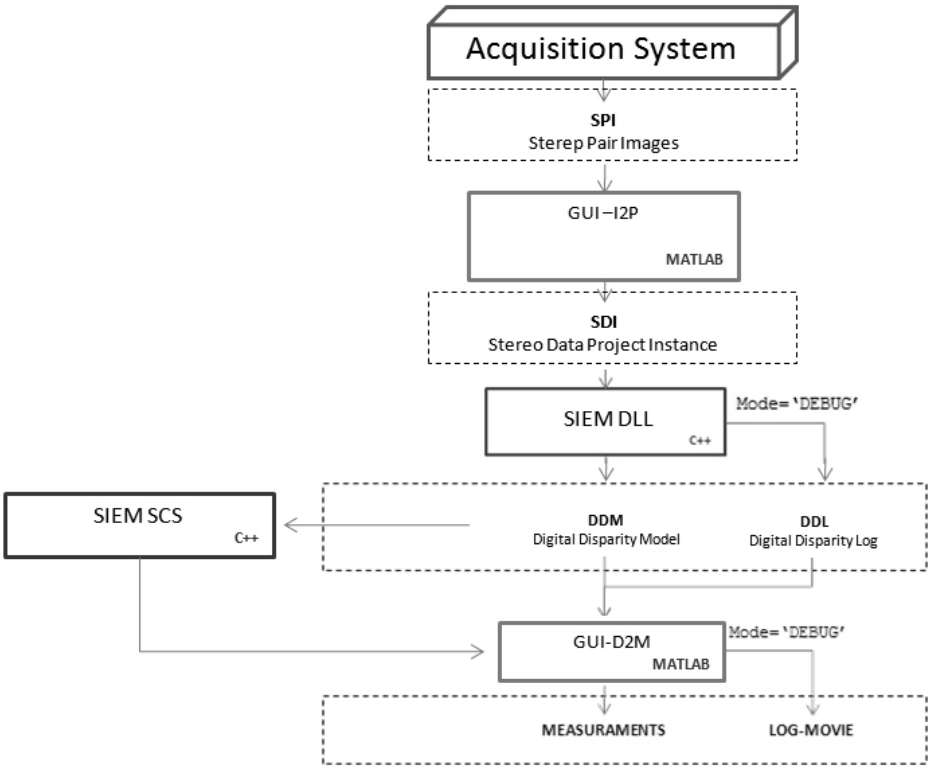

Figure 10 *Complete scheme of the layer considered in the software design.*

All the layers will be explained in detail in the following paragraphs. This partition has been chosen to link together classes with similar goals, and to keep the interfaces between the different components as simple as possible.

GUI-I2P layer

As shown in Figure 11 the GUI-I2P *Graphical User Interface (Images to Project)* layer includes the definition of all the User interface structures, as explained in Section 5.4.

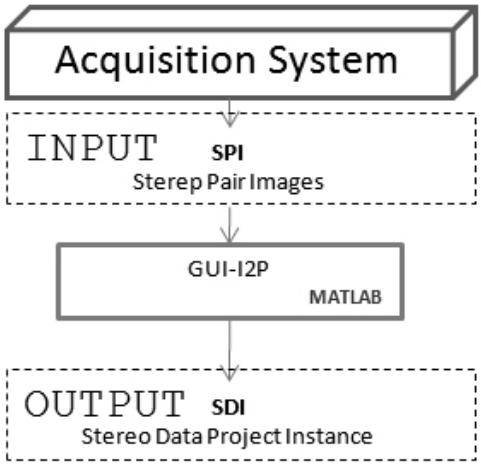

Figure 11 *GUI-I2P pipeline architecture. The Matlab software extracts the Stereo Data Project Instance from the input stereo pair images. The obtained result contains the images and the preliminary analysis of the geometry of the system.*

This includes all the pre-analysis tools for the ortho-images generation by means of a statistical analysis of the initial disparity map shape. Stereo image pairs acquired by STC, or by a different acquisition system, represent the input of the layer; their analysis brings to the definition of a SDI (Stereo Data Project Instance) a compact structured MAT[8] file following the above mentioned SDP (Stereo Data Protocol) protocol.

More in detail (see Figure 12), this layer makes a first statistical evaluation of the homography between the two images considering a limited number of points homogenously distributed on the images. In so doing, the boundaries of the disparity map are evaluated defining the memory zone for the hypercube used for the similarity function. Using this information, the SDI is generated following the SDP Stereo Data Protocol.

[8]Binary data container format used by MATLAB; may include arrays, variables, functions, and other types of data.

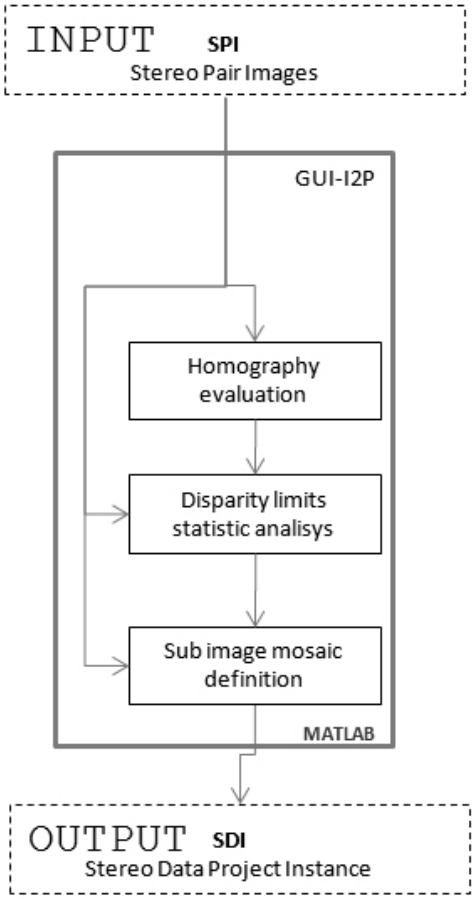

Figure 12 *Detailed scheme of the Graphical User Interface used to generate the Stereo Data Project.*

Since these boundaries generally occupies more memory than the usual capacity of a standard computer, the images are divided in sub-images according to the homography and different projects are generated.

SIEM-DLL layer

The *Stereo Image Evolving Model (Dynamic Link Library)* layer represents the kernel of the algorithm. Developed in C++, the SIEM-DLL layer evolves the project defined by the previous layers and saved in an SDI file (see Figure 13). It present a so called DEBUG mode more slow but efficient for forces analysis.

As result, it generates either a multiple or a single dataset of files representing the final reached evolution of the disparity map. or, used in DEBUG mode, the entire set of time-stepped images of the different components

of the forces, the time-local Kinetic energy, warnings detected and other parameters used for the log-analysis of all the algorithm pipeline.

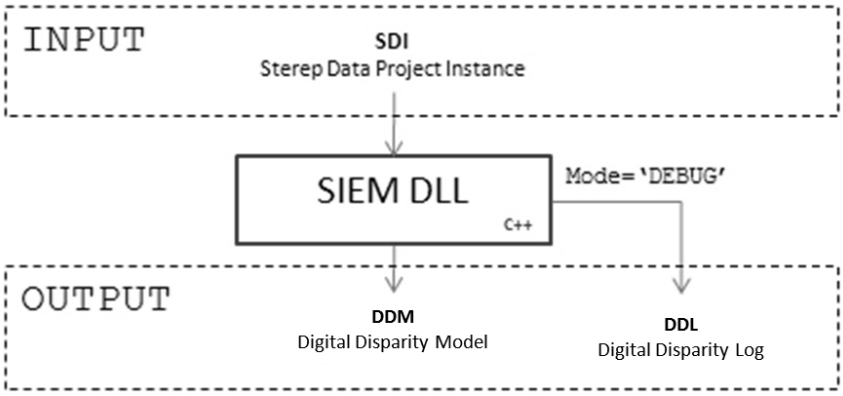

Figure 13 *SIEM-DLL architecture. The C++ DLL provides the analysis of the Stereo Data Project Instance giving the digital disparity model and the Log file as output.*

The principal function of SIEM-DLL is to guarantee the traceability of the evolution of the snakes and of the forces. This allows to detect possible wrong hypotheses on the definition of the force-models and to maintain the possibility to extend the number of used forces without losing the possibility of controlling their interaction.

The DDL Digital Disparity Log files, as explained in protocols section, are just data in binary format. This choice derives from the need of speeding up the model evolution: in fact, the latter is somehow limited by the complexity of the algorithm, and is presently the cause of the rather long time needed for processing the images.

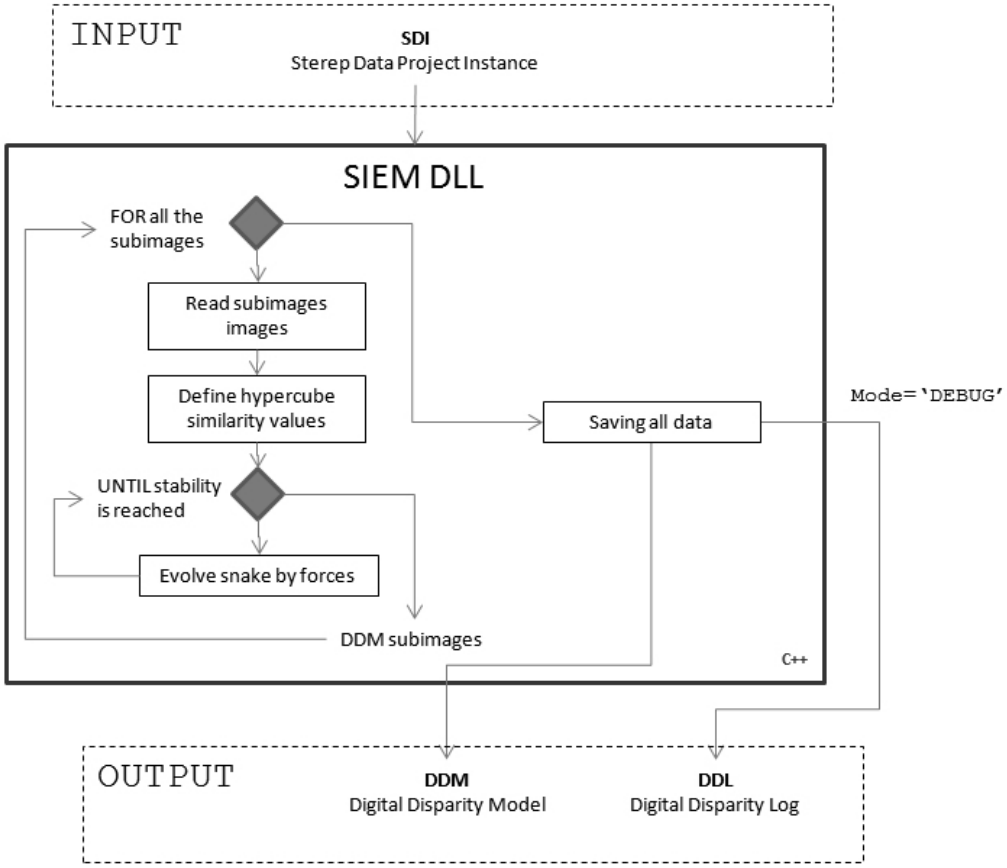

Figure 14 *The SIEM-DLL layer scheme*.

Figure 14 shows the hypercube for the similarity function defined for all the sub-images generated by previous layers. The iterative cycles for the evolution of the snakes are performed until the stability is reached. At the end of this process, a Digital Disparity Model for the considered sub-images is obtained and the process can continue until all the couples of sub-images are analyzed.

GUI-D2M layer

Graphical User Interface (*Disparity to Measurements*) is the user analysis interface. The layer, developed in MATLAB, reads and shows different outputs by SIEM interface to be used to check the reconstruction. The layer includes also some methods for the planetary surface analysis and the procedure for the generation of AVI (Indeo 5 Codec) movies for an optimal debug analysis of the model evolution.

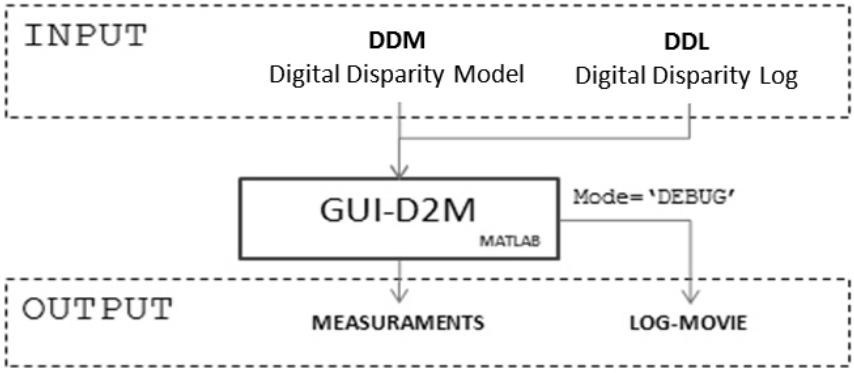

Figure 15 *GUI-D2M architecture.*

On one hand, this layer represents the graphical interface for the measurement of the 3D model; on the other, it can be considered as the block which transforms the DDL (Digital Disparity Log) binary files in more readable objects as images or movies.

As shown in **Errore. L'origine riferimento non è stata trovata.** the GUI-D2M Graphical Interface permits to analyze the results of the reconstruction in a wider mode. Different tool palettes are present:

- **Data palette** (Left-Button on the Figure 16): includes 5 different kinds of data to be shown, as follows:
    - *W. [warnings] (shows all the warnings)*
    - *I. [internal] (shows both coordinates of the internal forces)*
    - *E. [external] (shows both coordinates of the external forces)*
    - *V. [velocity] (shows both coordinates of the velocity of the snake)*
    - *D. [disparity] (shows both coordinates of the disparity map)*

- **Tool palette** (Left-Top on the Figure 16): includes 5 different tools for the images and data navigation, as follows:

    - *PAN (permits the user to pan the data dragging the mouse)*
    - *ZOOM (permits the user to zoom the data by clicking the mouse)*
    - *TURN (permits the user to rotate the data by dragging the mouse)*
    - *DIST (permits the user to measure different distances by adding new rulers)*
    - *CLEAR (clears all rulers defined by DIST).*

- **File palette** (Top-Right in the Figure 16): includes 7 different procedures. In order:

    - *Change project (permits the user to read existent projects)*
    - *Show separate (permits the user to read the output calibration file and shows the different sub-images and tie-points used to generate the project)*
    - *Movie (read all the data and generate a movie of the evolution of the snake)*
    - *NN [i.e. 102] (permits to choose the number of cycle to be shown)*
    - *New Project (permits to create a new project)*
    - *[<][>] (permits to choose the number of cycles to be shown cycle by cycle)*

- **Bool palette** (Right-Down in the Figure 16): includes 6 different Boolean choices for the visualization of the data. In order:

    - *Plot Div (permits the user to see on the images the sub-image division)*
    - *Contour (visualize the disparity map or other data as integer values ignoring the sub-pixel evaluation)*
    - *Cutter (remove homographic effect to have a better chromatic mapping)*
    - *SURF (show the data as a surface instead of images)*
    - *Composed (show the mosaicking of the sub-images instead of the stereo-images).*
    - *Invert (invert chromatic mapping)*

All commands are completely self-understanding.

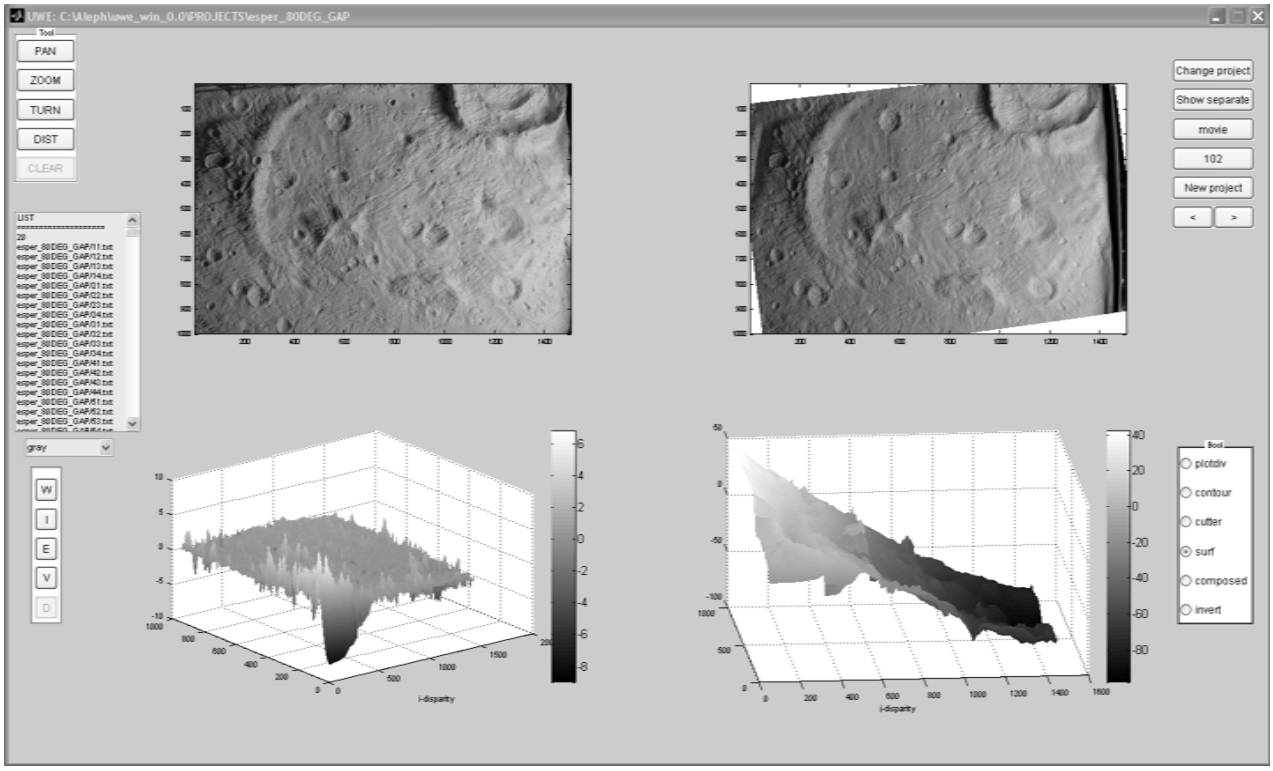

Figure 16 *Screenshot of the graphical interface.*

Other possible modalities of the interface are shown in Figure 16 and Figure 17. Note that on the images it is possible see the different sub-images taken in consideration.

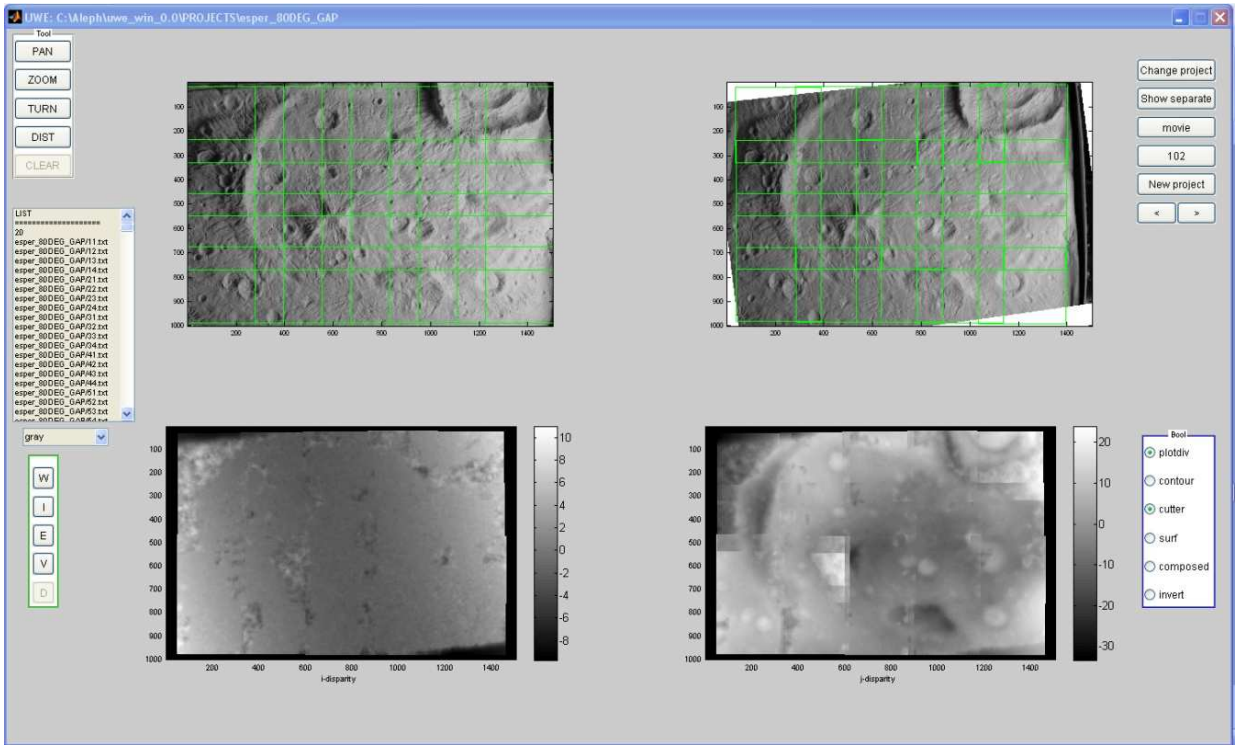

Figure 17 *Screenshot of the graphical interface.*

Component description

Table 1 reports the main characteristics of the two components:

- ***GUI_SIEM.m*:** visualization MATLAB user interface, implementing *GUI-I2P* and *GUI-D2M*
- ***Siem.dll***: algorithm pipeline, implementing the remaining blocks of the structure

	GUI_SIEM.m	SIEM.dll
Type	Starting script.	C++ DLL integrated.
Purpose	Implementing the design block I2P (from Images to Project) and D2M (from Disparity to Measurement)	It develops the stereo snaked based algorithm and supports the SCS (Stereo Calibration System)
Function	Create, Read and Measure different stereo-projects.	Generate a DDM.
Interfaces	Start interactively, by a command line, when the Operator begins the process of creating a project or wants to read an old project and apply any kind of measurement or visualize the effective step by step evolution of the snakes.	Actually starting by Operator choice, it will be integrated in the GUI_SIEM interface

Table 1 *Table of the principal characteristic of the two execute files responsible of the entire structure of the procedure.*

References

[ACK84] Ackermann, F. 1984. **Digital image correlation: performance and potential application in photogrammetry**.*The Photogrammetric Record. Volume 11 (64), pp. 429-439*

[ALB05] Albertz Joerg et al., 2005. **HRSC on Mars Express – Photogrammetric and Cartographic Research**. *Photogrammetric Engineering &Remote Sensing, Vol. 71, No. 10, October 2005, pp. 1153–1166.*

[BAL91] Baltsavias, E.P., 1991, **Multiphoto geometrically constrained matching**. PhD dissertation, *Report No. 49, Institute of Geodesy and Photogrammetry, ETH Zurich, Switzerland.*

[CRE09] Cremonese G. et al., The **stereo camera on the BepiColombo ESA/JAXA mission: a novel approach**, 2009*, Advances in Geosciences, 15, 305-322.*

[DAD10] V. Da Deppo, G. Naletto, G. Cremonese, L. Calamai, "**Optical design of the single-detector planetary stereo camera for the BepiColombo European Space Agency mission to Mercury***", Appl. Opt.* ***49****, pp. 2910-2919 (2010).*

[DEC00] DeCarlo D., Metaxas D., 2000, **Optical Flow Constraints on Deformable Models with Applications to Face Tracking***, International Journal of Computer Vision, 38(2), pp. 99-127.*

[EBN88] Ebner H., and C. Heipke, 1988: **Integration of digital image matching and object surface reconstruction**, *International Archives of Photogrammetry and Remote Sensing, Congress Kyoto, Commission III, Vol. 27, Part Bll, pp.III-534-545.*

[ECK05] Eckert, S., Kellenberg, T., Itten, K., 2005. **Accuracy assessment of automatically derived digital elevation model from ASTER data in mountainous terrain**. *Int. J. Remote Sensing 26 (9), 1943–1957.*

[FLA10] Flamini,E.,2010. **SIMBIO-SYS:the Spectrometer and Imagers Integrated Observatory SYStem for BepiColomboPlanetary Orbiter**, *Plan.Space Sci.,Vol 58, Jan 2010, pp 125-143.*

[FOR84] Förstner W., 1984. **A feature based correspondence algorithm for image matching**.*International Archives of Photogrammetry and Remote Sensing, vol 26/3, Rovaniemi, 1986,*

[GHA02] Ghaffari R.,2002 **Snake Contours in Three-Dimensions From Colour Stereo Image Pair**, *Ph.D. Thesis, Sharif University of Technology, Tehran Iran*

[GRE07] Greminger, M.A. et al., 2007. **A Deformable Object Tracking Algorithm Based on the Boundary Element Method that is Robust to Occlusions and Spurious Edges**, *International Journal of Computer Vision*, *Volume 78, Number 1 / June, 2008,pp 29-45*

[GRU85] Grün, *A.,* 1985. **Adaptive least squares correlation: a powerful image matching technique**. *South African Journal of Photog., Remote Sensing and Cartography, 14(3), pp. 175-187.*

[GRU88] Grün, *A.,* and Baltsavias, E. 1988. **Geometrically constrained multiphoto matching**, *Photogrammetric Engineering &Remote Sensing, Vol. 54, No.5, pp. 633-64l.*

[GWI09] Gwinner, K., F. Scholten, M. Spiegel, R. Schmidt, C. Heipke, J. Oberst, R. Jaumann, G. Neukum, **Derivation and validation of high resolution digital terrain models from Mars Express HRSC data**, *Photogrammetric Engineering &Remote Sensing, 75(9), pp. 1127-1142, 2009.*

[HEI92] Heipke, C., 1992. ***A Global Approach for Least-Squares Image Matching and Surface Reconstruction in Object Space.*** *Photogrammetric Engineering &Remote Sensing, Vol. 58, No. 3, pp. 317-323.*

[HEIP07] Heipke, C., J. Oberst, J. Albertz, M. Attwenger, P. Dorninger, E. Dorrer, M. Ewe, S. Gehrke, K. Gwinner, H. Hirschmüller, J. R. Kim, R. L. Kirk, H. Mayer, J.-P. Muller, R. Rengarajan, M. Rentsch, R. Schmidt, F.Scholten, J. Shan, M. Spiegel, M. Wählisch, G. Neukum, and the HRSC Co-Investigator Team, **Evaluatingplanetary digital terrain models —The HRSC DTM** test, *Planetary and Space Science, Vol. 55, Is-sue 14, pp. 2173-2191, 2007.*

[HEL88] Helava, U. V., 1988. **Object-space least-squares correlation,** *Photogrammetric Engineering &Remote Sensing, Vol. 54, No. 6, pp. 711-714.*

[HIR03] Hirano A., Welch R., Lang H., 2003, **Mapping from ASTER stereo image data: DEM validation and accuracy assessment**, *ISPRS Journal of Photogrammetry & Remote Sensing, Vol. 57 , No 5 pp. 356–370.*

[HOR81] Horn, B.K.P. and Schunck B.G., 1981. **Determining Optical Flow**, *Artificial Intelligence Vol.* 17 (1981) *pp.185-203.*

[KAS88] Kass, M., Witkin A, and Terzopoulos D. 1988 **Snakes: Active contour models**. *International Journal of Computer Vision,1(4):321–331*

[KIM06] Kim, S.H., et al. 2006, **Object Segmentation Algorithm Using Snakes in Stereo Images**, *Optical Engineering, vol. 45, no. 3, pp. 037005, Mar. 2006.*

[KIR08] Kirk, R.L., E. Howington-Kraus, M. R. Rosiek, J. A. Anderson, B. A. Archinal, K. J. Becker, D. A. Cook, D. M.Galuszka, P. E. Geissler, T. M. Hare, I. M. Holmberg, L. P. Keszthelyi, B. L. Redding, W. A. Delamere, D.Gallagher, J. D. Chapel, E. M. Eliason, R. King, and A. S. McEwen, 2008. **Ultrahigh resolution topographic mapping of Mars with MRO HiRISE stereo images: Meter-scale slopes of candidate** *Phoenix landing sites. J. GeophysicalResearch, 113, E00A24, doi: 10.1029/2007JE003000, 2008.*

[KRU97] Krupnik, A., and Schenk, T., 1997. **Experiments with matching in the object space for aerotriangulation.** *ISPRS Journal of Photogrammetry and Remote Sensing, Vol. 52, Issue 4, August 1997, pp.160-168.*

[KRY91] Krystek, P., 1991. **Fully automatic measurement of digital elevation models with MATCH-T, Proc. 43th Photogrammetric Week**, *Schriftenreihe des Institus für Photogrammetrie der Universität Stuttgart, Heft 15*

[LEM08] Lemaire, C., 2008. **Aspects of the DSM production with high resolution images**, *International Archives of Photogrammetry and Remote Sensing, Congress Beijing, Commission IV, Vol. XXXVII, Part B4, pp.1143-1146.*

[LEW95] Lewis, J. P., 1995. **"Fast Template Matching", Proc. Vision Interface 95, Canadian Image Processing and Pattern Recognition Society**, *Quebec City, Canada, May 15-19*, 1995,p. 120-123.

[MAS08] Massironi, M. et al. 2008, Simulations using terrestrial geological analogues to assess interpretability of potential geological features of the Hermean surface restituted by the STereo imaging Camera of the SIMBIOSYS package(BepiColombo mission),*Planetary and Space Science*, 56 (2008) 1079–1092.

[MCE07] McEwen, A.S.,Eliason, E. M., Bergstrom, J. W, Bridges, N. T.,Hansen, C.J.,Delamere, W. A., Grant, J. A., Gulick, V.C., Herkenhoff, K. E.,Keszthelyi, L., Kirk, R.L., Mellon, M.T., Squyres, S.W., Thomas, N., Weitz, C. M. **Mars Reconnaissance Orbiter's High Resolution Imaging Science Experiment (HiRISE)**.*Journal of geophysical research, vol. 112, e05s02, pp.1-40. doi:10.1029/2005je002605, 2007*

[MCL96] McInerney, T. and Terzopoulos D.,1996. **Deformable Models in Medical Image Analysis:** A Survey, *Medical Image Analysis, 1(2):91–108, 1996.*

[SCH00] Schmid, C, Mohr, R., Bauckhage, C., 2000. **Evaluation of interest point detectors**. *International Journal of Computer Vision*: 37(2*): 151-172.*

[NEU04] Neukum, G., R. Jaumann, and **the HRSC Co-Investigator Team, 2004. HRSC: The High Resolution Stereo Camera of Mars *Express**, ESA Special Publications SP-1240.*

[SCH05] Scholten, F. et al., 2005. **Mars Express HRSC Data Processing – Methods and 0perational Aspects.** *Photogrammetric Engineering &Remote Sensing, Vol. 71, No. 10, October 2005, pp. 1143–1152.*

[SER97] Sergey, F., 1997. Exploring three-dimensional implicit wavefield extrapolation with the helix transform,***URL:http://sepwww.stanford.edu/public/docs/sep95//sergey2/paper_html/node12.htm****l*

[TER97] TerjeTotland (1997). 5.2.7 **Object Modeling Technique (OMT)** Thesis, Norwegian University of Science and Technology (NTNU), Trondheim.

[TOU02] Toutin, T., 2002. Three-dimensional topographic mapping with ASTER stereo data in rugged topography. *IEEE Trans. Geosci. Remote Sensing 40, 2241–2247.*

[WRO87] Wrobel, B., 1987. **Facets stereo vision (FAST Vision) - A new approach to computer stereo vision and to digital photogrammetry, Interlaken***, Proc. Fast Processing of Photogrammetric Data, pp. 231-258.*

Chapter 6

Test data and Results

Contents

Introduction

The theory which supports the new method for the 3D reconstruction of Mercury using images from STC has been previously discussed (see Chapter 3). The same was done for the implementation of the so called SIEM algorithm. In this chapter we are presenting some applications of the algorithm.

On one side the tests have to be read as effective 3D reconstruction for metronomic measurement; on the other side, these tests allow to show the evolution of the algorithm itself. For this scope, the structure of the chapter is presented as a chronological history of the tests, showing to the reader what have been the choices that brought to the actual state of the algorithm and of the software.

Three principal tests will be described. The first is a comparison of the 3D reconstruction performance of SIEM with those obtained by means of the DLR-Match software; for this test, the Mercury images obtained by the Messenger satellite during its first flyby have been used. The second test is the analysis of the 3D reconstruction performance starting with synthetic images as obtained from a known object. Finally, the third is a test on the effect of the wavelet based image compression on the stereoscopic results; for this test, a comparison with a Least Square Matching based algorithm has been realized.

The obtained results can be of considerable interest for the development of a complete self automatic procedure for the high resolution (multi information based) stereo-reconstruction.

7.1. First Results: a brief history

The Mercury stereo images received from Messenger were processed with the snake algorithm using, to compute the similarity function, a window size as small as 3x3 pixels.

As explained in Chapter 3 an open question in snake methods is the tradeoff of the forces considered in the equation:

$$\dot{s} = \alpha \mathcal{F}_e^{(s)} + \beta \mathcal{F}_i^{(s)}$$

where α and β represent the weight of the external and internal forces.

The Messenger data shown in Figure 1 and obtained during the first flyby where used for the first simulations, with which we defined the optimal values of these parameters. The software was initially written in IDL[1] and did not allow the analysis of large images because of computational and timing problems. In this case a low "aperture" of the disparity , that is it varies of just 1-2 pixels over the whole surface, so that the reconstruction needs a really deep sub-pixel analysis which is not yet realized by the state of art software, did not granted a good reconstruction of the surface but permitted to understand the real effect of the two parameters.

In Figure 1 the effect of the two terms is presented. Horizontally there is the increment from left to right of β parameter responsible of internal forces (the right side panels of the figure are more smoothed because internal forces are more strong). Vertically there is the increment from up to down of the α parameter responsible of external forces (the down side of the figure is more affected by stereo mismatches).

In substance more strong are the stereo forces more there is the possibility of wrong mismatches which have to be balanced by the internal forces which maintain the continuity.

[1] **IDL**, the **Interactive Data Language**, is a programming language used for data analysis. It is popular in particular areas of science, such as astronomy and medical imaging.

(a)

(b)

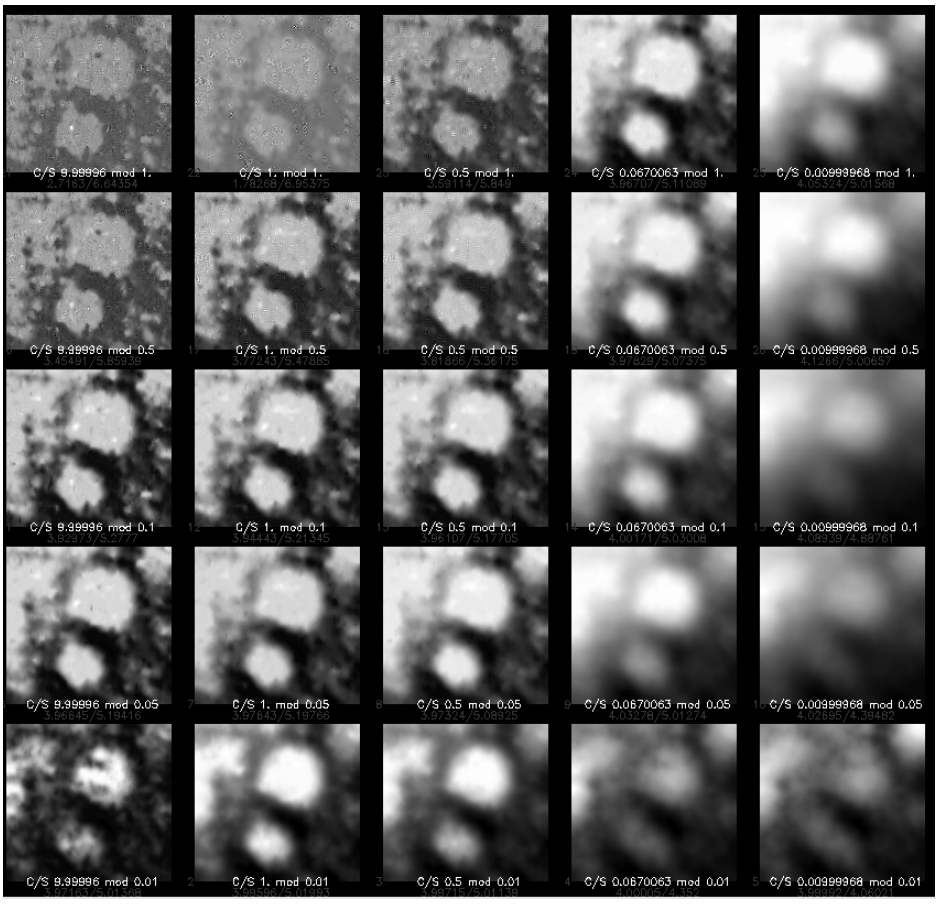

(c)

Figure 1 Couple of images (a) and (b) extracted by the first Messenger flyby; (c) small pictures showing the result reconstruction obtained using the snake method for different values of the weight parameters.

The same images have been used after a software optimization turning to enlarge image dimensions which can be analyzed.

In this case, a rather poor reconstruction has been obtained, with an overlapped strange wave deformation (Figure 2): this was a clear indication that the balancing of the weight parameters had still to be obtained.

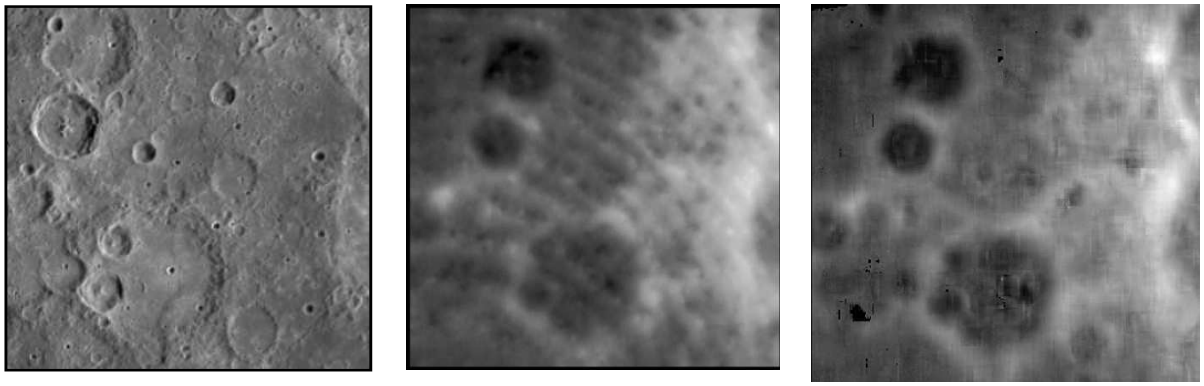

(a) (b) (c)

Figure 2 *First applications of the SIEM algorithm to MESSENGER data. (a) one of the two used images. (b) SIEM reconstruction results, where a wave overlaying pattern is clearly visible. (c) DLR-Match reconstruction results.*

Trying to explain this wave effect, we considered a possible error in the definition of the force boundaries (see Chapter 6); however the problem appeared to be related to the particularity of the images, which had low spatial resolution and minimal disparity aperture. At the end it was decided to use different images as test bench. Since other useful images of Mercury were not available, we selected more contrasted and easy to procure stereo images from Arizona, acquired by ASTER[2]. One of the images of the considered couple is shown in Figure 3(a). After some tests to define the better weight parameters the reached result (see Figure 3 (b)) was by far more performing than that obtained by the robust algorithm of DLR-Institute, showing many more details. All the reconstructions were made with a matching window value of 5 pixels.

[2]**ASTER** (**Advanced Spaceborne Thermal Emission and Reflection Radiometer**) is a NASA/Japan instrument which is one of five remote sensory devices on board the Terra satellite launched into Earth orbit by NASA in 1999. The instrument has been collecting superficial data since February 2000.

Classic DLR pipeline normally use larger dimensions (11-15 pixels) to reach a good reconstruction and the results obtainable by DLR-Match2 are surely more valid that the one of the actual state of SIEM, but the demonstration that with a so little information a snake based algorithm could reach so good results encouraged the evolution of the work.

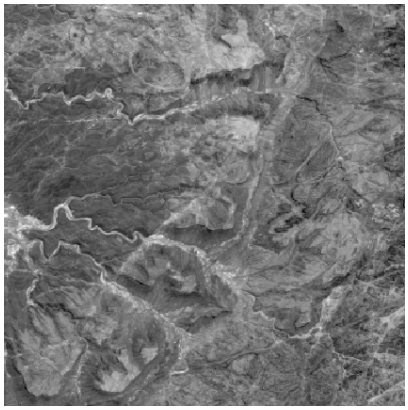

(a)

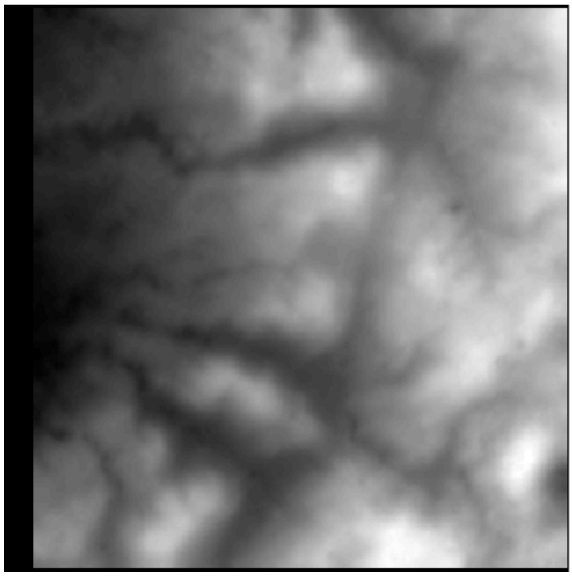

(b)

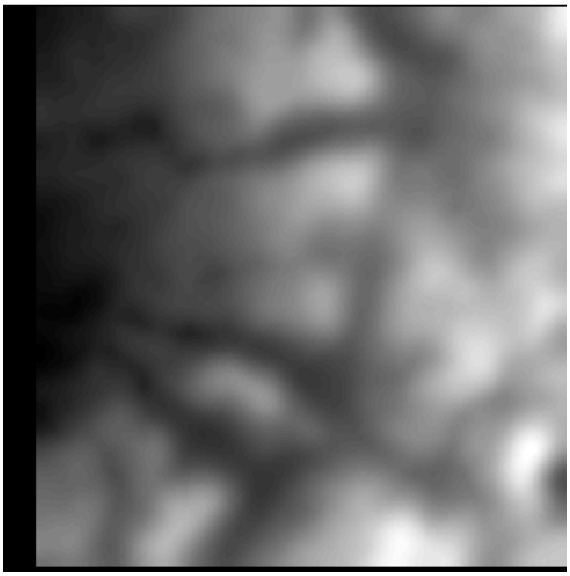

(c)

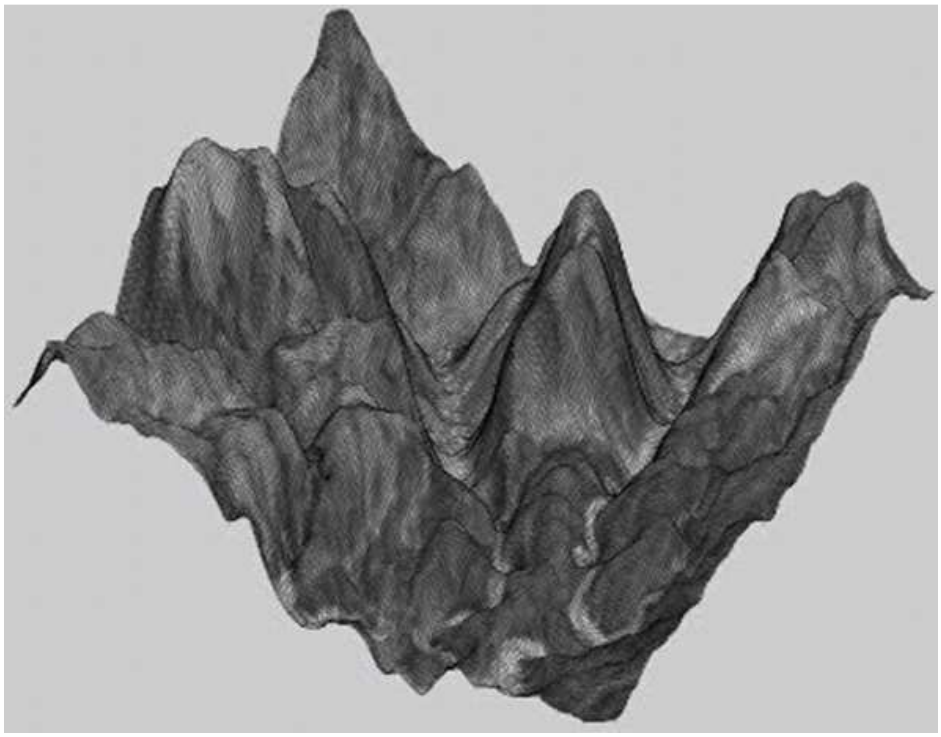

(d)

Figure 3 *(a) ASTER image showing a small portion of the Arizona State. Relative disparity map reconstructed with SIEM algorithm (b) and with DLR-Match2 (c); in both case a minimal matching window size of 5 pixels has been used. In (d) the surfing of the relative disparity map shown in (b).*

7.2. Test data with synthetic images

Tests on the performance of the proposed algorithm have been performed on synthetic images derived from 3D models of geological features relevant to planetary science, in the imaging geometry of the STC of BepiColombo.

All the images were produced remembering that:

- the images of the Mercury surface will be acquired from a satellite orbiting around the planet with its reference axis (nadir) always oriented towards the center of the planet
- the STC has been designed with two fixed optical sub-channels, oriented at ±20° with respect to nadir [CRE09]
- each sub-channel covers a field of view of 5.3° cross track;
- no occlusions should arise for slopes inclined less than 74°.

As described in Chapter 3 to simplify the problem of the weight we have defined the angle θ (where $\tan\theta = \frac{\alpha}{\beta}$) to study the influence of the two parameters.

In the following, the results for three datasets, respectively named C1, C2 and D1, are shown.

Each dataset is made of the image pair, the interior and exterior orientation data and the reference DEM. The first represents a fully synthetic crater site (see Figure 4.), generated in 3DStudioMax™; the global terrain trend is gently undulating but with a net of narrow and steep ridges a few meter high; the texture is generally good, there are also several areas with undulating terrain but low variance of the grey values, to simulate lack of image features. The second and third datasets have been generated from photorealistic 3D models of two geological Earth features: the RoterKamm crater (Namibia) (see Figure 5) and a volcanic endogenous dome from Meseta de Somuncura (Argentina) (see Figure 6). These two sites were selected in a previous study about the potentialities of the BepiColombo STC in resolving Mercury surface details for geological interpretation [MAS08].The 3D photorealistic models were produced using ASTER images from the Terra Earth Observation Satellite ([YAM10],[ABR00]). Using the DTM extraction module of IDL-ENVI (http://www.ittvis.com) a 30 m resolution DTM of each feature has been generated, with an estimated accuracy of 15 m, from the 15 m ground resolution images of ASTER ([TOU02]; [ECK05]). Notice that, as can be better seen in Figure 4 and 5 (left), the DTM generated by ENVI is very rough. Each model was texture-mapped in 3DStudioMax™ with the orthorectified image produced with ENVI.

Finally, the synthetic STC images of the three sites were generated in 3DStudioMax™: the textured 3D model of the craters C1 and C2 and of the volcanic dome D1 were positioned at the hermean equator and imaged by the two STC sub-channels from two locations symmetric with respect to the orbit periherm. The image scale is about 1:4,800,000, the base to height ratio is 0.86 and the ground resolution is about 50 m; with an image accuracy of 1 pixel = 10 µm and error-free interior and exterior orientation parameters this results in a theoretical accuracy of point determination of about 35 m in longitude and latitude and about 80 m in elevation [MAS08].

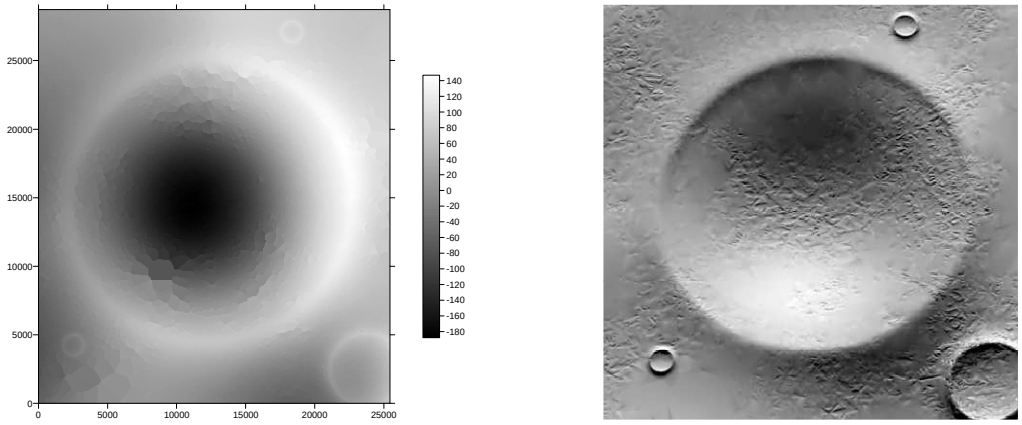

(a) (b)

Figure 4. *Dataset C1: (a) DTM pseudo-colored ; (b) synthetic image.*

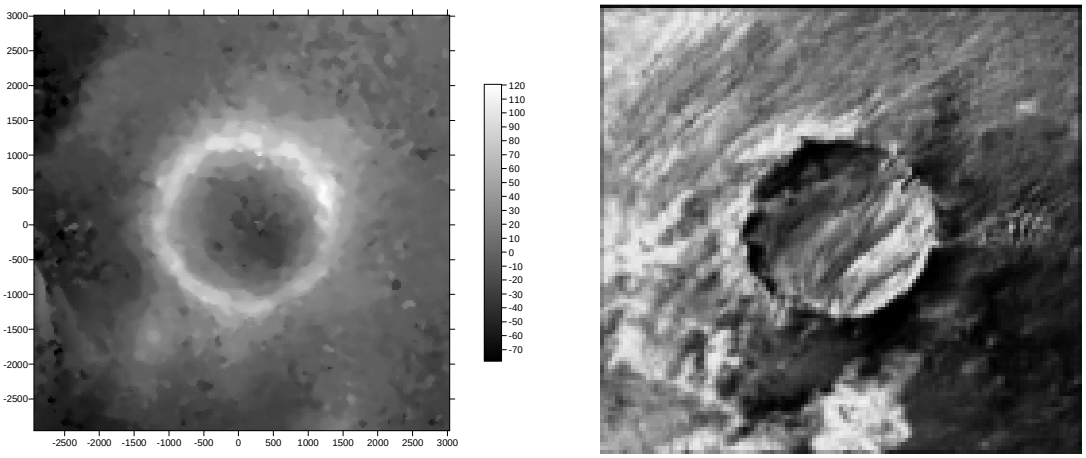

(a) (b)

Figure 5 *Dataset C2 (originally from Roter Kamm crater): (a) DTM pseudo-colored; (b) synthetic image.*

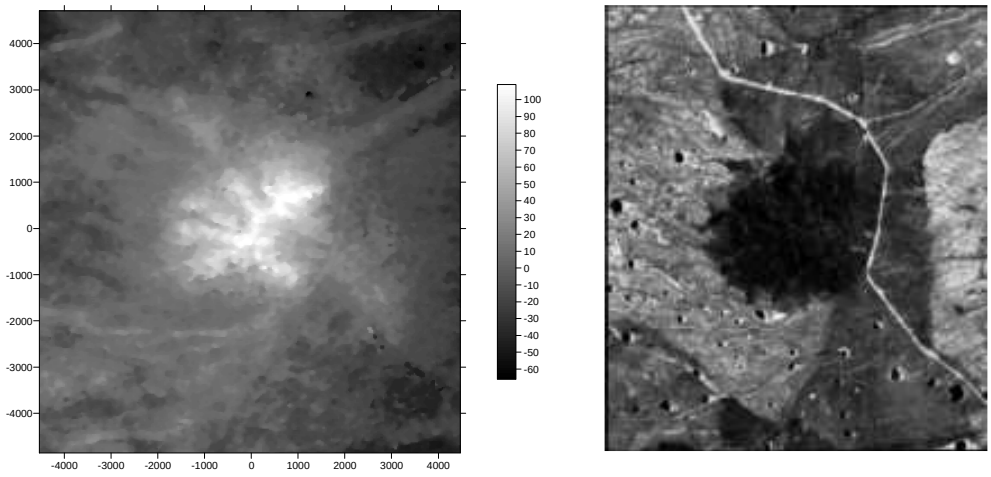

(a) (b)

Figure 6 *Dataset D1 (originally from Meseta de Somuncura): (a) DTM pseudo-colored; (b) synthetic image*

Tests were performed with θ values in the range 70°- 88°.

To assess the results of the algorithm, the final parallax field (after convergence of the *deformable surface*) and the known orientation parameters of the images were used to compute the object coordinates of each pixel in the template image of the stereo pair. The *z* coordinate of each point was then compared to the known DTM elevation at the same (*x*, *y*) location.

Table 1 shows the RMS of the difference between the original DTM of dataset C1 and the reconstructed one for different values of θ. The values are always smaller than 10 m, with a minimum of 8.3 m for $\theta = 83°$. Tables 2 and 3 show the same figures for datasets C2 and D1. The maximum value amounts to 8.1 m for the crater and to 6.5 m for the dome.

As a term of comparison, the nominal vertical accuracies presented in [MAS08] for the reconstruction of C2 and D1 using the LSM algorithm are 10 m for the crater and 7 m for the dome (see [SIM11]). It should also be noted that these figures were computed using only successfully matched points with correlation coefficients larger than 0.80 (i.e. a set of reasonably "safe" points). Although obtained from synthetic images, these results show the capacity of the algorithm to match the accuracy level of the best area-based methods.

θ [°]	81	82	83	84	85	87	88
RMS [m]	8.37	8.32	8.30	8.33	8.44	9.23	9.82

Table 1. Statistics of the a*ccuracy of 3D reconstruction of C1 for different θ values.*

θ [°]	70	75	80	82.5	83.7	85
RMS [m]	8.12	7.92	7.41	7.13	7.27	7.94

Table 2. Statistics of the a*ccuracy of 3D reconstruction of C2 for different θ values*

θ [°]	70	75	80	85	86.5	87.2	88
RMS [m]	6.51	6.25	5.95	5.67	5.64	5.67	6

Table 3. Statistics of the a*ccuracy of 3D reconstruction of D1 for different θ values*

Tables 1, 2, 3 and Figure 7 show that the optimal θ value in the simulations differs case by case, with some dependence on the surface characteristics. In fact, while the dome images have a fair amount of high frequency features, the crater images mainly contain lower spatial frequencies: the external forces do not need a strong boost and the best fitting surface is obtained for smaller values of the ratio θ .

Actually the optimal θ value is chosen by quality analisys of the resulting disparity map, as in common snakes application. A strategy for the automatic estimation of this value is being investigated (see [SIM11]).

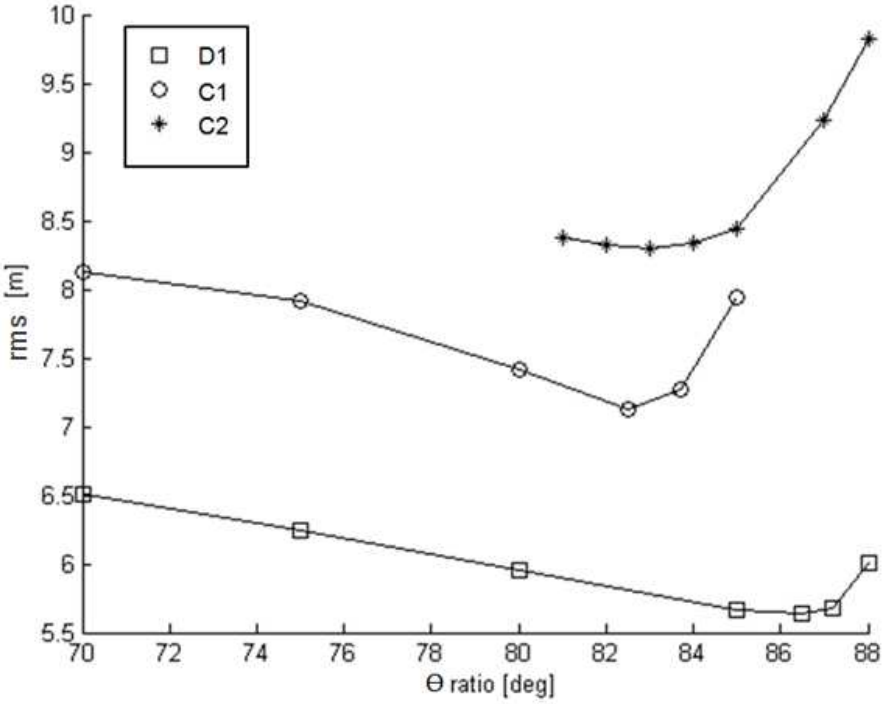

Figure 7 *Standard deviation of the differences between the true DTM and the DTM reconstructed by the snake-based algorithm. The theta parameter (see Chapter 3) represents the ratio between the magnitudes of the internal and external forces.*

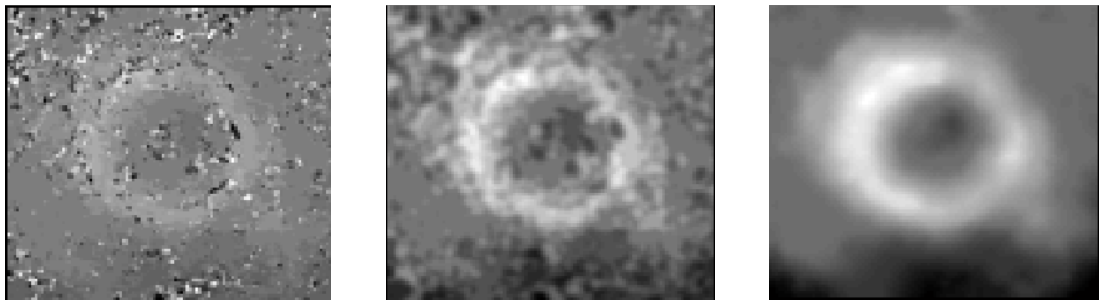

(a) *(b)* *(c)*

Figure 8 *DTM reconstruction of dataset C2 obtained with rather different ratios of internal to external forces: (a) θ =45°; (b) θ =75°; (c) θ =89°*

Figure 8 shows the DTM reconstruction for dataset C2 with very different values of the ratio θ. As pointed out earlier, the choice of the optimal value of θ is currently made by visual examination of the parallax field; in (a) the presence of positive and negative spikes in the terrain (black and white spots) suggests that the constraints are not strong enough and the solution may locally diverge; in (b) there are no spikes but the surface is clearly too rough; in (c) there is too much low-pass filtering (the constraints are too strong). The optimal value lies in this case between 80° and 85°.

Figure 9 compares the original and the reconstructed terrain representation of the three datasets in terms of contour lines, while Figure 10 compares the raster representation of the DTM with the error map.

As far as the synthetic crater C1 is concerned, the general morphology of the terrain depicted by the two sets of contour lines is very similar; the only difference is some smoothing of the contours. The corrugation of the original contours derives from the net of ridges that could not be captured by the algorithm. The correlation of the errors with the high frequency features of the DTM is more apparent in Figure 9, showing that the largest errors occur on the ridges. Notice that a more intensive use of other constrains could be the key to gain accuracy.

C1)

C2)

D1)

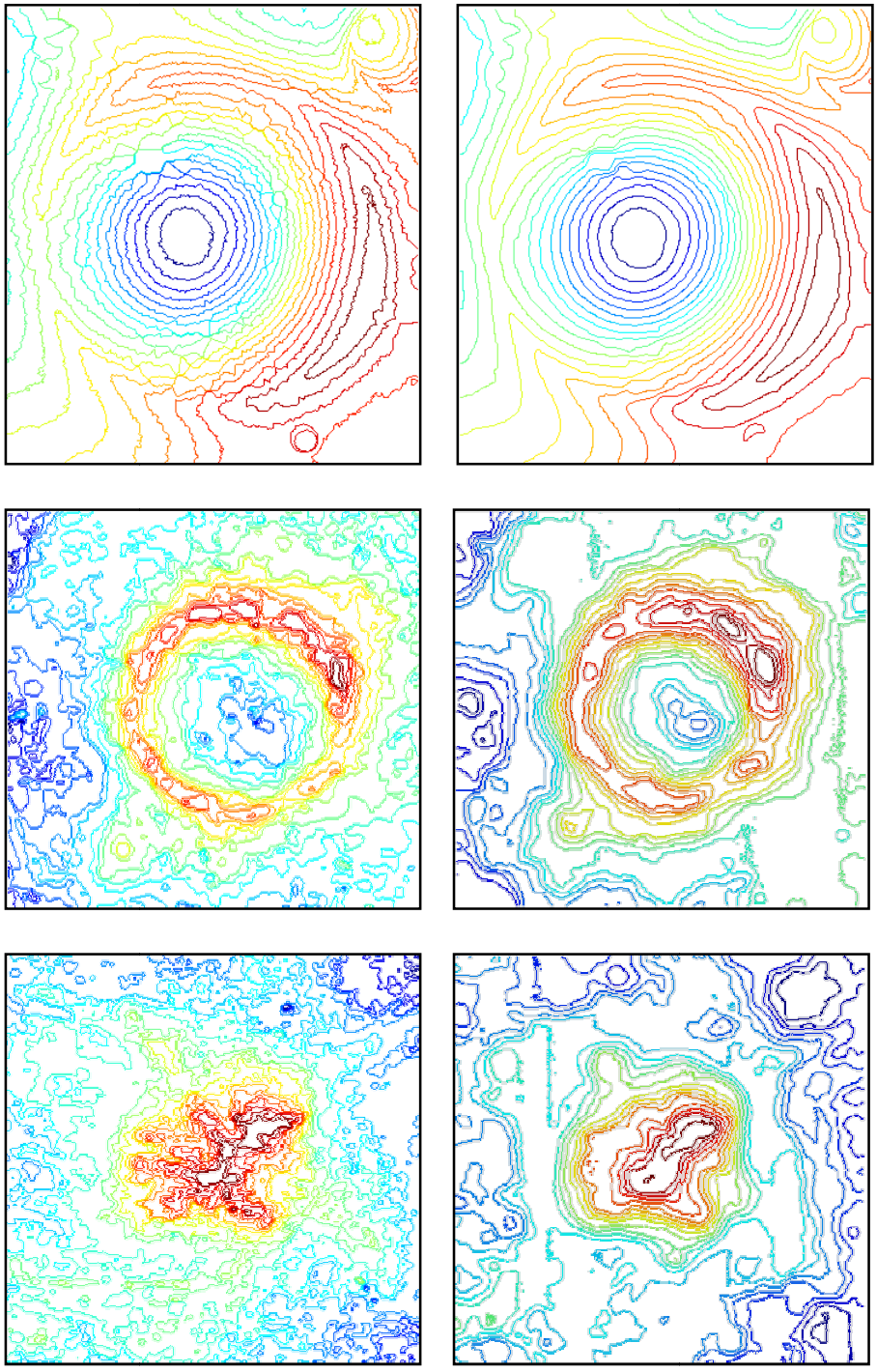

Figure 9 *Contour lines from the different datasets DTMs. Left: original; right: reconstructed.*

C1)

C2)

D1)

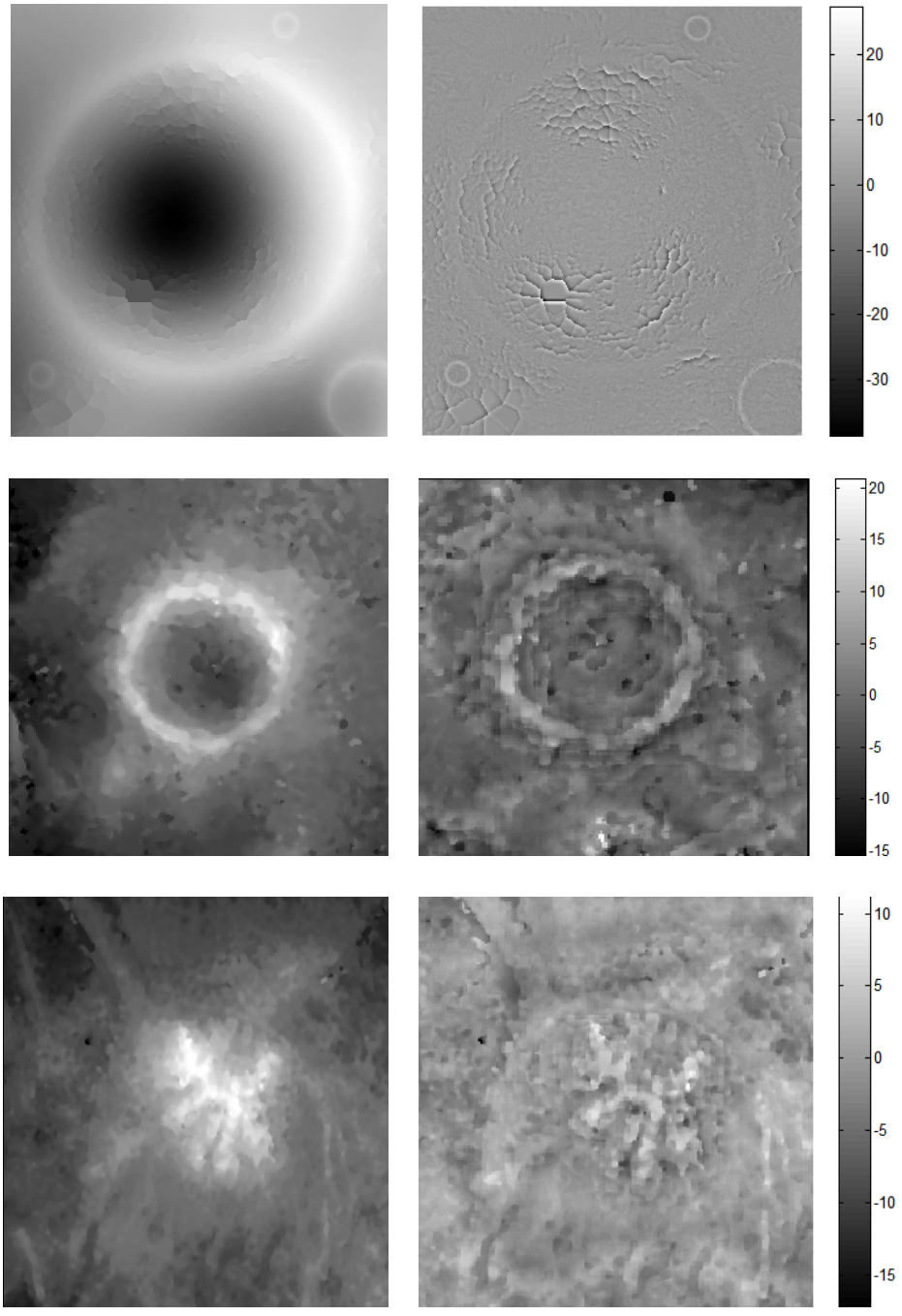

Figure 10 *Error maps (right) compared to images (left), with color coded error (scale in m). The reconstruction error is clearly correlated to surface topography.*

As far as dataset C2 and D1 are concerned, the low pass (smoothing) effect of the reconstructed DTM is also apparent and is still correlated with the high frequency features of the terrain.

7.3. Error in compression

As explained in [SIM11] SIMBIOSYS will use a compression algorithm based on wavelets and already adopted for some instruments on board the Mars Express mission. The compression factors will depend on the volume of the data to download, on the available data rate, and on the efficiency of the applied compression algorithm. The organization of the SIMBIOBSYS Main Electronics and software will permit to use different compression factor for the images.

The correspondence between the value of the compression factor used by the available algorithm and the actual number of bit/pixel in the compressed images is given in the following table:

Compression factor	bit/pixels
2	0.125
4	0.25
8	0.5
12	0.75
16	1
24	1.5
32	2
63	3.9375

Note that the compression factor 63 is associated to an image compression close to lossless.

To perform the tests on compression, the SIEM algorithm was compared to a different software, based on Least Square Matching (LSM) and Multiphoto Constrained Geometrically Matching (MCGM), called DenseMatcher (University of Parma)[FOR] generally used in completely different applications. The comparison shows the validity of the snake-based method until texture information is not affected by excessive compression.

In the following tables the standard deviation and the mean of the errors in reconstruction with respect to not compressed images are shown. For a better understanding of the results, the diagonal of the standard deviations is also presented in Figure 11.

σ_STD [m]	4	8	12	16	24	32	63
4	22.8	24.2	20.6	21.2	25.5	24.4	23.8
8	24.2	15.4	14.8	14.8	15.3	15.8	16.1
12	20.6	14.8	11.2	11.4	10.2	10.7	10.9
16	21.2	14.8	11.4	8.55	6.93	8.11	7.78
24	25.5	15.3	10.2	6.93	5.26	4.58	4.1
32	24.4	15.8	10.7	8.11	4.58	2.51	1.81
63	23.8	16.1	10.9	7.78	4.1	1.81	0.02

Table 1 *Standard deviation of the error in reconstruction between the DTM generated using SIEM algorithm and the same reconstruction applied to LOSSLESS images for the test image Crater C2*

σ_STD [m]	4	8	12	16	24	32	63
4	18.4	20.14	18.28	18.48	18.43	18.71	18.52
8	18.4	8.96	8.64	8.93	8.98	8.86	8.91
12	17.2	7.64	5.60	5.16	4.99	5.17	5.17
16	17.4	6.98	4.74	3.63	3.30	3.40	3.52
24	18.03	6.61	3.99	2.61	1.71	1.59	1.55

32	18.05	6.49	3.72	2.35	1.25	0.85	0.71
63	18.41	6.29	3.50	2.22	1.14	0.65	0.46

Table 2 *Standard deviation of the errors in reconstruction between the DTM generated using DenseMatcher algorithm and the same reconstruction applied to LOSSLESS images for the test image Crater C2*

MEAN [m]	4	8	12	16	24	32	63
4	1.72	9.58	10.6	14.1	16.8	15.9	14.6
8	9.58	2.12	3.56	2.96	4.46	4.77	5.42
12	10.6	3.56	1.45	0.79	2.53	2.17	1.71
16	14.1	2.96	0.79	0.69	1.69	1.76	1.5
24	16.8	4.46	2.53	1.69	1	0.99	0.67
32	15.9	4.77	2.17	1.76	0.991	0.36	0.15
63	14.6	5.42	1.71	1.5	0.668	0.15	0.03

Table 3 *Offset mean of the error in reconstruction between the DTM generated using SIEM algorithm and the same reconstruction applied to LOSSLESS images for the test image Crater C2*

MEAN [m]	4	8	12	16	24	32	63
4	-5.68	-9.90	-10.43	-11.14	-11.28	-11.63	-11.70
8	-5.49	-3.18	-4.73	-4.96	-5.00	-5.29	-5.24
12	-5.28	-2.73	-2.39	-2.69	-3.02	-3.22	-3.20
16	-5.05	-2.06	-1.26	-1.34	-1.71	-1.82	-1.82
24	-4.74	-2.05	-1.08	-0.78	-0.62	-0.57	-0.48
32	-4.99	-2.05	-1.14	-0.69	-0.44	-0.35	-0.20
63	-5.09	-1.88	-0.99	-0.54	-0.27	-0.15	-0.02

Table 4 *Offsett mean of the error in reconstruction between the DTM generated using Dense Matcher algorithm and the same reconstruction applied to LOSSLESS images for the test image Crater C2*

For a better understanding of the results the diagonal of the standard deviation is presented in Figure 11

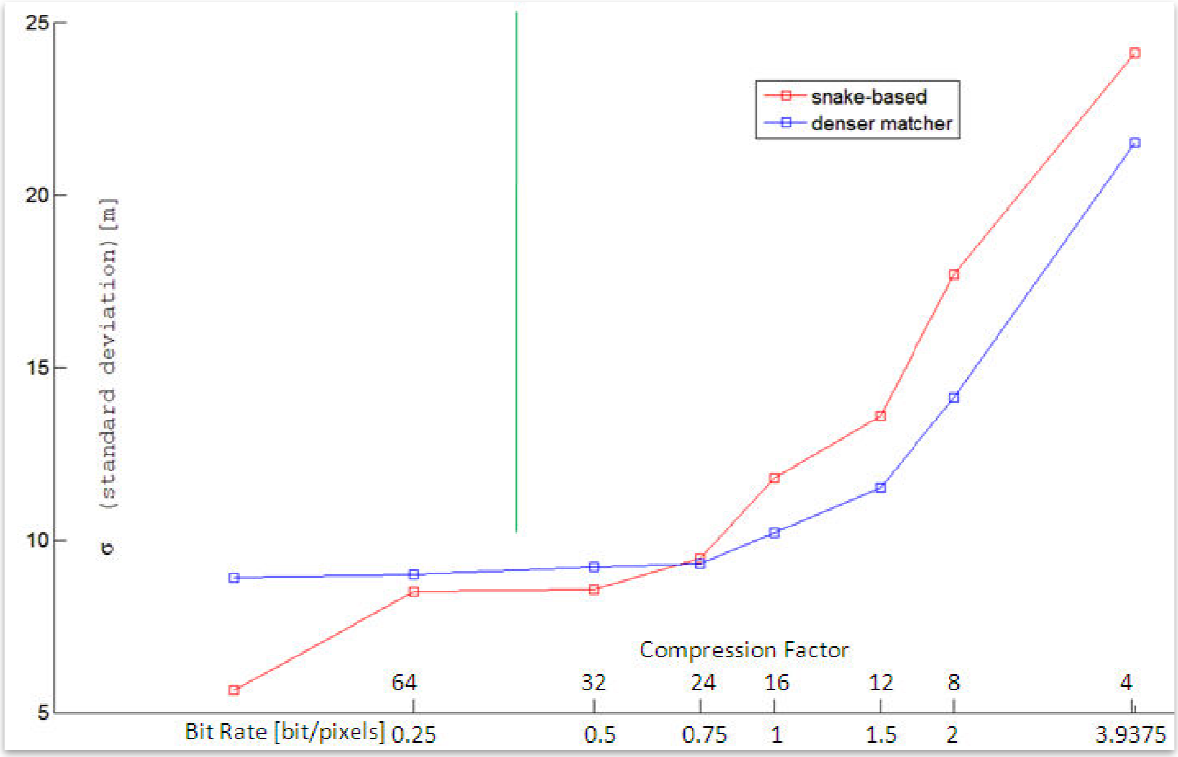

Figure 11 *Standard deviation of the error in reconstruction for the two algorithm in the case in which the couple of images is compressed with the same compression coefficient*

A strong difference between the two methods has to be considered:

- *the SIEM algorithm (with its greedy approach) gives a complete reconstruction of the surface, filling the holes generated where the information is not sufficient to use stereo by what we can define as an interpolation with neighbor parts.*
- *The Dense Matcher method does not give an effective complete reconstruction avoiding the parts which are not usable for stereo method.*

The completeness (percentile of the pixel reconstructed respect to the ones not used) of the Dense Matcher method is shown in Table 5. SIEM algorithm is structured to give a complete (100%) reconstruction of the surface.

%	4	8	12	16	24	32	63
4	85.12	61.62	55.85	51.36	50.87	50.47	50.51
8	59.10	87.82	78.95	75.66	74.98	74.88	74.61
12	51.70	78.59	88.19	85.87	85.00	85.33	85.03
16	47.12	75.26	87.2	92.25	92.57	92.75	92.75
24	46.11	73.66	85.2	92.47	95.74	96.29	96.42
32	45.6912	73.0596	85.0175	92.6175	96.1404	97.6912	98.0491
63	45.5789	72.5333	84.4561	92.4912	96.3088	98.0702	98.4632

Table 5 *Completeness (in percentage) using DenseMatcher algorithm and the same reconstruction applied to LOSSLESS images for the test image Crater C2*

References

[ABR00] Abrams, M. (2000). **The Advanced Spaceborne Thermal Emission and Reflection Radiometer (ASTER): Data products for the high spatial resolution imager on NASA's Terra platform**. *International Journal Of Remote Sensing, 21(5): 847-859.*

[CRE09] Cremonese G. et al., **The stereo camera on the BepiColombo ESA/JAXA mission: a novel approach**, *2009, Advances in Geosciences, 15, 305-322.*

[ECK05] Eckert, S., Kellenberg, T., Itten, K., 2005. **Accuracy assessment of automatically derived digital elevation model from ASTER data in mountainous terrain**. Int. J. Remote Sensing 26 (9), 1943–1957.

[YAM10] Yasushi YAMAGUCHI **ASTER Application in Urban Heat Balance Analysis (joint authorship), In: "Land Remote Sensing and Global Environmental Change"**, *Springer, 375-395, 2010.*

[MAS08] Massironi, M. et al. 2008, **Simulations using terrestrial geological analogues to assess interpretability of potential geological features of the Hermean surface restituted by the STereo imaging Camera of the SIMBIOSYS package(BepiColombo mission)**,*Planetary and Space Science, 56 (2008) 1079–1092.*

[SIM11] E.Simioni, G. Cremonese, G.Naletto, M.Massironi , G.Forlani., V.Da Deppo E.Segato**. A new stereo algorithm based on snakes;** *Accepted December 2010 PERS Photogrammetric Engineering and Remote Sensing, 2011*

[TOU02] Toutin, T., 2002**. Three-dimensional topographic mapping with ASTER stereo data in rugged topography**. *IEEE Trans. Geosci. Remote Sensing* 40, 2241–2247.

Chapter 7

Other applications of the image toolbox

Contents

Introduction

The image analysis toolbox created for the stereo analysis of the STC-Images was extremely helpful also in the analysis of other test images. In particular, it has been used in several different applications, always finalized to metrological applications, but not only in the space astronomy field.

This Chapter will describe the use of this toolbox in application different than the BepiColombo project. One case that has been analyzed is the use of the Shape From Silhouette (see Chapter 3) applied to asteroids images for the mission Rosetta; another application here described shows the application of the same method to the reconstruction of an archeological find from X-Ray data.

In both cases, the simplicity of the method has demonstrated its capacity and its versatility, bringing to new equipments for the analysis of shape images. This has been used not only for metrological analysis: in the case of the Rosetta asteroid images, it has allowed to calibrate the same images and to create a feedback system for the control (position and pointing) of the satellite.

7.1. Rosetta mission and Steins flyby

7.1.1. Rosetta mission

Rosetta is a Cornerstone mission of the European Space Agency(ESA). Its goal is to monitor a comet over several months on its way to perihelion with an orbiter and to investigate its surface and interior with a lander. Additionally, flybys of 2 asteroids are part of the mission plan.

The launch of Rosetta, first planned for January 2003, had to be postponed to the first quarter of 2004 due to problems with the launcher. As a consequence, all 3 mission targets had to be changed. Comet 67P/Churyumov-Gerasimenko was chosen as the new target comet. After the successful launch on 2 March 2004 the asteroids (2867) Steins and (21) Lutetia [LAM10] were selected as flyby targets, with closest approach in Sep. 2008 and July 2010, respectively.

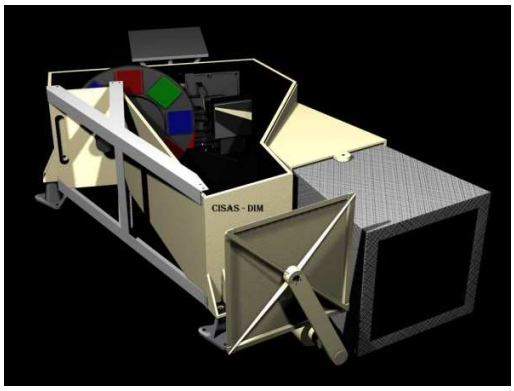

Figure 1 WAC Wide Angle Camera schematic overview.

Together with other 21 instruments, OSIRIS (Optical, Spectroscopic, and Infrared Remote Imaging System) is the system dedicated to image acquisition. It consists of a narrow angle camera (NAC) and a wide angle camera (WAC).

They are unobstructed mirror systems with focal lengths of 72 cm (NAC) and 14 cm (WAC). The focal ratio is f /D = 8 and f /D = 5.6 for the NAC and the WAC, respectively [DAD01]. Both cameras are equipped with 2048 × 2048 pixel CCD detectors with a pixel size of 13.5 µm. The image scale is 3.9 arcsec/pixel for the NAC and 20.5 arcsec/pixel for the WAC. OSIRIS is described in detail in [KEL10].

The flyby

On 5 September 2008 Rosetta passed the asteroid (2867) Steins with a relative velocity of 8.6 km s^{-1}. Closest approach (CA) took place at 18:38:20 UTC at a distance of 803 km, chosen such that the spacecraft could keep the instruments continuously pointed toward the asteroid. Early in the approach, the solar phase angle (Sun–object–observer) was 38°. It decreased to a minimum of 0.27° (opposition) 2

minutes before CA. It increased again to 51° at CA, and finally to 141° at the end of observations. The NAC (with five times higher resolving power) unfortunately stopped its automatic operation at a distance of 5200 km,10 min before CA. Thus the highest-resolution images of the surface of Steins were taken by the WAC.

Considering the minimal resolution of the Wide Angle Camera most of the measurement processes in the plane of the Steins flybys change their prospective. In fact, as we will see later, with such a limited resolution on an object with dimensions of about $6.67 \times 5.81 \times 4.47$ km^3,stereo dense reconstruction of the asteroid became a not-valid process; so a more approximate method as shape from silhouette was used for the asteroid shape definition.

As we could show, another problem made its appearance in this context related to the precision of the pointing of the satellite. Thanks to our work on the acquired images, we have been able to analyze in great detail this issue, and to find an optimal condition for the system geometry during the flyby.

The asteroid

The shape of Steins resembles that of a brilliant cut diamond. The last NAC image, taken at 31° phase angle before reaching minimum, and the best WAC image, near CA at 61.5° phase angle, show this very characteristic outline (Figure 2). The surface of Steins is mostly covered by shallow craters, often with subdued, ambiguous rims. Some of the larger craters are pitted with smaller ones.

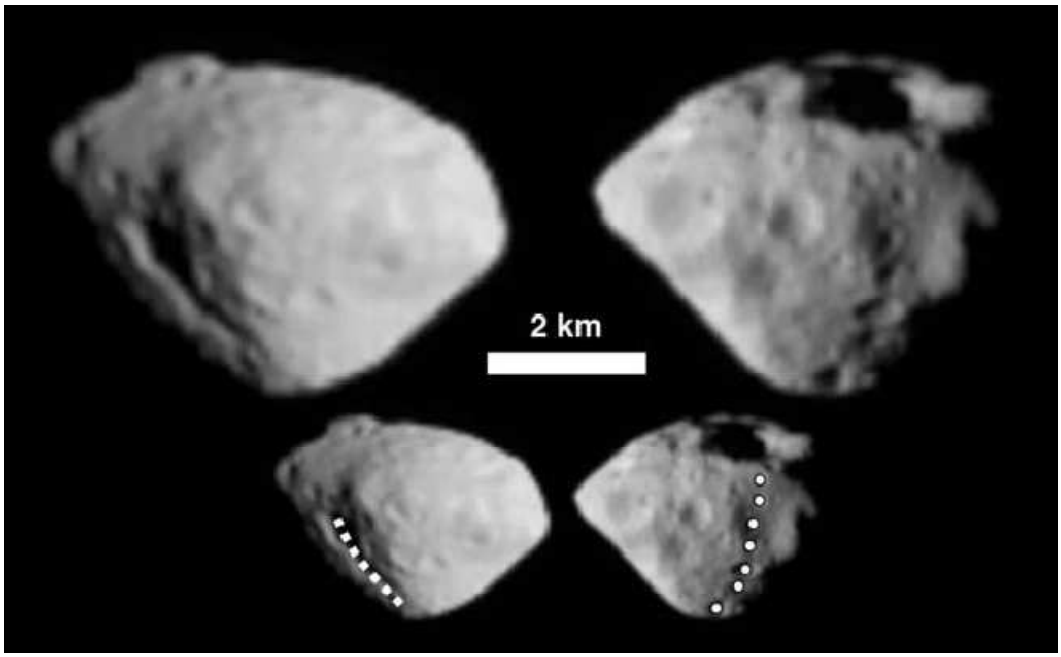

Figure 2 *The WAC image (top right) taken around CA at a phase angle of 61.5° shows the surface of Steins at a resolution of 80 m/pixel. The NAC image (top left) taken 10 min before CA has a slightly lower resolution of 100 m/pixel. The scale is given by the 2-km bar. The difference in viewing angle between the images is 91°, so they show opposite sides of the body. Celestial north is up. A large crater is visible near the South pole; Steins rotation is retrograde and therefore its North pole points toward the celestial South according to IAU rules. The positions of the catena with the seven pits (bottom right image) and of the large fault on the opposite side (bottom left image) are indicated on the small annotated image copies.*

The overall crater shape and depth-to-diameter ratio (~0.12) are consistent with degradation caused by ejecta blanketing and regolith disturbance by impact seismic shaking (2). A large, 2.1-km-diameter crater is located near the south pole.

A series of circular indentations and irregular ridges in an almost linear arrangement extending northward from this crater features prominently on the side that was visible during CA(see Figure 2). Chains of pits (or crater-like indentations) were also observed on other asteroids visited by spacecraft but not to the global extent seen on Steins.

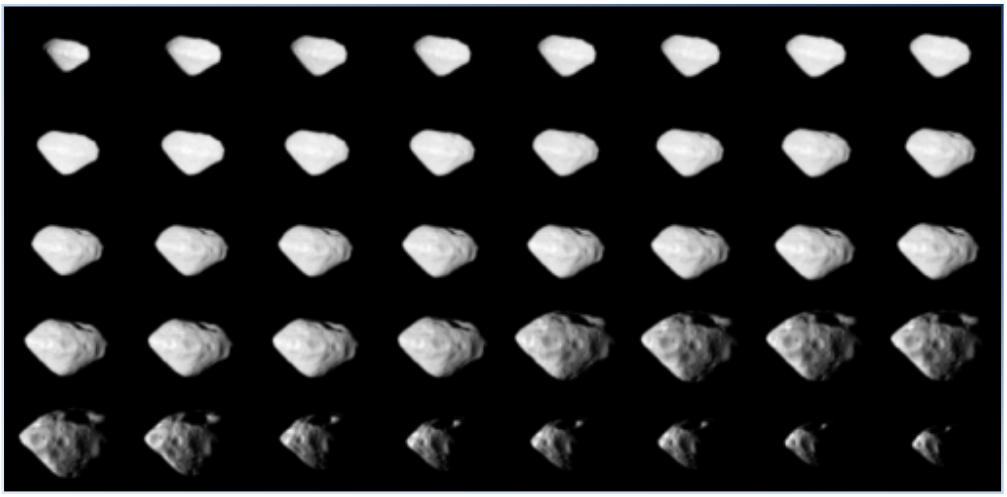

Figure 3 *Sequence of 40 selected images representing the flyby acquisition. Note that the approach to the satellite united to the low resolution of the WAC camera (not first-choice for this application) have brought to saturation problems in the first part of the acquisition and problems in the definition of the back-part of the asteroid due to the presence of a no so defined terminator.*

The chance of the formation of a chain (catena) of seven craters of roughly similar size is largely small. More reasonably, this feature could be linked to the impact at the origin of the large crater. It indicates partial drainage of loose surface material into a fracture within stronger, deeper material, possibly marking pre-existing physical inhomogeneity (5); therefore, we do not consider the seven pits of the catena to be impact craters. Another elongated feature(groove), surrounded by small pits and craters, is visible in NAC images (Figure 2): this groove is located along a meridian approximately opposite to the catena, also supporting the hypothesis of being another consequence of the large impact [JUT09].

7.1.2. The shape reconstruction

As previously explained, the rather poor image resolution of 80 m/pixel just allowed an approximate reconstruction of the shape of the asteroid by means of the shape from silhouette technique.

As explained in Chapter 3 this kind of method needs, to permit a correct reconstruction, to follow the following pipeline:

-Definition of the Prospective System for all the images (performed by kernel extraction)

-Definition of all the silhouettes of the target images

-Self reconstruction of the images.

Next section will explain the methods used to realize this process and the resulting linked-problems.

The precise definition of the Prospective System, that is of the position of the acquisition system in a defined reference frame, can be obtained by the so called kernels files. The SPICE kernels [NAI06] are files containing "low level" ancillary data that may be used to determine the higher level observation geometry parameters.

SPICE kernels files

Data provided by SPICE kernels refer to attitude and orbital position of probes and of natural space objects. These kernel files can be recalled to obtain a specific datum through various routines and subroutines. Matlab programming software is a suitable interface to access these kernel files by its interface with Mice, a toolbox which converts language in C++ and activate Spice, and returns the desired value through the called function.

These kernels contain, Rosetta, J2000 (the solar reference) and Steins position, Rosetta attitude for Steins flyby, and Rosetta frame, that tells to Spice how Rosetta and its instruments are related. After this initial data loading, various functions can be called in the Matlab script, for example to convert time from UTC to ephemerides; with this data it is possible to recall Rosetta attitude at each specific time. A note must be dedicated to Navigation and Ancillary Information Facility (NAIF1) code: it is a system to codify all space objects, and it is very useful to recall objects in Spice function. In fact, some subsystems are very similar in different mission, and internal data for these instruments have the same format. Even if this is not the case for WAC and NAC, this organization forces the system to be clear, and switching between various instrument or mission becomes fast and simple.

The only data that are not present in the kernel files are bitmaps from instrument and their time of acquisition. So we have to use other sources to complete our research. Without entering more in complicate details, an example of the reading procedure for an image is presented in following.

```
%  Load a set of kernels: an SPK file, a PCK file and a leap seconds file.
Use a meta kernel for convenience.

cspice_furnsh('E:\kernels\kernels\ck/ATNR_P040302093352_00077.BC  ');
cspice_furnsh('E:\kernels\kernels\fk/ROS_V14.TF                   ');
cspice_furnsh('E:\kernels\kernels\ik/ROS_OSIRIS_V10.TI            ');
cspice_furnsh('E:\kernels\kernels\lsk/NAIF0009.TLS                ');
cspice_furnsh('E:\kernels\kernels\pck/PCK00008.TPC                ');
cspice_furnsh('E:\kernels\kernels\pck/ROS_STEINS_V03.TPC          ');
cspice_furnsh('E:\kernels\kernels\sclk/ROS_080915_STEP.TSC        ');
cspice_furnsh('E:\kernels\kernels\spk/DE405S.BSP                  ');
cspice_furnsh('E:\kernels\kernels\spk/ORHR_____________00077.BSP');
cspice_furnsh('E:\kernels\kernels\spk/ORHO_____________00077.BSP');
cspice_furnsh('E:\kernels\kernels\spk/ROS_STRUCT_V1.BSP           ');
```

The first step is to define the SPICE kernel files inherent to the mission or satellite considered. The MATLAB command cspice_furnsh permits to save in memory the kernel files considered. Also, in this way, all orbit or target/satellite position updates, as implemented by the NAIF system, can be simply loaded by updating the singular files.

```
target   = 'STEINS';
frame    = 'J2000';
abcorr   = 'LT+S';
observer = 'ROSETTA';
instrument='ROS_OSIRIS_WAC';
[steins, found] = cspice_bodn2c(target);
[ROSETTA, found] = cspice_bodn2c(observer);
[WAC, found] = cspice_bodn2c(instrument);
```

The command cspice_bodn2c returns the SPICE identification code of the considered object. In this case the codes of Steins, ROSETTA and WAC are extracted.

After this process the words “STEINS”, ”ROSETTA” and “WAC” can be used to ask to kernels files their position and pointing at a definite time.

```
%    CSPICE_STR2ET converts a string representing an epoch to a
%    double precision value representing the number of TDB seconds
%    past the J2000 epoch corresponding to the input epoch.
epoch=['2008 SEP 05 18:34:0.132004'];
et = cspice_str2et( epoch );
```

```
%    CSPICE_SPKEZR returns the state (position and velocity) of
%    a target body relative to an observing body, optionally
%    corrected for light  time (planetary aberration) and stellar
%    aberration.
[state, ltime]=cspice_spkezr( target, et, frame, abcorr, observer);

%    CSPICE_PXFORM returns the matrix that transforms position
%    vectors from one specified frame to another at a specified epoch.
Ri = cspice_pxform(frame, instrument, et);
```

In this simple way at a defined time it is possible to obtain the "state" position c (in reference frame J2000) and the pointing R_i (rotational matrix) of the instrument. Other commands can integrate this information, as the knowledge of the Camera system $\mathrm{K_{WAC}}$ defined in the same kernels.

The result of a similar script is the knowledge at every time $et$of the projective matrix $\mathrm{P_{et}}$between a target considered (in this case STEINS asteroid) and a camera system (in this came Rosetta-WAC), and so the possibility to define the projective matrix needed for the 3Dreconstruction:

$$P_{et} = K_{WAC} R_{et} [\, I \quad | - \boldsymbol{c_{et}}]$$

This equation follows the format presented in Chapter 3, equation (4).

Silhouette extraction

The second step to determine the 3D shape of Steins by means of the Shape from Silhouette technique is the extraction of the silhouettes, or **Segmentation** of the target (Steins), from the images. The process is normally performed in automatic way, and it is rather easy for these images that have a so dark background (see Figure 2). As shown in Figure 4,the process can be performed by filter analysis and so called "erosion-dilatation" procedures [PAR90] explained in the Figure caption.

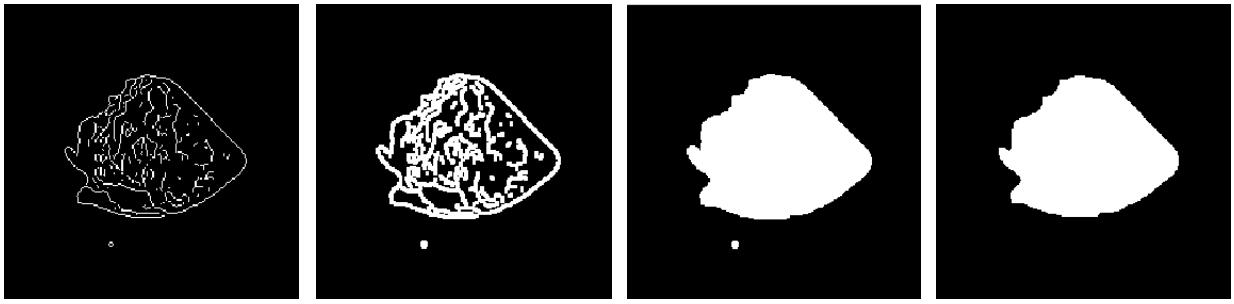

(a) (b) (c) (d)

Figure 4 *Given a Steins image, this figure shows: (a) the binary gradient mask, which defines the details of the images in Boolean format; (b) the dilated gradient mask performed by dilation of the previous images to close possible holes in the contour; (c) the result of a fitting-holes process on the previous image; (d) the final silhouette After the so called erosion-dilatation process external little shapes as the one presents in the other images in the button-left zone disappeared*

The result of this process for the image at closest approach is shown in Figure 5. The process is completely automatic and guarantees for all the images the definition of a silhouette that can be used for the shape from silhouette 3D reconstruction technique. The method presented (Sobel [SOB68] details filtering and erosion dilatation process [VIN09]) was chosen for its easy implementation. Best results could have been obtained with other algorithms, as snakes applied to segmentation; but the poor image resolution did not require a so precise method, so we moved to an easier algorithm.

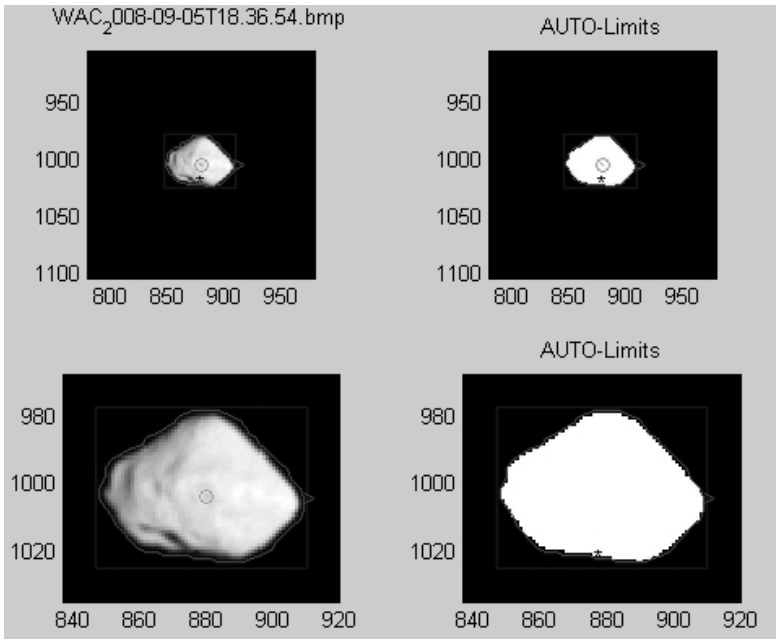

Figure 5 *Example of the application of the automatic silhouette extraction on the image at CA (Closest Approach). Original image (top) and its zoom (button) are shown on the left side of the figure; the obtained silhouette is shown on the right side.*

Problems occurred in the shadowed part of the image where the presence of the terminator makes not possible the automatic system. In that case, an approximation by hand of the possible shape (larger than the effective one) was made (see Figure 6)

At the end of this process, for all the images, a mask greater than the effective silhouette of the asteroid is obtained. This guarantees a volumetric reconstruction of the target.

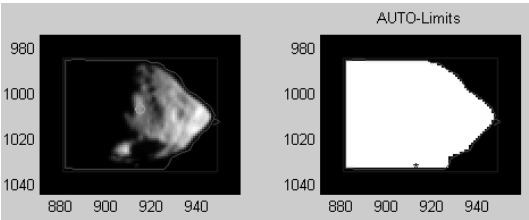

Figure 6 *Example of the approximation by hand of the silhouette to avoid terminator-problem.*

7.1.3. Results and considerations

After having applied the Shape from Silhouette process to all the available Steins images, the obtained result clearly demonstrated an incoherence of the input data. In particular the following issues appears:

- *the reconstructed model demonstrated to be smaller than the expected one and not so coherent with the one defined by light curves or photo-clinometry*
- *the projections of the silhouettes on the plane of the center of the asteroid were not aligned in critical manner, considering that all the images were taken from the same line (satellite orbit)*
- *the center of the model re-projected on the images sometimes was outside the same asteroid.*

These conditions, and particularly the third one, brought us to question the actual reliability of the projective system given by the kernel files. The same perplexity appeared using the DLR multi-stereo software.

The misalignment$D_{c/p}$between the center of the asteroid in the images and the re-projection of the center of the model on the same images presented a maximal value around 85 pixels in the WAC images and 23 in the few NAC images considered. A consistent error had to be investigated in the kernels data.

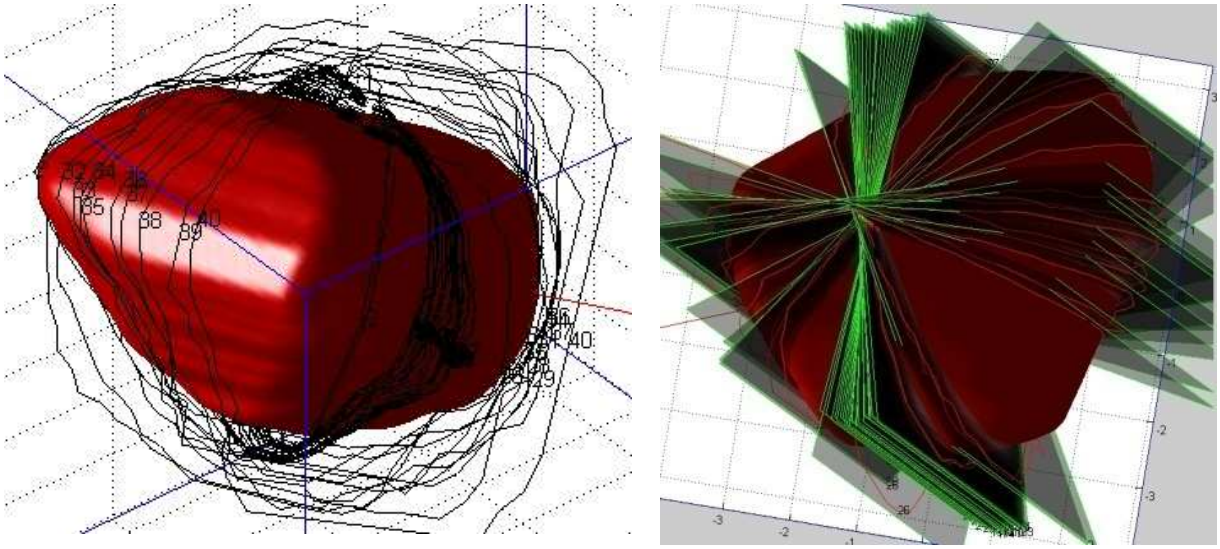

(a) (b)

Figure 7 *(a)First volumetric approximation by Shape From Silhouette Method of theSteins asteroid. Note the not co-alignment of the silhouettes (black lines). (b) Last reconstruction after the self alignment of the silhouette.*

In the attempt to correct the asteroid shape, a different approach was used using self-calibration of the camera system: in this way, a better result in reconstruction was obtained, and the new model presented a misalignment $D_{c/p}$ with a maximal value of 2 pixel.

Although this work has not produced an effectively usable (for measurement) 3D model, it brought to attention the problems on the kernel files.

On these basis, we are now investigating a relation between the errors in the kernel satellite position, and the filter wheel movements: a preliminary investigation seems to show that a possible solution to this problem can be found in a deeper analysis of the interaction between the OSIRIS filter wheels and the satellite reaction wheels.

7.2. X-Ray application

This section explains another different application of the image toolbox created as support of STC stereo channel. After the success of the use of the Shape From Silhouette method in Steins flyby, the same procedure was used in taxonomy field. Although this field seems so distant, the work here described can be simply seen as the application of an imaging measurement system to a different kind of acquisition system.

In this section, a brief explanation of the normal application of taxonomy will be given; then, the acquisition system and the problems which brought to a not-classical approach will be explained; finally, a description of the algorithm choices that have been applied to solve a completely not calibrated system will be provided.

This activity has been performed in the framework of the collaboration with the CNR IFN (Istituto di Fotonica e Nanotecnologia) laboratory LUXOR (Laboratory for Ultraviolet and X-ray Optical Research).

7.2.1.X-Ray Tomography

In the field of restoration of ancient handworks, X-ray tomography is a powerful method to reconstruct the internal structure of the object in non-invasive way. In some cases, such as small objects fully realized with hard metals and completely hidden by clay or products of oxidation, the tomography, although necessary to obtain the 3D appearance of the object, does not give any additional information on its internal monolithic structure. We present here the application of the shape-from-silhouette technique on X-ray images to reconstruct the 3D profile of handworks. The acquisition technique is similar to tomography, since several X-ray images are taken while the object is rotated.
The system can be seen as a flyby of the target (in this case the handwork) from different points of view on the same plane. Differently from an asteroid flyby in which the position of the camera system (although corrupted) is given (generally by other instruments) in this case a different method was used to calibrate the system, also in this case exploiting the image toolbox created for the STC image analysis.
Some reference points are placed on a simple structure co-rotating with the object and are acquired on the images for calibration and registration. The shape-from-silhouette algorithm gives finally the 3D appearance of the handwork.
We present here the analysis of a tin pendant of VI-VIII century B.C. (Venetian area) completely hidden by solid ground. The 3D reconstruction shows surprisingly that the pendant is a very elaborated piece, with two embraced figures that were completely invisible before restoration.

X-ray tomography refers to the cross-sectional imaging of an object from reflection data collected by illuminating it from several different directions. The impact of this technique in diagnostic medicine has been revolutionary, since it has enabled to view the internal structure of the human body with unprecedented resolution and precision in a non-invasive way. Fundamentally, tomographic imaging deals with reconstructing an image from several projections, where a projection at a given angle is the integral X-ray absorption of the image in the direction specified by that angle. Although from a mathematical point of view the problem of how to reconstruct a function from its projections has been solved by Radon at the beginning of the 20th century, the invention of the first X-ray computed tomographic scanner dates back approximately 40 years. Nowadays, tomography is an essential tool for inspecting the internal structure of an object [HEN99-KAL05]. Also in the field of restoration of ancient handworks, X-ray tomography is a powerful method to reconstruct the internal structure of the object in non-invasive way. In some cases, such as small objects fully realized with hard metals and completely

hidden by clay or products of oxidation, the tomography, although necessary to obtain the 3D appearance of the object, does not give any additional information on its internal monolithic structure.

The results of the application of the tomographic system was in this case a bench of images that could clearly be considered as silhouettes, and this was the cause which brings the application of the shape from silhouette methods to this project.

The acquisition technique is similar to tomography, since several X-ray images are taken while the object is rotated. Some reference points (nails) are placed on a light plastic structure co-rotating with the object and are acquired on the images for calibration and registration. The shape-from-silhouette algorithm gives finally the 3D appearance of the handwork.

There are two main differences with classical X-ray tomography: 1) the angular steps required to apply the shape-from-silhouette algorithm are typically 5° to 20° on the full 360° rotation, so very few images (of the order of few tens) are taken compared to what is required for a complete high-resolution tomography, which is typically acquired with 720 views in 0.5° angular steps; 2) low-energy X-ray are used, since it is not required that the radiation is transmitted through the object, but only the "X-ray shadow" has to be acquired. From the point of view of the users, the advantages given by the two previous characteristics are a very short acquisition time compared to tomography and the possibility of using low-power and low-energy X-ray sources. Two principal disadvantage, on the other side, have to be taken in account: obviously, the spatial resolution given by the shape-from-silhouette is low compared to what can be obtained with X-ray tomography and, as a limit of shape-from-silhouette method, not all the concavities of a target object can be solved.

We discuss here the technique and the algorithm. We present the validation tests made on a pewter object. Finally, we present the analysis of a tin pendant of VI-VIII century B.C. (Venetian area) completely hidden by solid ground. The 3D reconstruction shows surprisingly that the pendant is a very elaborated piece, with two embraced figures that were completely invisible before restoration.

Acquisition System

The X-ray system is shown in Figure 8.It consists of three different components: the X-ray source, the detector and the rotational stage, which is mounted half-way between the source and the detector. The sample to be analyzed is positioned on the stage.

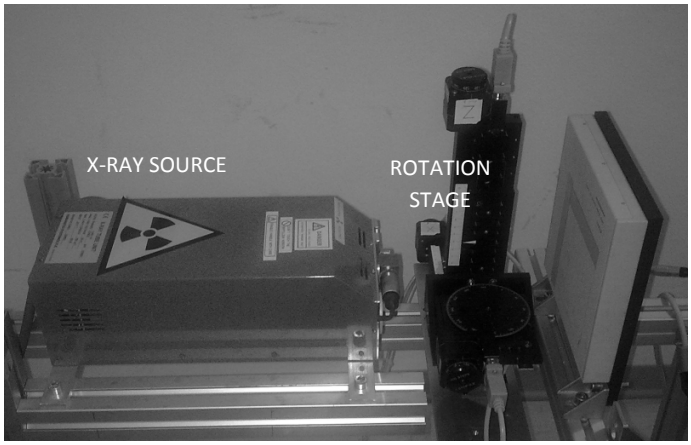

Figure 8 *The system for X-ray analysis. From left to right: source, translation stage and detector.*

The X-ray source is the Hamamatsu L8601-01. It is a microfocus X-ray tube with a tungsten anode whose focal spot ranges from 7 μm at maximum power (10 W) to 5 μm at reduced power (4W). The control system automatically decreases the tube current at the increase of the voltage in order to avoid damage to the system by exceeding the maximum power. The operating range is 20-90 kV and 0-250 μA.

The detector is a Hamamatsu C7943 flat panel sensor. It consists of a sensor board and a control board, both assembled in a 1 mm-thick aluminum package. The sensor board has a CsI scintillator plate and a two-dimensional photodiode array with a 1248 $\times$ 1248 pixel format with minimized blooming and high sensitivity to the green light emitted from the scintillator after the absorption of X-rays. Each row of pixels is addressed in sequence by the vertical shift register connected to the gate line. The sensor board also has 8 charge sensitive amplifier arrays, each having 156 channel amplifiers with a horizontal shift register. The detector delivers a frame rate of 7 frames per second (which can be increased by using a 2 $\times$ 2 or 4 $\times$ 4 binning) with a dynamic range of 12 bits. Its pixel size is 100 μm and the active area is 124.8 $\times$ 124.8 mm^2.

The motorized stage is made up of two linear stages and one rotary stage. The linear stages are mounted perpendicular to each other in order to permit translations along both the horizontal and the vertical axes. They have a travel range of 100 mm (vertical) and 200 mm (horizontal), a maximum velocity of 10 mm/s and a resolution of the order of 0.5 μm. The rotary stage has a 360° rotation range, a maximum rotation speed of 8 turns/min and a resolution of 0.01°. The system can be used both for classical X-ray radiography and phase-contrast imaging to objects as large as 100 $\times$ 100 mm^2. In particular, resolutions of 20 μm on biological specimens have been demonstrated through phase-contrast techniques [POL08].

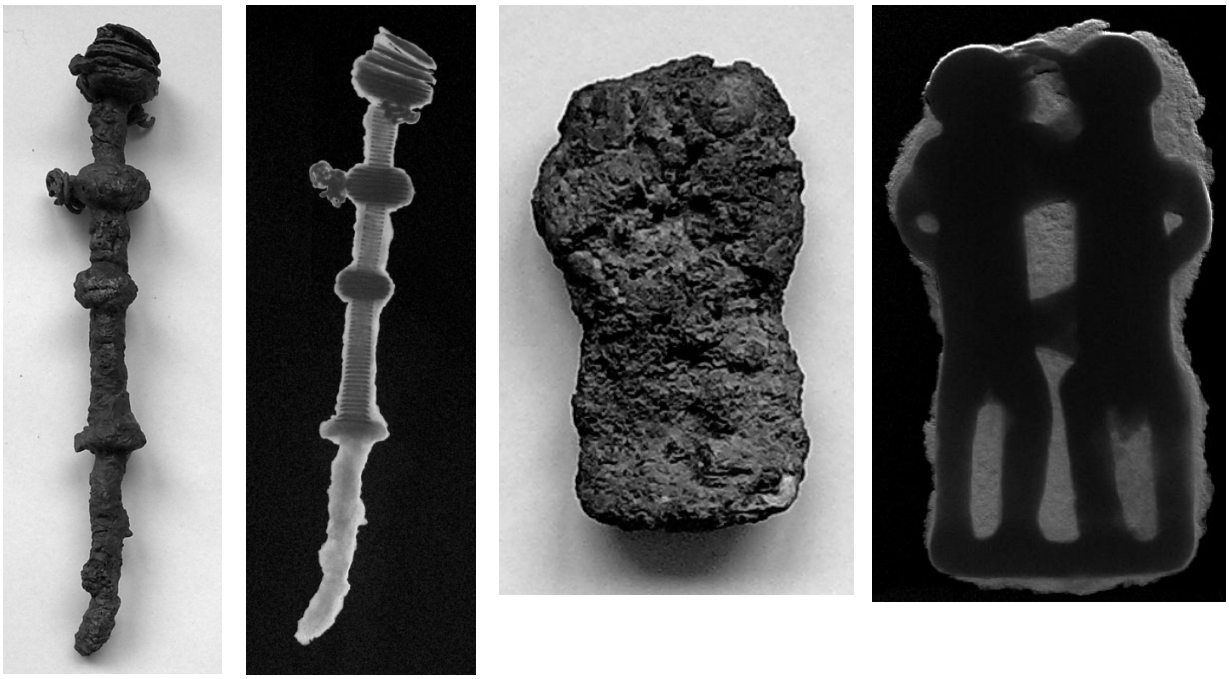

(a) (b) (c) (d)

Figure 9 *Different example of tomography images: Image of a brooch (a) and X-ray radiography revealing its fine internal structure with a spiral wire (b). Image of a pendant (c) and X-ray radiography revealing its internal appearance (d).*

X-ray radiography has been applied to the analysis of ancient handworks to assess the restoration process. Some of the images of ancient handworks from the Venetian area (VI century B.C.) are shown in Figure 9. The X-ray images have been acquired in the dual-energy mode to optimize the final contrast: two images have been acquired in 140 ms integration time with the source operated respectively at 90 kV-10W and 70 kV-10 W and then subtracted one to the other. In both cases, the radiography shows the fine structures of the objects that cannot be elsewhere inferred from the photos before restoration.

In particular, the X-ray images of the pendant shown in Figure 9 (c,d) are really impressive. It is clear that the object is monolithic therefore radiography gives no information on its internal structure. Nevertheless, X-ray images reveal some details on the architecture of the object that are completely invisible before restoration. It is clear that the pendant is a very elaborated piece, consisting of two embraced figures, a male and a female, that are completely invisible in the object as found. The 3D appearance of the pendant before restoration could be reconstructed by a complete tomography that would require 360-720 views on the 360° angle and a high-energy X-ray source. We present here the results of the shape-from-silhouette technique applied to the 3D reconstruction of monolithic objects as an alternative to tomography. Although some basic limitations of the algorithm have to be taken into

account in the revealing of the 3D shape, the main advantages of the technique here presented are the small number of views and the limited X-ray energy and power that are required. We present here a test case to assess the validity of the method as a measuring tool, then the results on the pendant that has been shown in Figure 9 (c,d).

7.2.2 New method for easy calibration

The tomography is a good test case for the shape-from-silhouette algorithm. The acquisition system is described as a set of several acquisitions of the same target seen from different point of views by the same pinhole camera. Here, we will describe in detail the calibration of the geometrical system, presenting a simple method to define the geometrical calibration of the reference frame.

To avoid the problem of the absence of an effective projection system, we inserted within the field-of-view of the X-ray camera of a set of tie-points that move with the reference frame. In our case a simple paper-box with 8 nails knocked in the vertex of the low and top faces of the structure was used to wrap the target, as shown in Figure 10. Obviously, any other material can be considered for fixing the nails, provided that the nails are visible in the X-ray images. The dimensions of the box surrounding the object have to be set in a way that all the tie-points are visible during the rotation, with the exception of the ones covered by the target in the X-ray projections.

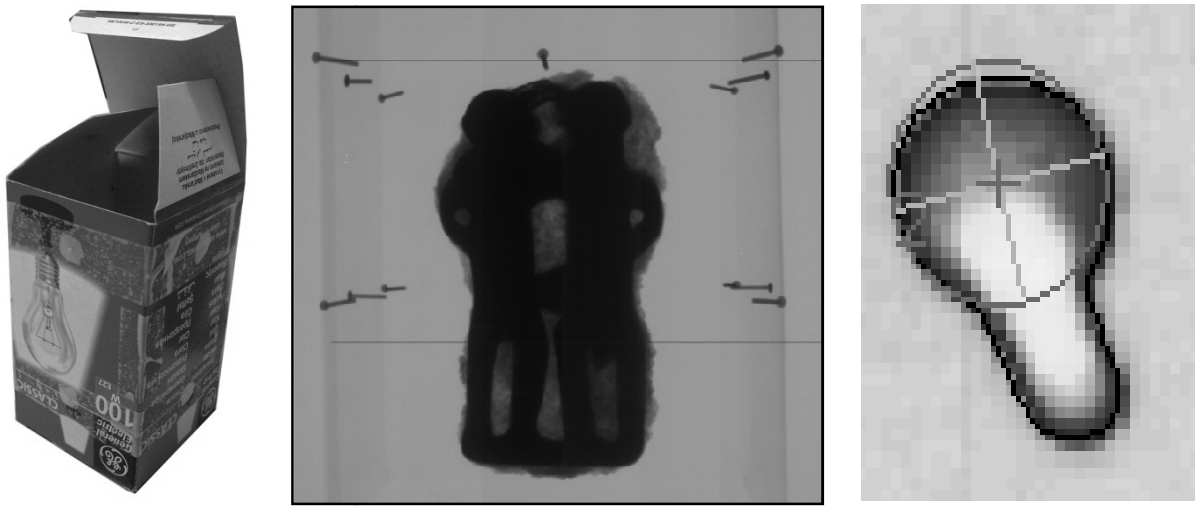

(a) (b) (c)

Figure 10 *(a) Box used to accommodate the nails. (b) Example of acquired image: observe the nails*

distributed around the object. (c) Detection of one of the nails.

Simple segmentation algorithm can be used to detect the silhouette of the targets and of the nails on the images. The nails-head have an almost elliptical shape, so it is rather simple to detect their centers. Furthermore, two additional considerations can be done:

- the up-nails and the down-nails (i.e. the nails belonging to the upper or lower face) can be divided by a simple control of the vertical coordinates
- the position of the same nail in two consecutive images can be detected by a Kalman filter[1] or parabolic approximation of the "orbits" of the nails on the coordinate position

This process applied to all the images gives the silhouette of the target and the position of all the tie-points, that are partially directly calculated on the images and partially evaluated by predictions where the target covers some of the tie-points. The geometrical system can be reconstructed through inversion of the projective matrices. The system is very redundant and this gives a minimum error in the geometrical reference frame. To demonstrate the precision of the system, a Gaussian error was applied to all the centers extracted for the nails to evaluate the variation of the volume of the object.

As previously described, the first step is the segmentation of the images. Any image is pre-processed by the use of classical expansion-erosion pipeline [GIA88] and a set of features is extracted. After the first segmentation all the closed extracted borders are measured and the outliers are deleted.

The acquisition system was chosen to avoid the overlap of the upper and lower part of the nails, therefore the tie points can be divided in different groups, B_{up} and B_{dw}, which represents the bases for calibration. B_{up} and B_{dw} are normally different from a topological point of view, since the former has a larger projective effect that is more useful for our aims. We can define the features considered as a side $B_{up/dw} = \{x_1, x_2,\ldots,x_n\}$ where x_i represents the two coordinates of the center of the feature considered.

[1]The Kalman filter is a set of mathematical equations that provides an efficient computational (recursive) means to estimate the state of a process, in a way that minimizes the mean of the squared error. The filter is very powerful in several aspects: it supports estimations of past, present, and even future states, and it can do so even when the precise nature of the modeled system is unknown.

Note that n is generally smaller than eight (i.e. the actual numbers of nails), since part of the nails are normally not detected and some x_i are the centers of not consistent features.

The next step is the selection of the sequence of consecutive images with the same n. Since the images are consecutive following the rotation of the target, we expect a relatively short distance between the same nail on two consecutive images of the sequence. Therefore the nails can be sorted, and in the same way all the features having no twin on the sequence are discarded.

Therefore, the images are divided in two parts: on one side the sequences with the same numbers of nails in which the same nails are ordered in the correct way and, on the other side, all the sequences of images in which the points are not identified. For any of the images in the first sequences, the positions of the nails is used to extrapolate the future position of the same nail of the next image on the hypothesis of a locally parabolic orbit. The nail is so chosen on the x_i of the following image. The process is repeated iteratively until the eight nails are identified in all the images, partially in coherence with the others images and partially not detected. For example, we can consider a base of the k image as $B_k = \{x_1, y_2, x_3, x_4, x_5, y_6, x_7, x_8\}$, where only the 2nd and the 6th nails were not detected and are indicated with y_i notation.

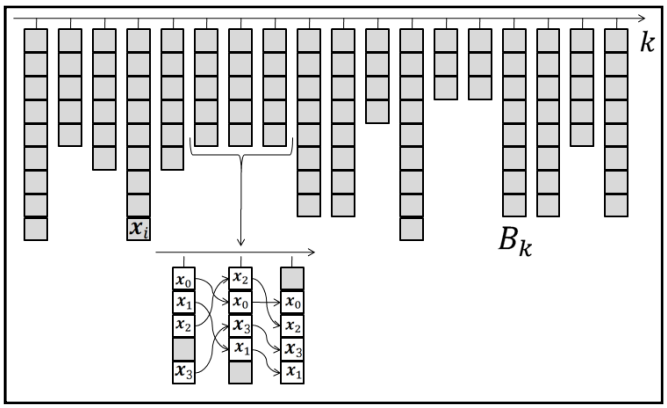

Figure 11 *Each image k is related to a base B_k of n points with n different for each image. The first step is to consider a sequence of images with the same n and to sort the considered points.*

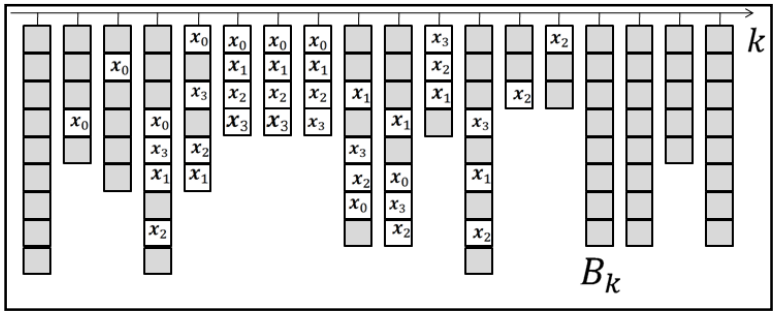

Figure 12 *The sequence considered in the previous image is used to detect the other points using parabolic approximation. The process is repeated until the maximum covering is granted.*

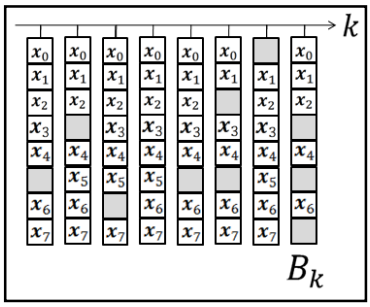

Figure 13 *Final configuration: all points are sorted and coherent. Some tie-points however are not detected.*

To complete the sorting process, the topology of the calibration system is used. The sequence can be calculated as

$$x_{ik} \sim P_k \begin{bmatrix} X_i \\ 1 \end{bmatrix} \quad (1)$$

where x_{ik} are the coordinates of the i_{th} nail on the k_{th} image, P_k is the projection matrix, and X_i represents the 3D coordinates of the i_{th} nail in a known reference system. Symbol "$\sim$" is used to identify the projection: the right part of equation (1) gives a 3D vector where the two first coordinates divided by the third are the effective 2D point x_{ik} .

It is simple to extract the matrix P_k (or its suitable approximation) knowing all the other elements of equation (1). We can define for any detected point the matrix L_i

$$L_i = \begin{bmatrix} [X_i^T\ 1] & 0_{1x4} & -x_{ik}[X_i^T\ 1] \\ 0_{1x4} & [X_i^T\ 1] & \end{bmatrix} \quad (2)$$

In this way we can define the global matrix L as the overlap of the L_i defined in (2).

$$\mathrm{L} = \begin{bmatrix} \mathrm{L}_1 \\ \\ \mathrm{L}_\mathrm{M} \end{bmatrix}$$

Where M is the number of the nails.

Defining as $\mathrm{l} \in \mathbb{R}^{12}$ the minor eigenvector of the matrix ($L^T L$) the projective matrix P_k can be written as the wrap form of l in a matrix 3×4. The vectors x_{ik} have to be normalized in mean and variance before calculating the corresponding L matrix. In this way it is possible to detect not only the projection matrix but even the y_i nails not seen by the process (i.e. see Figure 14).

Note that no additional information are required, as the modeling of the detector or the positioning of the rotating table.

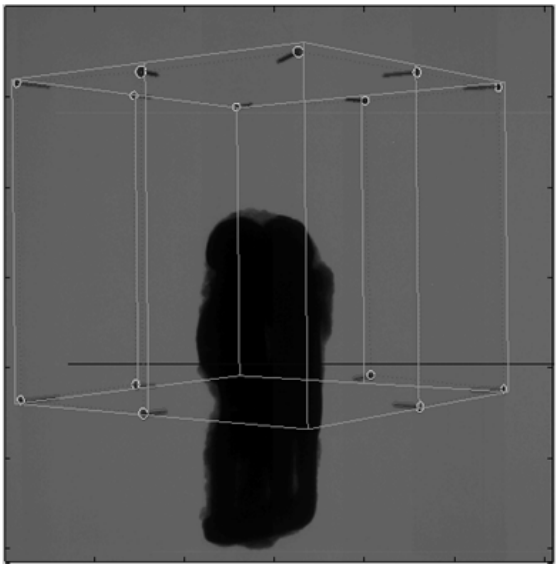

Figure 14 *Example of reconstruction of the calibration grid. Note that also the two vertices not detected are correctly positioned.*

Redundancy of the system permits a feedback control on the nails-sorting heuristic, to check a possible mis-interpretation of the algorithm.

7.2.3 Tests on a known object

Tests were performed to establish the robustness of the methods, by acquiring X-ray images of a known target. The target object is shown in Figure 15: it is the pewter model of a nun. The object was covered by a paste to simulate oxidation of a normal ancient target, therefore a normal photo cannot detect the 3D shape of the object.

(a) (b) (c)

Figure 15 *(a) Pewter object used as test target. (b) Object covered by a plastic paste. (c) X-ray image acquired of the object covered by the paste and inserted in the paper-box with the calibration nails.*

Eighty images were acquired all around the object with an angular step of 4.5°. The object was introduced in an external box with 20 nails distributed partially in the top part (8 nails), partially in the middle (4 nails) and partially on the base (8 nails) of a cube of 5.8 cm in side. The images were acquired with the source operated at 90 kV-10 W in 140 ms integration time. Some views of the reconstructed object are shown in Figure 16.

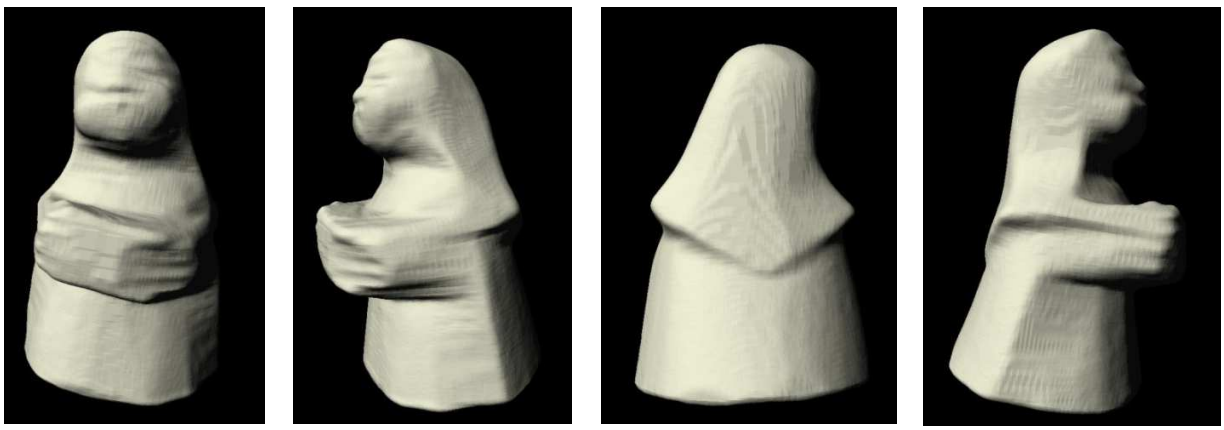

(a) (b) (c) (d)

Figure 16 *Different views of the reconstructed 3D model.*

After the completion of the calibration process, a Gaussian two-dimensional error was added to all the measurements of the positions of tails. Aim of the test is to measure the degradation of the final model due to the uncertainty in the measurements. Taking into account the maximum size of the nails, that is about 50 pixels, the error can be restricted to a standard deviation of 20 pixels. The schematic of the testing process is shown in Figure 17. As shown in Figure 18, the error in volume reconstruction is limited to 14% of the complete volume even where the error simulated in nail detection has a variance of 20 pixels. The effect of the noise on the reconstruction is shown in Figure 18 where the face of the reconstructed nun is shown both in case of not noise reconstruction and in case of an error with a 20 pixel variance. The monotony of the volume reconstructed with the increase of the noise variance is due to the lost of coherence of the silhouette.

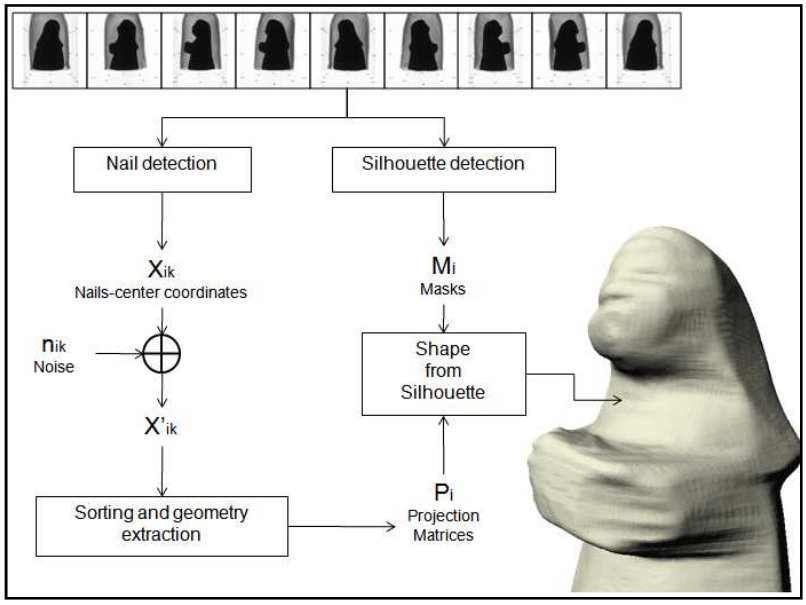

Figure 17 *Schematic of the testing process. The images are used to generate masks and tie-points coordinates. The coordinates were affected by Gaussian noise before being processed for geometry extraction. The resulting 3D model accuracy is then tested.*

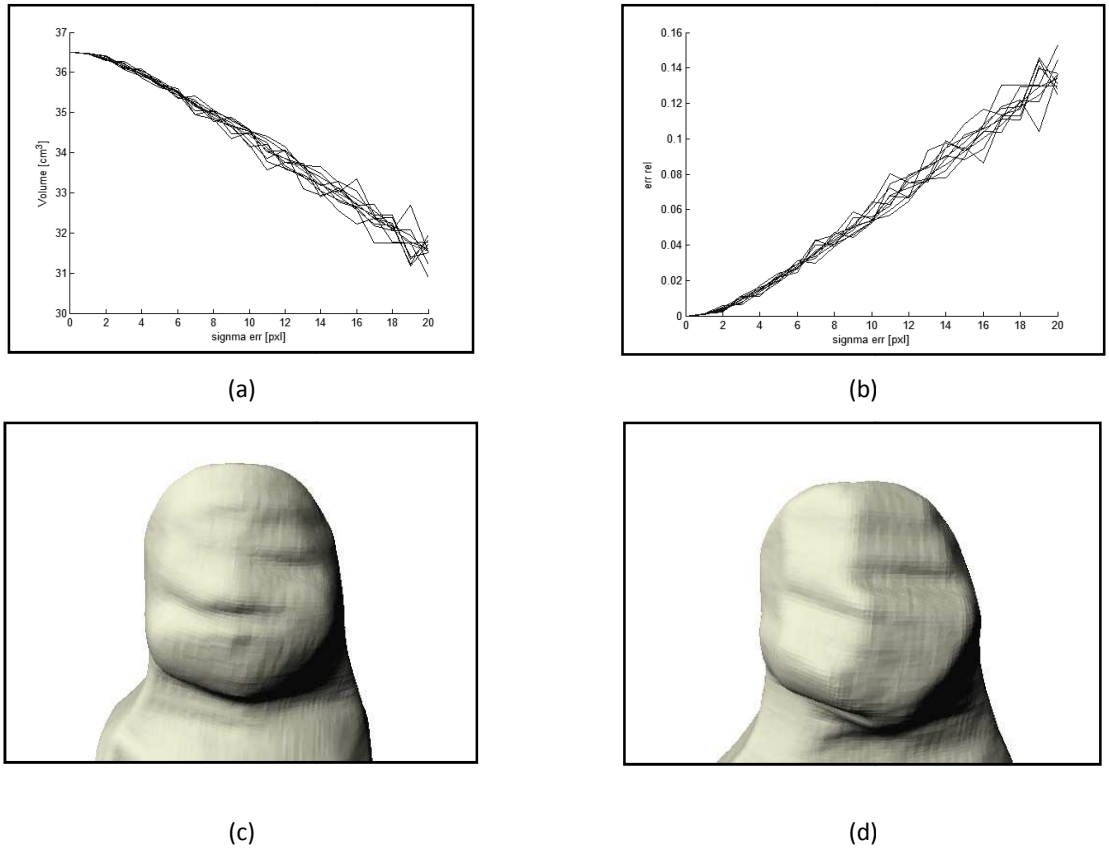

Figure 18 *(a) change of the object volume as a function of the noise introduced in the tie-detection; (b) Relative error on the effective volume as a function of the considered noise; (c) face of the nun reconstructed, where minimal features as mouth or eyes are visible; (d) Reconstruction generated using a noise with a variance of 20 pixels on the nail coordinates.*

Application to an ancient handwork

The acquisition procedure was applied to the pendant shown in Figure 9. Forty images were taken with an angular step of 9°. The object was introduced in an external box with 20 nails distributed partially in the top part (8 nails), partially in the middle (4 nails) and partially on the base (8 nails) of a cube of 5.8 cm in side. The images were acquired with the source operated at 90 kV-10 W in 140 ms integration time. The final 3D model is shown in Figure 19.

The application of the shape-from-silhouette technique on X-ray images to reconstruct the 3D profile of handworks has been discussed. The acquisition technique is similar to tomography, since several X-ray images are taken while the object is rotated. Some reference points (easily available for everyone) are placed on a structure co-rotating with the object and are acquired on the images for calibration and registration. The shape-from-silhouette algorithm gives finally the 3D appearance of the handwork. The technique can be very useful to reveal in a fast way the 3D appearance of objects that are not visible before restoration.

(a) (b)

Figure 19 *Reconstructed 3D model of the pendant.*

References

[DAD01] V.Da Deppo et al**.Optical performance of the Wide Angle Camera for the Rosetta mission: preliminary results**', *UV/EUV and Visible Space Instrumentation for Astronomy and Solar Physics'', SPIE Proc. 4498, 2001*.

[GIA88] C.R. Giardina and E.R. Dougherty**, Morphological Methods in Image and Signal Processing,** *Prentice Hall, 1988*

[HEN99] W. Hendee ed., **Wiley Biomedical Uses of Radiation, ,** *1999*

[JUT09] Jutzi et al. **A large crater as a probe of the internal structure of the E-type asteroid Steins** *Astronomy & Astrophysics manuscript no. JutzietalSteinsLetterAAFinalEdited c ESO 2009 December 11, 2009*

[KAK88] A.C. Kak and M. Slaney**, Principles of Computerized Tomographic Imaging**, *IEEE Press, 1988*

[KAL05] *W.A. Kalender,* **Computed Tomography**, *Publicis, 2005*

[KEL10] H. U. Keller et al.**"E-type asteroid (2867) Steins as Imaged by OSIRIS on board Rosetta"** *Science, Vol. 327. no. 5962, pp. 190 - 193, 8 January 2010. DOI: 10.1126/science.1179559*

[LAM10] Lamy et al**. Multi-color, rotationally resolved photometry of asteroid 21 Lutetia from OSIRIS/Rosetta observations** *A&A 521, A19 (2010) DOI: 10.1051/0004-6361/201014452 c_ ESO 2010*

[LAU04] A. Laurentini**, "The visual hull concept for silhouette-based image understanding***", IEEE Trans. Pattern Analysis and Machine Intelligence, 16, 150-162 (2004)*

[MAT00] W. Matusik, et al**, "Image-Based Visual Hulls", SIGGRAPH 2000, Computer Graphics Proceedings,** *Annual Conference Series, 369-374 (2000)*

[NAI06] **NAIF SPACE KERNELS Mars Global Surveyor MOC Instrument:** h*ttp://isis.astrogeology.usgs.gov/Isis2/isis-bin//naif_spice.cgi?isis_moc_kernels.html*

[PAR90] J. Parker. **A system for fast erosion and dilation of bi-level images**. *Science computer*, 5(3):187 –198, 1990

[SOB68] Sobel, I., & Feldman, G. (1968). **A 3 × 3 isotropic gradient operator for image processing**. *Presented at atalk at the Stanford Art ificial Project.*

[VIN09] O. R. Vincent, and O. Folorunso **A Descriptive Algorithm for Sobel Image Edge Detection** *Proceedings of Informing Science & IT Education Conference (InSITE) 2009*

[POL08] L. Poletto, M. Caldon, G. Tondello, A. Megighian**, "A system for high-resolution X-ray phase-contrast imaging and tomography of biological specimens***", SPIE Proc. 7078, ologiaphy has been applied 70781P (2008)*

[YEM04] Y. Yemez et al**, "3D reconstruction of real objects with high resolution shape and texture",** *Image and Vision Computing 22, 1137–1153 (2004)*

Chapter 8

Conclusions

This work has been essentially devoted to development of a new method for the 3D reconstruction of the Mercury surface.

In the framework of the development of the stereo camera for the BepiColombo space mission, the new algorithm for stereo image matching SIEM (*Stereo Image Evolving Model*) has been presented. Its basic idea is to implement a semi-dense stereo method where an approximate disparity field is modeled as a *deformable surface* that evolves improving image correspondences.

A key feature of the new algorithm is that it can be extended in a straightforward manner to incorporate additional information available to improve the solution. In fact, the snake approach enables to integrate every additional constraint on the object surface or on the stereo-images provided it can be expressed by a dual force. The new algorithm has also three interesting characteristics that may turn as advantages with respect to area-based methods. Its performance seems to compare very well with that of state of art area-based algorithms in terms of image measurement accuracy. The possibility to use matching windows as small as 3x3 pixels to compute the similarity function allows for more details of the object shape to be captured and represented in the DTM. Finally, the reconstruction of the disparity map takes place at once and not on a point-by-point basis; this ensures a consistency of the solution that prevents large mismatches and keeps a bound on the largest errors. This might prove an important asset in the context of space missions, where data redundancy is often limited due to data volume constraints and therefore multi-image coverage cannot be exploited to increase matching reliability.

The method has, however, also some limitations. The most important is, on the theoretical side, the hypothesis that there are not occlusions; this may prevent success in very steep areas: for instance, in the BepiColombo case, the theoretical limit is set by a slope inclined of about 74°. Also strong perspective deformation may cause convergence problems, because NCC would not provide in that case an accurate measurement of similarity. This might be solved either by using pre-rectification of images (so the new method would be used as refinement of conventional area-based or in an image pyramid) or, more fundamentally, by allowing image resampling (deformation of the grey values) within the similarity function. More investigation is required to better clarify this point.

As far as processing time and memory requirements are concerned, the method is, as any global method, more demanding compared to area based methods. By means of a suitable optimization of the code and

thanks to the continuous increase of the computation speed of modern computers, it is expected that in a short time this problem can be greatly reduced.

Several tests to investigate the advantages of the method will be performed. The main objective of future investigations will be the analysis of the dependence of the ratio parameter on the surface roughness and on images texture. The integration of shape-from-shading in the snakes forces, currently underway, is expected to provide a faster and more reliable convergence of the deformable model to an optimal solution.

The characteristics of the set of images used for the tests, however significant, is certainly still limited and have to be extended to cover a wider range of geological feature of planets with different morphologies and textures.

The critical ambient and the particularity of the camera system, first in the history to be considered as an effective Stereo-Camera with a push frame acquisition system, has brought to the definition of the new algorithm more adaptable and extendible of the actual state of art.

The software performance exposed in the last chapters demonstrate the reliability of the process to synthetic and satellite images revealing the capability to obtain performance very close and sometimes better than a classical pipeline, with the advantage of the extendibility to other kind of information to reach a complete use of all the procedure (as photoclinometry) and hypothesis (surfaces BRDF) so to get a much more precise surface reconstruction.

Other applications of the work were presented in the last chapter demonstrating that the toolbox generated to implement the new method SIEM had given results in different fields, so showing its versatility.

Pubblications

G.Cremonese, D.Fantinel, E.Giro, M.T.Capria, V.Da Deppo, G.Naletto, G.Forlani, M.Massironi, L.Giacomini, M.Sgavetti, E.Simioni, C.Bettanini, S.Debei,. M.Zaccariotto, P.Borin, L.Marinangeli, E.Flamini,	**The stereo camera on the BepiColombo ESA/JAXA mission: a novel approach, *2009*,** *Advances in Geosciences, 15, 305.*
S. Marchi, C.Barbieri, S.Casotto, G. Cremonese, Da Peppo V., Ferri F., Lazzarin M., Magrin S., Martellato E., Marzari F., Mottola S. and Simioni, E.	**Analysis of Steins Cratering History Using the OSIRIS/ROSETTA Images.** *In: Bulletin of the American Astronomical Society, 41, 558. American Astronomical Society. 41th DPS Meeting, 4.-9. Okt. 2009, Puerto Rico.*
G.Cremonese, M.T.Capria, V.Da Deppo, G.Forlani, M.Massironi, G.Naletto, M.Sgavetti, L.Giacomini, E.Simioni, E.Flamini, S.Debei, and the SIMBIOSYS International Team,	**New approach for the stereo camera on the ESA mission BepiColombo,** *Geophysical Research Abstracts, Vol. 9, 06137, 2007*
G.Cremonese, M.T.Capria, V. Da Deppo, D.Fantinel, G.Forlani, M.Massironi, G.Naletto, M.Sgavetti, L.Giacomini, E.Simioni, E.Flamini, S.Debei and the SIMBIOSYS international team,	**New approach for the stereo camera on the ESA mission BepiColombo,** *2007, AOGS, Bangkok***.**
G.Cremonese, M.T.Capria, V. Da Deppo, D.Fantinel, G.Forlani, M.Massironi, G.Naletto, M.Sgavetti, P.Borin, E.Martellato, L.Giacomini, E.Simioni, E.Flamini, S.Debei and the SIMBIOSYS international team.	**The stereo camera on the ESA mission BepiColombo; a novel approach,** *2008, COSPAR, Montreal (Canada).*
E.Simioni, G. Cremonese, G.Naletto, M.Massironi , G.Forlani. E.Segato.	**A new stereo algorithm based on snakes;** *Accepted December 2010 PERS Photogrammetric Engineering and Remote Sensing*
Cremonese, Gabriele; Simioni, E.; Naletto, G.; Forlani, G.; Da Deppo, V.; Massironi, M.	**A New Stereo Reconstruction Software for STC/SIMBIOSYS on BepiColombo,** *American Astronomical Society, DPS meeting #41, #67.07*
E. Simioni, F. Ratti, I. Calliari, L. Poletto	**Three-dimensional reconstruction with X-ray shape-from-silhouette** *(SPIE X-RAY) Proc. SPIE, Vol. 7804, 78040X (2010)*

Acknowledgments

I wish to acknowledge the Italian Space Agency which has supported the Simbiosys suite for the BepiColombo mission and indirectly also my PhD grant, giving me the possibility to reach the results here described. All this work would not have been done without the support of the National Institute for Astrophysics. Particular acknowledgments have to be done to my PhD supervisor, Prof. G. Naletto, and my Co-Supervisor, Dr. G. Cremonese, which have followed me during these years; they also introduced me to other space projects, as Rosetta and Messenger, and to extremely fruitful collaborations with foreign institutions, as DLR in Berlin and JAXA in Japan.

In the acknowledgements, also the STC team has to be mentioned since it collaborated to this work giving important ideas and resources. People as M. Massironi, V. Da Deppo, G. Forlani have represented a compact and solid working group.

Great contribution and new work perspective was given to this thesis by many people working at DLR institute during the period I spent in Berlin under the supervision of Prof. J. Oberst.

The years I spent at CISAS during this thesis work have been really exiting and productive: I am proud of the obtained research results and to have had the possibility to give my contribution to such an important work.

To mum and dad.

To my family.

To all the always friends, always around and always here:

To the loop artist Gianluch,to Marco.

To the nomadic friends and Coco.

To the colleagues of the Luxor laboratory.

To Antonello and Fausto.

To Davide and Ada to much young to read these acknowledgments but always ready to make me smiling.

To Pico and Ironically to my Nemesis :)